ABSTRACT

Title of Dissertation: Aspects of Unconventional Transport and Quasiparticles in Condensed Matter Systems
Huan-Kuang Wu
Doctor of Philosophy, 2023

Dissertation Directed by: Professor Jay D. Sau
Department of Physics

Transport in condensed matter system serve as one of the main properties for characterizing its phases and topological properties. A cornerstone in the theoretical efforts in transport is the Boltzmann transport equation (BTE), which describes the low frequency responses of weakly correlated systems through distribution functions of particle-like carriers. The BTE is extremely successful in describing transports in classical systems where the collision is largely uncorrelated and the quasiparticles wave lengths are significantly less than the mean free path. However, such major assumptions made by the Boltzmann transport does not hold in many aspects of modern condensed matter systems. Examples of such scenarios include quantum ballistic transport on the edge of a quantum Hall system, variable-range hopping in an Anderson localized system, and transport above the Mott-Ioeffe-Regel limit in bad metals. In this thesis, we discuss three example systems that exhibit transport properties beyond the conventional Boltzmann framework.

First, we will introduce a new family of systems for Majorana zero mode that does not require an external magnetic field. Our proposal is based on a planar Josephson junction setup

with a quasi two dimensional spin-orbit coupled electron gas and the usual role of the magnetic field that breaks the time reversal symmetry is taken by three phase biased superconductors. This idea is then simulated with HgTe as the two dimensional material together with realistic parameters. Our result demonstrates a large parameter regime of Majorana zero mode and a topological gap at the order of the superconducting gap.

In the second part, we will discuss the physics of plasmonic mode in a Josephson junction chain in its insulating regime. Utilizing the Luther-Emery point of the sine-Gordon model, the polarizability can then be interpreted by the responses of soliton and anti-soliton pairs. we consider the system in both the clean limit and with disorder. Our theory suggests the existence of coherent phase mode in the insulating regime and provides a natural explanation for the frequency-dependent broadening of such a mode. The results is consistent with the recent experiments on the reflection spectrum of Josephson junction chains.

Finally, we will look into the problem of Planckian thermal diffusion bound where a mechanism for sub-Planckian thermal diffusion is introduced. We will study a lattice system with large degrees of freedom per unit cell but has limited channel for heat conduction. In the highly-nonlinear regime, the thermal diffusivity can be solved accurately through applications of fluctuation-dissipation theorem. Through numerical simulations, our proposal demonstrate a modification of the lower bound to D_P/N, where D_P is the Planckian diffusivity and N is the per-unit-cell degrees of freedom.

Aspects of Unconventional Transport and Quasiparticles in Condensed Matter Systems

by

Huan-Kuang Wu

Dissertation submitted to the Faculty of the Graduate School of the
University of Maryland, College Park in partial fulfillment
of the requirements for the degree of
Doctor of Philosophy
2023

Advisory Committee:
Professor Jay D. Sau, Chair/Advisor
Professor Steven M. Anlage
Professor Johnpierre Paglione
Professor Victor Yakovenko
Professor Christopher Jarzynski, Deans Representative

Acknowledgments

My time as a PhD student has been a significant journey for me, largely due to the intriguing physics problems I got to explore. This experience was made possible by the guidance of my advisor, Jay Sau. He always encouraged me to ask questions which often leads to discussions that were both engaging and insightful. Reflecting on my years at the University of Maryland, the most valuable aspect was undoubtedly working with someone as intelligent and capable as Jay. Besides his mentorship in research, Jay is genuinely supportive of our career paths. I am extremely grateful for his advice and support throughout my time here in the University of Maryland, especially when I began considering career options in the industry.

I would also like to express my gratitude towards Dr. Anlage, Dr. Jarzynski, Dr. Paglione, and Dr. Yakovenko. for making the time to serve as my dissertation committee members. Their valuable advice on my thesis content and the interesting discussions during the defense not only enriched my thesis but also marked a memorable conclusion to my journey in physics.

Finally, I would like to thank my wife Wen-Chen and my 21-month old daughter Nora. Wen-Chen has been my rock, providing immense mental support during the most challenging times. Her willingness to take on the primary responsibility of caring for Nora, especially during the long hours I dedicated to my work in the past two years, has been invaluable. Nora, while requiring much time and resources, has brought an entirely new purpose to my life. Her presence is a constant source of motivation and joy, fueling my drive even through the challenging, sleepless nights she sometimes brings.

Table of Contents

List of Figures

List of Abbreviations

2DEG	Two-dimensional electron gas
ABS	Andreev bound state
AZ	Altland and Zirnbauer
BdG	Bogoliubov-de Gennes
BTE	Boltzmann transport equation
CDW	Charge density wave
JJ	Josephson junction
MBS	Majorana bound state
MZM	Majorana zero mode
QPS	Quantum phase slip
SAP	Soliton-antisoliton pair
TI	Topological insulator

Chapter 1: Introduction

Condensed matter physics are concerned with systems composed of interacting macroscopic degrees of freedom. In its stationary state, the system reach its thermal equilibrium that is governed by the conservation of energy. The likelihood of the macroscopic system to be at energy E is determined by maximizing the number of ways the total energy is distributed among the system and its environment. Accordingly, the canonical ensemble suggests that the probability of the macroscopic system to have energy E is given by $P(E) \propto \exp\{(-E/k_BT)\}$. For a separable system, whose dynamics of its constituent degrees of freedom can be addressed individually, the same form of distribution is generalized to the microscopic scale, a result that is commonly referred to as the Maxwell-Boltzmann distribution $P(i) \propto \exp\{(-\epsilon_i/k_BT)\}$ where i labels the microscopic state which has energy ϵ_i. The microscopic degrees of freedom carries physical quantities such as energy and charge, which collectively comprise the corresponding density field in the real space coordinates. In the presence of an external stimulus such as a temperature gradient or electric field, the system will be taken away from its thermal equilibrium state. The relaxation process of the density fields from the out-of-equilibrium distribution results in generation of the corresponding current. Such processes describe most transports in general in condensed matter physics.

The development of transport theory has seen a cornerstone in the Boltzmann transport

equation (BTE), which describes the dynamics of the distribution function of macroscopic degrees of freedom in phase space. It breaks down the contribution to the general evolution into three separated terms which corresponds to diffusion, external drive and the scattering process. In particular, the scattering rate can be formulated using the cross section obtained by quantum mechanics, allowing a semi-classical calculation of transport coefficients of a wide range of systems.

Despite the BTE being a universal transport formalism applicable to any system with fluctuations that can be broken down into localized excitations, one major assumption is that the collision process is uncorrelated so that the evolution equation only involves single particle distributions, which is also known as "Stosszahlansatz" by Boltzmann. As a result, alternative transport models are often useful in special scenarios. For example, in certain nano-scale systems, the mean-free path of carriers, which measures the length scale at which a collision happens, can exceed the scale of the system size. In this case, the transport process becomes ballistic and is captured accurately by the Landauer-Buttiker formalism in which the current is simply determined by the driving field at the two ends of the material and the number of the transport channels. In this case, the energy relaxation occurs in the leads instead of collisions in the system.

The central assumption made by the Boltzmann equation is that the carrier of the physical quantities in the system has a particle-like characteristic such that the macroscopic dynamics can be described classically through a phase space distribution function. Such an assumption can become invalid in systems whose quantum coherence is preserved in the transport process and systems whose nonlinearity dominates such that the quasiparticle picture breaks down. In such cases, other transport theorie are often used for evaluating the transport coefficients. For example, in the ballistic transport regime, the Landaur-Büttiker formalism captures the quantum transport

more accurately and in regimes characterized by incoherent transport, more general theories such as the Green-Kubo relation, are more applicable.

1.1 Boltzmann Transport Equation

The Boltzmann transport equation (BTE), first introduced by Ludwig Boltzmann in 1872 [2], provides a fundamental framework for analyzing transport phenomena across a wide range of systems. This equation describes the evolution of the distribution function for particles or quasi-particles under the effect of external fields and the scattering process. As mentioned above, the underlying assumption in the Boltzmann transport is that wave packets retain coherence and are sufficiently localized to allow for a meaningful definition of spatial distribution. This enables the characterization of transport phenomena by tracking the evolution of these wave packets within phase space.

Assuming a distribution function $f_k(r)$ that represents the number of carriers in state k is located at spatial location r. The evolution of f_k can then be written as the combination of contribution from diffusion, external field, and collision. That is,

$$\frac{df_k}{dt} = \left[\frac{\partial f_k}{\partial t}\right]_{\text{diff}} + \left[\frac{\partial f_k}{\partial t}\right]_{\text{field}} + \left[\frac{\partial f_k}{\partial t}\right]_{\text{coll}}. \tag{1.1}$$

First, the diffusion term is the direct result of particle's motion on a spatially non-uniform distribution,

$$\left[\frac{\partial f_k}{\partial t}\right]_{\text{diff}} = -\vec{v}_k \cdot \vec{\nabla} f_k. \tag{1.2}$$

For a given k, this can be understood as the drift in the spatial distribution function. Next, the

contribution from the external field is

$$\left[\frac{\partial f_k}{\partial t}\right]_{\text{field}} = -\vec{F}_k \cdot \vec{\nabla}_k f_k. \tag{1.3}$$

where $\vec{F}_k$ denotes the force acting on k from external field that satisfies $\vec{F}_k = d\vec{k}/dt$. In the case of electron, and k being its wave vector, $\vec{F}_k = -\frac{e}{\hbar}(\vec{E} + \vec{v}_k \times \vec{B})$. Finally, the collision term, or the collision integral, contains all contributions from different scattering processes that changes the carrier occupation in state k. In the case of metals, such processes include the interactions such as the electron-electron and electron-phonon scattering and scattering with lattice disorders. Under the steady state condition, $df_k/dt = 0$, Eq. 1.1 becomes

$$\vec{v}_k \cdot \vec{\nabla} f_k + \vec{F}_k \cdot \vec{\nabla}_k f_k = \left[\frac{\partial f_k}{\partial t}\right]_{\text{coll}}, \tag{1.4}$$

which is the well-known Boltzmann transport equation (BTE). While the BTE offers a general and conceptually straightforward framework, applying it in practice is challenging due to the complexity of obtaining solutions. The collision integral in Eq. 1.4 is governed by the microscopic scattering process in the system. Accordingly, BTE for a general condensed matter system is an integro-differential equation that is highly non-trivial to solve which usually involve sophisticated numerical methods.

1.1.1 Relaxation Time Approximation

To make the Boltzmann transport analytically tractable, simplification to the collision integral is often needed. In this section we will introduce the relaxation time approximation.

At thermal equilibrium, the principle of detailed balance states that for every possible microscopic configuration of a system that can change into another configuration with a certain probability, there is a reverse process with the same probability in equilibrium. Accordingly, the collision integral should vanish at the equilibrium distribution f^0,

$$\left[\frac{\partial f_k^0}{\partial t}\right]_{\text{coll}} = 0. \tag{1.5}$$

The relaxation time approximation consider the cumulative effect of the microscopic scattering act to dissipate deviations from the equilibrium distribution of state k, characterized by a relaxation time scale τ_k. That is,

$$\left[\frac{\partial f_k}{\partial t}\right]_{\text{coll}} = -\frac{f_k - f_k^0}{\tau(k)}. \tag{1.6}$$

The relaxation time approximation can be understood as two main assumptions. First, the distribution of the particle state after collision does not depend on the current non-equilibrium distribution. Second, if the particle distribution about position r is in a local equilibrium state described by temperature $T(r)$, then the collision process does not change this distribution. Additionally, as shown in Ref. [3], relaxation time approximation becomes exact under the assumption that the system is spherically symmetric and the collision is described by an isotropic single particle scattering. In this case, the relaxation time $\tau(k)$ for states whose wave vector has modulus k is given by

$$\int (1 - \cos\theta)\mathcal{Q}(k,\theta)d\Omega = \frac{1}{\tau(k)} \tag{1.7}$$

where $\mathcal{Q}(k,\theta)$ is the transition probability between states whose wave vectors have a relative angle of θ.

Consider a simple example of a normal metal under a small electric field $\vec{E}$. Under the relaxation time approximation, the Boltzmann equation 1.4 can be written as

$$-e\frac{\partial f_k}{\partial \epsilon_k}\vec{E}\cdot\vec{v}_k = -\frac{f_k - f_k^0}{\tau(k)} \tag{1.8}$$

where we have used the fact that the group velocity $\vec{v}_k = \vec{\nabla}_k \epsilon_k/\hbar$ and the equilibrium distribution denoted by f^0 is the Fermi-Dirac distribution. In the small $|\vec{E}|$ limit, we the deviation from equilibrium $\delta f_k \equiv f_k - f_k^0$ is small. Keeping the first order term in $|\vec{E}|$, we obtain the deviation δf_k under a small electric field

$$\delta f_k = e\frac{\partial f_k^0}{\partial \epsilon_k}\vec{E}\cdot\vec{v}_k\tau(k). \tag{1.9}$$

The current associated with this distribution is given by

$$\begin{aligned}\vec{J} &= -2e\int_k \delta f_k\, \vec{v}_k \\ &= 2e^2\int_k \tau(k)\vec{v}_k\left(\vec{v}_k\cdot\vec{E}\right)\left(-\frac{\partial f_0}{\partial\epsilon}\right)\end{aligned} \tag{1.10}$$

where we have used the fact that there is no net current in the equilibrium and the factor 2 comes from the spin degree of freedom. In a typical metal, the Fermi temperature T_F is above the order of $10^4 K$ [4]. Assuming $T \ll T_F$, the derivative of the Fermi-Dirac distribution is simply a delta function at the Fermi energy, or $\partial f_0/\partial\epsilon = -\delta(\epsilon - \epsilon_F)$. As a result, the current can be approximated as a 2d integral over the Fermi surface S_F,

$$\vec{J} = \frac{e^2}{4\pi^3\hbar}\int \tau(k)\frac{\vec{v}_k\vec{v}_k}{|\vec{v}_k|}dS_F\cdot\vec{E}. \tag{1.11}$$

Accordingly, the electrical conductivity tensor is given by

$$\sigma_{\alpha\beta} = \frac{e^2}{4\pi^3\hbar}\int \tau(k)\frac{v_k^\alpha v_k^\beta}{|\vec{v}_k|}dS_F. \tag{1.12}$$

Assuming free electron with quadratic dispersion $\epsilon_k = \hbar^2k^2/2m^*$ and that the relaxation is isotropic, the conductivity tensor becomes

$$\begin{aligned}
\sigma_{\alpha\beta} &= \frac{e^2}{4\pi^3\hbar}\tau_F\int \frac{v_k^\alpha v_k^\beta}{v_F}dS_F \\
&= \delta_{\alpha\beta}\frac{e^2}{4\pi^3\hbar}\tau_F\left(\frac{4\pi k_F^2 v_F}{3}\right) \\
&= \delta_{\alpha\beta}\frac{e^2\tau_F}{m^*}\left(\frac{k_F^3}{3\pi^2}\right) \\
&= \delta_{\alpha\beta}\frac{ne^2\tau_F}{m^*}
\end{aligned} \tag{1.13}$$

where k_F is the fermi wave vector and $\tau_F \equiv \tau(k_F)$ is the relaxation time on the Fermi surface. In conclusion, the electric conductivity from the relaxation time approximation with free electron Eq. 1.13 formally matches the electric conductivity from the Drude model, but with the mean free time replaced by the relaxation time on the Fermi surface.

1.2 Limitations of Boltzmann Transport

Boltzmann transport provides a framework semi-classical transport that is based on the quasiparticle picture. Accordingly, there are certain scenarios where the validity of BTE is challenged. In this section, we discuss two limiting cases which violates the assumption made by the Boltzmann transport. The first case is when the system dimension is small enough such

that the transport is dominated by quantum mechanics. In this so-called ballistic transport regime where Boltzmann equation which neglects quantum coherence become insufficient, the process is more accurately captured by the Landauer formalism. Another case is the failure of the quasiparticles picture, which is the main assumption used in Boltzmann transport. This happens when the mean free paths for the carriers are too short such that the excitations of the system can not be considered as non-interacting quasiparticles. One the most notable examples are bad metals which violates the Mott-Ioffe-Regel limit derived from qualitative arguments regarding the requirement on the mean free path of Landau quasiparticles.

1.2.1 Ballistic Transport

The Boltzmann transport models the transport as diffusions of classical particles. Therefore, its validity is subjected to three relevant length scales to quantum properties, which are the de Broglie wavelength, mean free path of the carriers, and the phase relaxation length that arises from incoherent scatterings. For systems whose dimension is smaller than all of the three, the transport becomes collisionless and remains quantum coherent throughout the process. A prime example of ballistic transport is observed in quantum point contacts within a two-dimensional electron gas (2DEG) created at a GaAs/AlGaAs heterojunction [5]. In this structure, the electron flow is restricted to an extremely narrow channel to allow electron transition through the QPC without scattering. The most striking property of the transport is that conductance shows plateaus at multiples of the conductance quantum $G_0 = 2e^2/h$,

$$G = \nu G_0 \tag{1.14}$$

where ν is a positive integer corresponding to the number of conduction channels in the QPC.

This result can be derived through the Landauer formalism. Assuming the QPC is modeled by a one-dimensional quantum wire and both the input output is smooth such that there is no reflection, the net current that flows through is given by the imbalance between occupations on the two sides. Assuming $T \ll T_F$ such that the electrons are travelling at the Fermi velocity v_F,

$$\begin{aligned} I &= I_{l\to r} - I_{r\to l} \\ &= -ev_F\delta n \end{aligned} \tag{1.15}$$

where δn is the difference between the right movers on the left of the constriction and the left movers on the right, which is given by

$$\delta n = -\frac{g_{1D}eV}{2} \tag{1.16}$$

where $g_{1D} = 2/\pi\hbar v_F$ is the one-dimensional density of states of electrons at the Fermi level. Plugging Eq. 1.16 into Eq. 1.15 yields the relation between the current and the potential difference,

$$I = \frac{2e^2}{h}V = G_0 V. \tag{1.17}$$

Interestingly, the conduction does not depend on any detail of the Fermi surface in one dimension. Accordingly, for a system with ν channels of ballistic transport, the conductivity is simply given by νG_0.

In addition to the nano-scale semiconductor systems, another notable class of one-dimensional

ballistic transport systems are the edge states of a two-dimensional topological material. One of the simplest example of such a system is the integer quantum Hall effect whose edge states are immune to back scattering due to its chirality, resulting in the quantized Hall conductance $\sigma_{xy} = \nu e^2/h$. Note that the Hall conductance quantum e^2/h appears as half of the conductance quantum G_0 of a quantum point contact. This is due to the magnetic field splitting the spin degeneracy, thereby halving the density of states in an one-dimensional energy band. A more recent example is the class DIII topological superconductors, whose edge exhibits helical Majorana states, or the Majorana Kramers pairs. Due to its superconducting nature, the electrical conductance cannot be directly measured, as the supercurrent carries charge without resistance. Instead, the topological nature of these systems manifest itself through quantized thermal conductance. This quantization is a direct consequence of the time-reversal symmetry that protects these helical Majorana modes.

1.2.2 Breakdown of the Quasiparticle Picture

One major assumption made by the Boltzmann transport is the quasiparticle picture, which assumes that the excitation or energy carrier of the system exhibits particle-like behavior. Specifically, this requires that the carriers should be localized and has a well-defined trajectory. In a normal metal, the Debye temperature $T_D \sim 10^2 K$ [6] is orders of magnitude below the Fermi temperature $T_F > 10^4 K$ [4]. In the temperature regime where $T_D \ll T \ll T_F$, the lattice vibrations are classical and but the electron remains degenerate. In this case, the charge transport can be described in terms of classical scattering of quasiparticles at the Fermi surface. The cross section A of the ions that arises from thermal fluctuation is described by the equipartition principle

$$A \sim \left\langle (\delta x)^2 \right\rangle \sim k_B T / k_s \tag{1.18}$$

where curly bracket denotes averaging over thermal distribution and k_s is the characteristic spring constant from the potential energy experienced by an ion in the lattice. This result suggest that the mean free path l of the electron will be inversely proportional to T. That is,

$$l \sim a^3/A \propto T^{-1}, \tag{1.19}$$

where a is the lattice constant. From Eq. 1.13 and using the relation $\tau_F = l/v_F$, we get the resistance $\rho \sim T$. This linear-T resistance is a universal property of normal metals in the high temperature regime.

As mentioned above, Boltzmann transport requires that the quasiparticle in the Fermi liquid has a well-defined trajectory. Equivalently, the Fermi momentum should be greater than the momentum uncertainty, $\hbar k_F > \delta p$, and the mean free path should be greater than the uncertainty in position, $l > \delta x$. Together with the uncertainty principle, the combination of the two inequality yields the Mott-Ioffe-Regel limit,

$$k_F \, l > 1 \tag{1.20}$$

This inequality represents the condition for the minimal mean free path required for the Boltzmann transport to be valid. Interestingly, it was measured in the experiment that certain high-Tc cuprate superconductors exhibits linear-in-T resistance at temperatures above the Mott-Ioffe-Regel limit. This phase of matter are commonly referred to as bad metals, which is one of the central topic in condensed matter physics [7].

In addition to Landau quasiparticles, the carriers of the transport process can be bosonic, which appears as wave packets of some collective excitation of the systems. Examples include

phonons, magnons, plasmons, and Cooper pairs. Due to scattering, such quasiparticles exhibits a finite lifetime, denoted by τ, during which they may collide and decay into other quasiparticles. In the spectral functions, this would cause a broadening in the quasiparticle spectral peak, with the width given by the effective damping coefficient derived from the lifetime $\Gamma = 2/\tau$.

There are multiple qualitative arguments on the condition for a bosonic quasiparticle to be considered well-defined for Boltzmann transport. First, it is necessary that the collective mode associated with the quasiparticles is not overdamped. That is,

$$\Gamma \ll \omega_{qp} \tag{1.21}$$

where ω_{qp} represents the oscillation frequency of the quasiparticle. A more strict condition on the lifetime is that the broadening Γ should be much smaller than the level spacing.

$$\Gamma \ll \Delta\omega_{qp}. \tag{1.22}$$

Qualitatively, violation of this condition will would invalidate the weak coupling assumption inherent in the quasiparticle picture and challenge the linearity of the system. Finally, it is important to note that the argument on the breakdown of quasiparticle picture provided in this section are more of an empirical rule rather than a rigorously derived threshold from first principles. Therefore, the conditions from Eq. 1.20, 1.21, and 1.22 should not be taken as quantitatively accurate boundaries for the Boltzmann transport regime.

1.3 Example Systems for Unconventional Transport

In this thesis, we will discuss three distinct physical systems whose transport is not described by the conventional Boltzmann transport theory with quasiparticles.

1.3.1 Edge of a 2-d Class DIII Topological Superconductor

In the seminal work by Reed and Green [8], it was predicted that in the absence of time reversal symmetry, a 2d topological superconductor exhibits chiral Majorana edge states. Due to the electrical charge neutrality of Majorana fermions and the U(1) symmetry breaking in the bulk, the electrical transport does not exhibit quantization properties like that in an integer quantum Hall system. Instead, the quantized conductance can be observed in the Righi–Leduc effect, which is the thermal analog of the Hall effect. In such a system, the thermal conductance per chiral edge mode is given by

$$\kappa_{xy} = c\frac{\pi^2 k_B^2}{3h}T \equiv c\kappa_0 \tag{1.23}$$

where $c = 1/2$ is the central charge of a single Majorana fermion [8] and κ_0 is commonly known as the thermal conductance quantum, which corresponds to the thermal conductance associated with a single ballistic phonon channel.

Upon restoring time-reversal symmetry, the superconducting system is categorized as class DIII within the Altland-Zirnbauer classification [9]. In this case, Kramers' theorem requires the appearance of a time-reversal copy of the chiral edge states, which results in helical Majorana edge states. Therefore, the chirality on the edge is lost and the thermal Hall conductance κ_{xy} will vanish due to the opposite contribution from the Majorana Kramers' pair. In this case, the

signature of quantized transport from the symmetry protected edge state can be observed in the longitudinal thermal conductance κ_{xx}. Due to the parallel propogating Majorana fermions on the opposite edges, the thermal conductance appears as two times that of a single Majorana fermion,

$$\kappa_{xx} = 2c\kappa_0 = \kappa_0, \tag{1.24}$$

which can be shown directly by a similar derivation from Landauer formalism introduced in Sec. 1.2.1.

In chapter 3, we will introduce a proposal for Majorana zero mode that is inspired by the Fu and Kane tri-junction model but with the topological insulator replaced by a 2d electron gas with spin-orbit interaction. The advantage of our setup is that it does not require an external magnetic field for lifting the degeneracy, which usually degrades the topological gap. The topological phase of this system is controlled by the phases of three s-wave superconductors in proximity. At parameters where the relative proximitized pairing strength from the top and bottom surface is opposite for the two Fermi surfaces, the system becomes a class DIII topological superconductor with the interesting non-Boltzmann transport discussed in the previous paragraph, and the helical Majorana edge states appears when the phase difference between the top and bottom superconductors is π. The appearance of the helical Majorana edge state closes the gap, allowing the topological phase transition of the one dimensional planar Josephson junction at the center of the tri-junction.

1.3.2 1-d Josephson Junction Array across the SIT

An array of Josephson junction exhibits rich transport properties. In the case of a uniform JJ chain, the system is characterized by the Josephson energy E_J and the charging energy between

nearest neighbor island E_{C1} and that with the ground plane E_{C0}. At large E_J, the phase differences across each junctions are small so that the cosine potential can be well approximated by its quadratic component. In this superconducting regime, the quasiparticle are plasmonic modes corresponding to the fluctuation of the phase in the superconductors. It is important to note that while the plasmons can form wave packets much like the phonons in crystals, they are charge neutral so they can only form energy currents. Similar to a homogeneous superconductor, the charge transport in a Josephson junction chain is dominated by the supercurrent from the frictionless flow of the Cooper pairs that is a direct result of quantum coherence, a phenomena that is beyond the Boltzmann transport.

A more interesting property of the Josephson junction array is that as the charging energy E_{C0} increases, it will go through a quantum phase transition to a insulator phase. This so-called superconductor-insulator transition is an example of the Kosterlitz-Thouless transition in the corresponding classical 2d XY model, which can be derived through the standard quantum to classical mapping of the partition function [10]. In ordinary insulators, the electrical transport can be described by a simple thermal activation picture, with carrier density proportional to $e^{-\Delta/k_BT}$, where Δ is the insulating gap. In the presence of disorder, the interference of wave functions can give rise to localized eigenstates [11]. This so-called Anderson localization has a critical dimension of two [12], suggesting that at any level of disorder, all states in the 1-d Josephson junction will have a finite localization length. For finite system size, at weak disorder, this effect gives rise to in-gap states that are localized, while the high-frequency solitons and antisolitons remain extended due to their localization lengths exceeding the system size. Therefore, at low temperature, where the majority of the activated states are localized, the transport is described by the variable-range-hopping model [13]. Finally, the transport becomes Boltzmann-like again in

the insulating phase at high temperature, where the localization length of the activated carriers exceeds the dephasing length from scattering.

In chapter 3, we will discuss the frequency-dependent transport in the Josephson junction array in the insulator regime. Surprisingly, consistent with experiments [1], the high frequency conductance is seen to be dominated by coherent plasmon resonances, even in the insulating regime. This contributes to sharp peaks in the reflection spectrum. We discuss a mechanism based on the sine-Gordon model, where the low frequency conductance is insulating as a result of gapped soliton excitations. In contrast, the high frequency plasmons can be viewed as soliton-antisoliton pairs. We analyze the effects of disorder at the Luther-Emery point. Upon considering a Luther-Emery point that is deep in the insulating phase in the effective sine-Godon model as well as the nearly superfluid regime where the perturbative approach from the microscopic model can be justified, we provide the theory that describes the behavior of the phase mode under weak disorder. In addition, we show that the Josephson junction array with junction and ground capacitance can be reasonably described by the Sine-Gordon model. Our results are consistent with the recent microwave response measurement on the insulating Josephson junction array [1].

1.3.3 Sub-Planckian Heat Transport without Quasiparticles

Charge or energy transport with dissipation time approaching the Planckian time $\tau_P = \hbar/k_B T$, a phenomenon generally referred to as the Planckian transport, has been observed in a wide range of materials [14, 15, 16]. This phenomenon is first observed across various families of metals (heavy fermion, oxide, pnictide, organic metals and conventional metals) in the high temperature regime [14]. In particular, in strongly interacting systems such the high-Tc cuprate,

the Planckian electrical transport apparently persists above the Mott-Ioffe-Regel limit, where the system is expected to enter the regime of transport without quasiparticles. The ubiquitous Planckian transport at temperatures higher than the Debye temperature encourages the conjecture of an existing underlying diffusivity bound [17] that is called the Planckian bound,

$$D \geq v_F^2 \tau_P, \tag{1.25}$$

where v_F is the Fermi velocity. A simpler system where the Planckian diffusivity is observed are complex insulators [15, 18, 19], where the characteristic velocity in Eq. 1.25 is replaced by the longitudinal sound velocity, or $D_{th} \geq v_s^2 \tau_P$ that correspond to the acoustic phonon which is the Goldstone mode of the system.

In chapter 4, we will discuss a classical model of a complex insulator that exhibits sub-Planckian thermal diffusion. It is important to note that the sub-Planckian thermal diffusion is not allowed in the Boltzmann transport regime, as can be shown by combining the condition for the quasiparticle picture in Eq. 1.22 with thermal the conductivity formula [20] derived from the kinetic theory. Our key strategy is to find a system with a large number of incoherent localized phonon excitations that can be described semiclassically. Through including highly nonlinear interaction, we can then achieve such a state where only the sound mode remains coherent with a well-defined sound velocity, while the rest of the motion can not be described as quasiparticles. The thermal diffusivity of this system is then evaluated through numerical simulations and applying the Green's-Kubo formula. Our results shows a thermal diffusivity that scales inversely with the number of internal degrees of freedom, which allows the breaking of the Planckian diffusivity bound.

Chapter 2: Proposal for Majorana Modes without a Magnetic Field in Phase-biased Josephson Tri-junction

2.1 Introduction

The existence of the Majorana fermion was first proposed by Ettore Majorana in 1937 [21]. The original insight was purely theoretical and was discovered through the decomposition of the complex Dirac equation into two real wave equations, resulting in a spin-1/2 particle field that constitutes its own antiparticle. The simple and elegant concept strongly influences multiple research fields across modern physics. In high energy physics, the Majorana fermion was considered a candidate model for many phenomena. Most notably, it was proposed in the original paper that neutrinos are Majorana fermions instead of Dirac fermions. While this idea remains unconfirmed, it has inspired a plethora of valuable research endeavors [22]. More recently, Majorana fermions have even been used to model dark matter under the concept of supersymmetry [23].

In solid-state systems, the building blocks are limited to charged particles such as electrons and ions. Majorana fermions are not expected to be found as elementary particles. Instead, they can only emerge as quasiparticles, which are excitations from a many-body ground state. In the early work on $p + ip$ superconductors [8], it was found that the BdG equation for such a system bears similarity to that of the Majorana fermion from the Dirac equation. Therefore, it exhibits

excitations that are analogous to Majorana fermions in high-energy physics, which possess finite energy and mass. In the context of quantum computation, there is another conceptually different analog concerned with zero-energy collective modes, on which our project will also focus. To differentiate the two, the latter is commonly dubbed as the Majorana zero mode (MZM). In the context of MZM, the analog for an antiparticle in condensed matter physics is the annihilation operator of the corresponding quasi-particle. Accordingly, the operator $\gamma^\dagger$ of an MZM should therefore be a Hermitian operator, or

$$\gamma^\dagger = \gamma. \tag{2.1}$$

A direct consequence of this is that MZM does not have the notion of particle number. In fact, a pair of any two Majorana operators constitutes a fermion operator

$$f = \frac{1}{2}(\gamma_1 + i\gamma_2), \tag{2.2}$$

which also implies that MZMs in any Hamiltonian of electrons must appear in pairs. Following the anti-commutation relation between fermionic operators, $\{c_i^\dagger, c_j\} = \delta_{ij}$ and $\{c_i, c_j\} = \{c_i^\dagger, c_j^\dagger\} = 0$, the MZM satisfies

$$\gamma^2 = \left(\gamma^\dagger\right)^2 = 1. \tag{2.3}$$

An important note is that there is no constraint on the distance between the two MZMs and having a pair of isolated MZMs is indeed required to unveil the property of MZMs in a real-world context. As we will see in the Kitaev chain model, pure separation of the MZM is achieved at the special point $\Delta = t, \mu \neq 0$, where the MZMs perfectly isolated at the first and the last site of the chain.

Due to the charge neutrality that is the direct consequence of its fundamental property, superconductivity, which breaks charge conservation, aligns naturally with the search of MZMs in solid-state systems. This property manifests itself in the form of Bogoliubov quasiparticles, which are usually superposition of creation and annihilation operators. In an s-wave superconductor, the Bogoliubov quasiparticles take the form,

$$\gamma^{\dagger}_{k,\sigma} = u_k c^{\dagger}_{k,\sigma} + v_k c_{-k,\bar{\sigma}} \tag{2.4}$$

Where c are the electron operators and the bar notation denotes opposite spins and $\phi(k) = v_k/u_k$ can be interpreted as the Cooper pair wave function. Although this form is already close to what we need for Majorana at $k = 0$, there is another issue. The requirement of singlet pairing in s-wave superconductors will always form Cooper pairs of opposite spins, and the quasiparticles inevitably become spinful. This will clearly violate Eq. 2.1, as the corresponding anti-particle, or the annihilation operator, must carry the opposite spin. As a result, it is required that the superconductivity for MZM should be formed by "spinless" electrons, or effectively the Cooper pairs should be composed by electrons with parallel spins. Accordingly, as we will discuss in the following subsections, the two seminal models for MZM in 1-d [24] and 2-d [8] are based upon spinless p-wave superconductors. However, the direct implementation of these models faces challenges due to the scarcity of p-wave superconductors and the complexities in isolating one of the spin degrees of freedom. Presently, the most favored approach to induce p-wave superconductivity involves proximitizing s-wave pairing on spin-orbit coupled electrons. This technique is adopted by most proposals we will discuss in this section. Meanwhile, the strategy for isolating the spin degree of freedom typically involves an external Zeeman field, which is

known to weaken the topological gap. Therefore, alternatives are being proposed in more recent developments.

In this chapter, we will introduce a new proposal for Majorana zero modes (MZMs) that does not require an external magnetic field. The structure of this chapter is organized as follows: In Section 2.1, we will explain the two pioneering models for MZMs in 1-D and 2-D. These toy models are based on spinless p-wave superconductors. Towards the realization of MZMs in 1-D, multiple proposals and their corresponding challenges are described in Section 2.1.3. In Section 2.2, we will investigate the Andreev bound state spectrum in two scenarios that go beyond the Andreev limit and are relevant to our proposal. Next, we describe the structure of our setup in Section 2.3. The topological phase boundary of our system is derived and presented in Section 2.4.3. In Section 2.4.4, the topological phase boundary in the case where Cooper pair tunneling is stronger on the opposite sides of the two Fermi surfaces is discussed. In Section 2.5, we demonstrate topological superconductivity by simulating our setup using HgTe as the 2DEG with realistic parameters. The topological gap, which is the lowest Andreev bound state energy, is shown in Section 2.5.4.

2.1.1 MZM in 1-d Spinless p-wave Superconductor

In 2001, three separated groups discovered the existence of zero energy modes at the ends of a one dimensional spinless p-wave superconductor [24, 25, 26], a model that is now known as the Kitaev chain model. The Kitaev chain is paradigmatic not only because it exhibits MZMs in the topological regime but also it contains the key ingredients to realize such a scenario. The

model is presented as a finite N-site chain with nearest neighbor hopping and p-wave superconductivity.

$$H = -\mu \sum_{j=1}^{N} c_j^\dagger c_j - t \sum_{j=1}^{N-1} \left(c_j^\dagger c_{j+1} + h.c. \right) + \Delta \sum_{j=1}^{N-1} \left(c_j^\dagger c_{j+1}^\dagger + h.c. \right) \tag{2.5}$$

where $c_j^\dagger$ represents the creation operator of electron at site j, μ is the chemical potential, t is the nearest neighbor hopping integral, and Δ is the p-wave pairing potential. The isolated Majorana modes in this system are most directly seen by transforming each of the fermion operators into Majorana modes as mentioned above

$$\begin{aligned} c_j &= \frac{1}{2} \left(\gamma_{2j-1} + i\gamma_{2j} \right) \\ c_j^\dagger &= \frac{1}{2} \left(\gamma_{2j-1} - i\gamma_{2j} \right) \end{aligned} \tag{2.6}$$

where γ_{2j-1} and γ_{2j} are Majorana operators for site j. Note that index $2j-1$ and $2j$ does not represents actual relative positions. It is just a convention used to conveniently demonstrate the inter-site pairing between Majoranas. In the transformed basis, the Hamiltonian (Eq. 2.5) becomes,

$$H = -\frac{\mu}{2} \sum_{j=1}^{N} \left(1 + i\gamma_{2j-1}\gamma_{2j} \right) + \frac{i}{2} \sum_{j=1}^{N-1} \left(t + \Delta \right) \gamma_{2j}\gamma_{2j+1} + \left(-t + \Delta \right) \gamma_{2j-1}\gamma_{2j+3}. \tag{2.7}$$

In general, transforming to the Majorana basis does not simplify the Hamiltonian directly. However, in this particular case, it reveals the two topologically distinct limits under specific parameter sets through an extremely elegant way.

- $t = \Delta = 0, \mu \neq 0$:

This is the trivial limit even in the $\{c^\dagger, c\}$ basis, corresponding to uncoupled electron on separated sites with a uniform chemical potential. The Hamiltonian becomes

$$H = -\mu/2 \sum_{j=1}^{N} (1 + i\gamma_{2j-1}\gamma_{2j}) \tag{2.8}$$

whose eigenstates are indeed the single electron states,

$$c_j^\dagger = \frac{1}{2} (\gamma_{2j-1} - i\gamma_{2j}) \tag{2.9}$$

where $[H, c_j^\dagger] = -\mu c_j^\dagger$.

- $\mu = 0, \Delta = t \neq 0$:

  In this limit, we are only left with the second term in the Hamiltonian,

$$H = it \sum_{j=1}^{N-1} \gamma_{2j}\gamma_{2j+1}. \tag{2.10}$$

  In this case, the Majorana modes between adjacent sites are coupled. As mentioned above, we can choose to combine pairs of coupled Majorana modes into a new sets of fermion operators $\tilde{c}_j$,

$$\tilde{c}_j = \frac{1}{2}(\gamma_{2j} + i\gamma_{2j+1}) \tag{2.11}$$

  where $j = 1 \sim N - 1$ and the Hamiltonian becomes

$$H = t \sum_{i=1}^{N-1} \left(\tilde{c}_j^\dagger \tilde{c}_j - \frac{1}{2} \right). \tag{2.12}$$

Therefore, all the excitations in the bulk are gapped with energy t. On the other hand, at the ends of the chain there are two Majorana modes γ_1 and γ_{2N} completely decoupled from the Hamiltonian. Therefore, the fermion operator $\tilde{f} = \frac{1}{2}(\gamma_1 + i\gamma_{2N})$ formed by these two modes is a zero energy excitation of the system.

$$[H, \tilde{f}] = [H, \tilde{f}^\dagger] = 0. \tag{2.13}$$

Note that the appearance of zero energy excitation results in ground state degeneracies. Assuming $|0\rangle$ is a ground state of the system $H|0\rangle = Eg|0\rangle$, then $\tilde{f}|0\rangle$ is also a ground state of the system. The two-fold degeneracy can be distinguished by the fermion parity operator.

$$\begin{aligned} P_F &= (-1)^{\sum_i c_i^\dagger c_i} \\ &= \prod_i \left(1 - 2c_i^\dagger c_i\right) \\ &= \prod_i \left(-i\gamma_{2i-1}\gamma_i\right) \end{aligned} \tag{2.14}$$

and the presence of any Majorana mode flips the sign of fermion parity $\{P_F, \gamma_i\} = 0$.

While we demonstrated that the Kitaev chain displays zero modes for a specific set of parameters, the presence of MZMs is actually a topological characteristic and persists across a broad range of the parameter space. To understand the role of topology in this system, we first look at the bulk Hamiltonian. For the sake of simplicity, we will close the chain and impose the periodic boundary condition $c_{N+1} = c_1$. In momentum space, the Hamiltonian can be written in the usual

Bogoliubov-de Gennes (BdG) form,

$$H = \frac{1}{2}\sum_k C_k^\dagger H_{BdG}(k) C_k \tag{2.15}$$

where $C_k^\dagger = \left(c_k^\dagger, c_{-k}\right)$ is a two-component operator. The $H_{BdG}(k)$ is given by

$$H_{BdG}(k) = \begin{pmatrix} \epsilon_k & \Delta_k \\ \Delta_k^* & -\epsilon_k \end{pmatrix} \tag{2.16}$$

where $\epsilon(k) = -2t\cos k - \mu$ is the single particle energy and $\Delta_k = -2i\Delta \sin k$ is the p-wave pairing potential. Note that H_{BdG} satisfies the particle-hole symmetry by construction, which is defined by the operator $\mathcal{P} = \tau_x K$. That is,

$$\mathcal{P} H_{BdG} \mathcal{P}^{-1} = -H_{BdG} \tag{2.17}$$

Therefore, the eigenstates of H_{BdG} always come in pairs with energies differ by a $-$ sign. This is an artificial result of redundantly including particle and hole operators as separated basis states in the two-component operators C and $C^\dagger$.

We will employ a simple way to visualize the topological differences in the Hamiltonian by examining the evolution of components associated with various Pauli matrices within the Brillouin Zone.

$$H_{BdG}(k) = \vec{h}(k) \cdot \vec{\sigma} \tag{2.18}$$

Due to the fact that $\left(C^{\dagger}_{-k}\right)^{T} = \sigma_x C_k$, $\vec{h}(k)$ and $\vec{h}(-k)$ must have the following relation,

$$h_{x,y}(k) = -h_{x,y}(-k), h_z(k) = h_z(-k). \tag{2.19}$$

Next, we will only focus on the direction of the vector $\vec{h}(k)$ by considering the unit vectors $\hat{d}(k) = \vec{h}(k)/|h(k)|$, this is possible because the bulk Hamiltonian is completely gapped, or $|h(k)| \neq 0$. In two dimensions, the solid angle swept by $\hat{d}(k)$ as k goes around the Brillouin zone corresponds to the Chern number. In one dimension, at the symmetry momentum points $k = 0, \pi$ where $H_{BdG}(k) = H_{BdG}(-k)$, $\hat{d}(k)$ is constraint to locate on the z-axis, or $h_{x,y}(k) = 0$. Let

$$\begin{aligned} \hat{d}(0) &= s_0 \hat{z} \\ \hat{d}(\pi) &= s_\pi \hat{z}. \end{aligned} \tag{2.20}$$

where $s_{0,\pi} = \pm 1$ represents the direction. From the symmetry in Eq. 2.19, we only need to focus on half of the Brillouin zone. As we move from 0 to π, there are two possible cases. If $s_0 s_\pi = -1$, $\hat{d}$, we will end up on the opposite poles, whereas for $s_0 s_\pi$, we will return to the original pole. The description suggests that the quantity

$$Q = s_0 s_\pi \tag{2.21}$$

is indeed the $\mathbb{Z}_2$ invariant to distinguish the two topological phases. Note that Q will remain constant unless there is a gap closing at 0 or π, where $\hat{h}$ becomes not well-defined. This happens for $k = 0$ at $\mu = -2t$ and $k = \pi$ at $\mu = 2t$. Combining these gap closing points, we can conclude

that $Q = 1$ for $|\mu| > 2t$ and $Q = -1$ for $|\mu| < 2t$, assuming the usual case of non-negative t. More generally, in the mathematical form, the $\mathbb{Z}_2$ invariant can be represented by the combined sign of the Pfaffian of the Hamiltonian matrix at the symmetry momenta

$$Q = \text{sign}(Pf[iH(0)]Pf[iH(\pi)]). \tag{2.22}$$

The topological invariant Q is commonly interpreted as the fermion parity. Its changes only when an odd number of gap closings occurs in the Hamiltonian. $Q = 1$ is usually referred to as the trivial phase, in that it can be adiabatically connected to the vacuum state. Conversely, $Q = -1$ denotes the topologically non-trivial phase.

For the special case of $\mu = 0, t = \Delta \neq 0$ where the MZMs appear on the two ends, it clearly correspond to the topologically non-trivial phase. The emergence of a zero mode at the terminal sites of the Kitaev chain for the non-trivial phase can actually be anticipated without directly solving for the eigenstates. Given that the vacuum has $Q = 1$, the topological invariant differs between the vacuum and the bulk of the Kitaev chain, making it impossible to adiabatically link the two without closing the gap. As a consequence, the end sites, serving as the boundary between them, must display zero energy states to bridge these topologically distinct entities. Finally, while the Pfaffian method can be used to determine the topological phase, it's less common in practice. Instead, one often starts from a parameter set known to be trivial and then counts the number of band inversions that occur while adjusting the parameter to the target value.

2.1.2 MZM in 2-d Spinless $p + ip$ Superconductor and the Fu-Kane Proposal

Another great milestone in the pursuit of MZM is the discovery of chiral Majorana zero mode in a 2-d spinless $p + ip$ superconductor by Read and Green in 2000 [8]. The model they study share similar ingredient as the Kitaev chain. It is composed of spinless electrons under a $p + ip$ pairing potential. The Hamiltonian is given by

$$H = \int d^2 r \psi^\dagger(r) \left(-\frac{\nabla^2}{2m} - \mu \right) \psi(r) + \frac{\Delta}{2} \left[\psi(r) \left(\partial_x + i\partial_y \right) \psi(r) + h.c. \right] \tag{2.23}$$

where $\psi(r)$ is the fermion operator at r and Δ represents the strength of the $p+ip$ superconducting pairing. To investigate its topological characteristic, we will follow the method introduced in Sec. 2.1.1 and focus on the bulk Hamiltonian. We first rewrite Eq. 2.23 in its BdG form in the momentum space,

$$H = \frac{1}{2} \int \frac{d^2 k}{2\pi^2} \Psi^\dagger(k) H_{BdG}(k) \Psi(k) \tag{2.24}$$

where $\Psi^\dagger(k) = \left(\psi^\dagger(k), \psi(k) \right)$ and H_{BdG} is given by

$$H_{BdG}(k) = \begin{pmatrix} \epsilon(k) & \tilde{\Delta}^*(k) \\ \tilde{\Delta}(k) & -\epsilon(k) \end{pmatrix}$$

where $\epsilon(k) = k^2/2m - \mu$ and $\tilde{\Delta}(k) = i\Delta(k_x + ik_y)$. As in Eq. 2.18, we represents H_{BdG} in terms of the vector $h(k)$, where

$$h_x(k) = \text{Re}[\tilde{\Delta}(k)]$$
$$h_y(k) = \text{Im}[\tilde{\Delta}(k)]$$
$$h_z(k) = \epsilon_k \tag{2.25}$$

and $\hat{d}(k) = \vec{h}(k)/|h(k)|$. In two dimensions, the manifold mapped out by the momentum space has a well-defined topological invariant called the Chern number $\mathcal{C}$. To put it in mathematical form,

$$\mathcal{C} = \int \frac{d^2k}{4\pi} \hat{d}(k) \cdot \left[\partial_{kx}\hat{d}(k) \times \partial_{ky}\hat{d}(k)\right] \tag{2.26}$$

The Chern number offers a topological characterization of certain quantum systems, fundamentally representing how many times a parameterized map wraps around the unit sphere. Referring to Eq. 2.25, as $|k|$ approaches infinity, the $\hat{d}$ converges to the positive z direction. This implies that the Chern number is solely determined by the behavior of $\hat{d}$ at the origin, namely $\hat{d}(0)$, which in turn is influenced by the sign of the chemical potential. When $\mu < 0$, the direction of $\hat{d}(0)$ points to the north pole, resulting in a Chern number $\mathcal{C}$ of 0. This is indicative of a topologically trivial phase. On the other hand, for $\mu > 0$, $\hat{d}(0) = -\hat{z}$, yielding $\mathcal{C} = -1$. This scenario corresponds to a topologically non-trivial phase.

To study the edge state of such this Hamiltonian, we consider an annulus geometry with a continuous chemical potential $\mu(r) > 0$ for $R_{in} < r < R_{out}$ and $\mu(r) > 0$ otherwise. Working in the low energy limit, we can assume that the eigenstate is slowly varying, which allows a

simplification to the Hamiltonian by dropping the kinetic energy which is quadratic in k. In polar coordinates, the Hamiltonian in Eq. 2.23 becomes

$$H = \frac{1}{2}\int d^2\mathbf{r}\Psi^\dagger(\mathbf{r}) \begin{pmatrix} -\mu(r) & \Delta e^{-i\theta}\left(-\partial_r + \frac{i}{r}\partial_\theta\right) \\ \Delta e^{i\theta}\left(\partial_r + \frac{i}{r}\partial_\theta\right) & \mu(r) \end{pmatrix} \Psi(\mathbf{r}). \tag{2.27}$$

and the quasiparticle wave function $(u(\mathbf{r}), v(\mathbf{r}))^T$ must satisfy the eigenvalue problem,

$$\begin{pmatrix} -\mu(r) & \Delta e^{-i\theta}\left(-\partial_r + \frac{i}{r}\partial_\theta\right) \\ \Delta e^{i\theta}\left(\partial_r + \frac{i}{r}\partial_\theta\right) & \mu(r) \end{pmatrix} \begin{pmatrix} u(\mathbf{r}) \\ v(\mathbf{r}) \end{pmatrix} = E \begin{pmatrix} u(\mathbf{r}) \\ v(\mathbf{r}) \end{pmatrix} \tag{2.28}$$

Due to the $e^{i\theta}$ term in the off-diagonal matrix element, the Hamiltonian couples different angular momentum sectors. Accordingly, we can formulate an ansatz for the wave function as

$$\begin{pmatrix} u(\mathbf{r}) \\ v(\mathbf{r}) \end{pmatrix} = e^{im\theta} \begin{pmatrix} \frac{f(r)}{\sqrt{r}} \\ \frac{e^{i\theta}g(r)}{\sqrt{r}} \end{pmatrix} \tag{2.29}$$

where $m \in \mathcal{Z}$ to satisfy the 2π periodicity in θ for the wave function. By pluging Eq. 2.29 into Eq.2.28, we get,

$$\begin{pmatrix} -\mu(r) & \Delta\left(-\partial_r - \frac{m+1/2}{r}\right) \\ \Delta\left(\partial_r - \frac{m+1/2}{r}\right) & \mu(r) \end{pmatrix} \begin{pmatrix} f(r) \\ g(r) \end{pmatrix} = E \begin{pmatrix} f(r) \\ g(r). \end{pmatrix}$$

We first consider the limit $R_{in} \gg \Delta(m+1/2)/\mu$ so that near the inner interface between $\mu < 0$

and $\mu > 0$, the term $\Delta(m + 1/2)/r$ is negligible. In this case, the matrix becomes

$$H = -\mu(r)\sigma_z - \Delta i\partial_r\sigma_y. \tag{2.30}$$

The given expression aligns closely with the celebrated Jackiw-Rebbi model as presented in Ref. [27]. In this context, the term $\mu(r)$ is mapped to the fermion mass. An important feature of the Jackiw-Rebbi model is its prediction concerning interfaces: specifically, wherever there's a transition or interface where this effective fermion mass changes sign, a localized zero-energy eigenstate emerges. Therefore, we can expect the existence of a zero energy states that circulate the inner edge of the annulus. The process for getting the outer edge state is formally similar and the same argument from Jackiw-Rebbi model also applies. The result is a pair of chiral edge states propagating in the opposite direction. The eigenvectors are given by

$$\begin{aligned}
\begin{pmatrix} f_{in}(\mathbf{r}) \\ g_{in}(\mathbf{r}) \end{pmatrix} &= e^{-\frac{1}{\Delta}\int_{R_{in}}^{r}\mu(r')dr'} \begin{pmatrix} 1 \\ 1 \end{pmatrix} \\
\begin{pmatrix} f_{out}(\mathbf{r}) \\ g_{out}(\mathbf{r}) \end{pmatrix} &= e^{\frac{1}{\Delta}\int_{R_{out}}^{r}\mu(r')dr'} \begin{pmatrix} i \\ -i \end{pmatrix}
\end{aligned} \tag{2.31}$$

where we the normalization factor is ignored.

The edge states move away from zero energy if we consider the correction from $H' = -\Delta(m + 1/2)/r\sigma_x$, which gives the first-order energy correction $\epsilon^{(1)}_{m,in} = -\Delta(m + 1/2)/R_{in}$ and $\epsilon^{(1)}_{m,out} = \Delta(m + 1/2)/R_{out}$. Since m only takes integer values, $\epsilon^{(1)}$ can not vanish and there is no zero energy state on the edges. Note that this does not contradict with the above argument that between systems with distinct topology there exists gapless mode. The reason is that the

finite sized annulus does not strictly satisfy the condition of bulk. So the gapless property is only guaranteed in the limit $R_{in}, R_{out} \to \infty$.

The reason for the existence of the gap comes from the $e^{\pm i\theta}$ factor in the off-diagonal terms that is intrinsic to the $p + ip$ superconductivity. Under a gauge transformation $\psi \to e^{i\theta/2}\psi$ to explicitly remove this extra phase, the fermion operators become anti-periodic in θ, resulting in half-integer angular momentum along z. This is precisely the origin of the $1/2$ we see in the first-order energy correction.

The simplest way to remove this gap is to remove this phase factor by adding an extra phase winding to the superconductor $\Delta \to e^{-i\theta}\Delta$. This corresponds to threading a flux quantum $\Phi_0 = h/2e$ through the superconductor. Intuitively, this creates an extra Aharonov-Bohm phase of π, restoring the periodic boundary condition on θ. on the qusiparticle wave function $(u, v)^T$, thereby removing the half integer part in the angular momentum. As a result, the eigenstate energy becomes $\epsilon_{m,in} = -m\Delta/R_{in}$ and $\epsilon_{m,out} = m\Delta/R_{out}$ and the system becomes gapless ($m = 0$) even for a finite size annulus. In fact, the two edge states at $m = 0$ are MZMs, whose operator is given by

$$\chi_{in} = e^{-\frac{1}{\Delta}\int_{R_{in}}^{r}\mu(r')dr'}\begin{pmatrix}1\\1\end{pmatrix}$$
$$\chi_{out} = e^{\frac{1}{\Delta}\int_{R_{out}}^{r}\mu(r')dr'}\begin{pmatrix}i\\-i\end{pmatrix} \tag{2.32}$$

which satisfy $\gamma = \Psi^T \cdot \chi = \gamma^\dagger$. To achieve the 2d $p + ip$ spinless superconductor, the primary challenges are to suppress one of the spin degrees of freedom and to induce $p+ip$ superconductivity

in the system.

In the groundbreaking work by Fu and Kane in 2008 [28], a new proposal that utilize the surface of a strong topological insulator (TI) to realize this model is introduced. The surface of a strong TI can be described by a Dirac cone Hamiltonian given by,

$$H_0 = \psi^\dagger(-iv\vec{\sigma}\cdot\nabla - \mu)\psi \tag{2.33}$$

where $\psi = (\psi_\uparrow, \psi_\downarrow)$ and $\sigma = (\sigma_x, \sigma_y)$. Note that The Hamiltonian is time reversal invariant, or $\mathcal{T}\mathcal{H}_0\mathcal{T}^{-1} = \mathcal{H}_0$, where $\mathcal{H}_0$ is the 2 by 2 matrix in H_0 and the time reversal operator in spin-1/2 is $\mathcal{T} = i\sigma_y\mathcal{K}$. On this surface, Fu and Kane consider the effect of an s-wave superconductivity on the system. In practice, this can be done through bringing an s-wave superconductor in close proximity to allow Cooper pairs to diffuse onto the surface of the strong TI. In terms of the Nambu spinor $\Psi(\mathbf{r}) = (\psi_\uparrow(\mathbf{r}), \psi_\downarrow(\mathbf{r}), \psi_\downarrow^\dagger(\mathbf{r}), -\psi_\uparrow^\dagger(\mathbf{r}))^T$, the Hamiltonian becomes $H = \int_{\mathbf{r}} \Psi^\dagger(\mathbf{r})\mathcal{H}\Psi(\mathbf{r})/2$ and

$$\mathcal{H} = -iv\tau_z\vec{\sigma}\cdot\nabla - \mu\tau_z\Delta_0\left(\cos\phi\tau_x + \sin\phi\tau_y\right) \tag{2.34}$$

where $\tau_{x,y,z}$ are Pauli matrices for the particle-hole space, Δ_0 is the magnitude of the pairing potential and ϕ is the phase of the s-wave superconductor. The kinetic part of the Hamiltonian in momentum space is diagonalized by the operator $c_k = \psi_\uparrow(k) + e^{i\theta_k}\psi_\downarrow(k)$, where the symmetry of the pairing becomes the $p + ip$.

$$H = \sum_k (v|k| - \mu)c_k^\dagger c_k + \Delta_0\left[(k_x + ik_y)c_k c_{-k} + h.c.\right] \tag{2.35}$$

Note that this Hamiltonian becomes formally similar to the spinless $p + ip$ model introduced in Eq. 2.23 at high enough chemical potential $\mu \gg \Delta_0$ such that the quadratic dispersion can be approximated by its linear term. Therefore, most of the knowledge we gain from solving the spinless $p + ip$ model applies directly. An important difference is that the Fu-Kane Hamiltonian remains time reversal symmetric, while the spinless model does not. This has the benefit that the topological gap is robust against non-magnetic disorder.

For the chiral edge mode that exists on the edges in the spinless model, it does not come naturally in the Fu-Kane model as the surface of the 3d strong TI does not have a boundary. To create an edge, as suggested by Fu and Kane, one can introduce a mass term $M\sigma_z$ that suppresses superconductivity by depositing superconducting and insulating magnetic materials on the TI. In this case, the chiral edge states can appear. In a spin-1/2 system with time reversal symmetry, the eigenstates must form Kramers pairs, resulting in the Hamiltonian displaying a two-fold degeneracy. To induce isolated MZM, a mechanism to lift this degeneracy is required. One way to achieve this would be to introduce a flux quantum Φ_0 as mentioned above, and the MZM can reside on the edge of the vortex. Fu and Kane ingeniously proposed a method to emulate a 2π phase winding in the superconductor. This is achieved by employing three superconducting leads with detuned superconducting phases to form a vortex. Such a trijunction setup can capture an MZM at its core. By developing a network of these structures, more intricate manipulations of MZMs can be realized. It is later proven that phase winding is a necessary condition for topological superconductors in multiterminal junction set-ups [29]. The main experimental challenge towards realizing this proposal lies in achieving strong proximitized pairing into the surface of the topological insulator. Recent experiments with deposition of Pd on TIs BiSbTeSe2 [30, 31] and WTe2 [32] have reported progress in the transparency of the SC-TI

interface.

2.1.3 Realization of Topological Superconductors in 1d

In this section, we will overview the some of the important proposals towards the realization of topological superconductors predicted in the spinless p-wave superconductors [8, 24, 26] which are characterized by the occurrence of localized zero-energy MZMs. This has been a great effort in the field of condensed matter physics for over a decade primarily because of its potential application to topological quantum computation [24, 33, 34, 35, 36]. This system is considered ideal for quantum information applications for two main reasons. First, the Majorana zero modes are robust against the usual phase and charge quantum errors due to their localization nature. Second, the Majorana modes exhibit non-Abelien braiding statistics, which enables the realization of logical gates in topological quantum computation [36, 37]. Without time-reversal symmetry, the system belongs to class D in the Altland–Zirnbauer classification [9], where the $\mathbb{Z}_2$ topological invariant corresponds to the ground state fermion parity. In the topological regime or odd fermion parity, two unpaired localized Majorana zero modes appear at the opposite ends of the chain, which are robust as long as the superconducting gap remains finite.

A large number of designs have been proposed and studied [38, 39, 40, 41, 42, 43, 44, 45, 46] for the realization of MZMs in the 1-d systems. The conceptually simplest way to realize the Kitaev chain is through proximitizing an s-wave superconductivity to the edge of a 2d TI [47]. The edge of a 2d TI is characterized by helical edge states where opposite spins travels in the opposite direction. Through applying a Zeeman field h, the counter propagating modes hybridize and form two separated bands. Due to the momentum dependent spin direction, the spins are

misaligned on the same band. As a result, in the presence of an s-wave pairing potential Δ, the two bands naturally exhibits intraband coupling which exhibits a p-wave symmetry. In the regime where $h \gg \Delta$ and the chemical potential being closed to the upper band minimum, an effective Kitaev Chain model can be achieved. To put this proposal in to practice, the primary challenge is the requirement of a 2d TI. The discoveries and characterizations of 2D TIs remain active areas of research, with ongoing advancements. [48].

Towards replacing topological insulators, ideas around combining the spin-orbit effect and magnetic field were put forth. A particularly simple design for Majorana zero mode is the superconductor-semiconductor heterostructure [39, 40, 41, 42], also known as the Majorana nanowires. This set-up consists of a one-dimensional semiconductor (Eg. InAs or InSb) with Rashba spin-orbit coupling and proximitized s-wave superconductivity. Unlike the tri-junction set-up, the mechanism for time-reversal symmetry breaking is a strong external magnetic field parallel to the wire. The Zeeman term opens an energy gap at the degeneracy point ($k_x = 0$) between the two bands that are split by the spin-orbit coupling, thereby creating a window for an odd number of Fermi points in the half Brillouin zone [24]. Due to the simplicity of this model, extensive experiments and theoretical simulation in the real experimental context have been performed [49]. A major challenge for these proposals is that the topological phase requires a limited range of chemical potential, which can be difficult to control in systems that are in contact with a superconductor. Additionally, the topological gap in such systems, which is determined by the superconductivity, is usually degraded due to the requirement of a strong magnetic field [50]. Therefore, the appearance of Majorana zero modes in this system requires careful control of the disorder, such as the impurities at the semiconductor-superconductor interface [51].

As mentioned above, to have more robust Majorana zero modes, it is desirable to reduce

the magnetic field. To this end, designs that rely on phase control in the superconductor to break time-reversal symmetry were proposed [52]. Extension models of Majorana nanowires include driving a supercurrent through the s-wave superconductor [53] and using magnetic flux to induce Majorana zero mode [54]. In the latter case, the geometry of the s-wave superconductor is changed to a cylindrical shell that wraps around the semiconductor nanowire, where an emergent Zeeman field can appear in the presence of an odd number of windings in the SC phase, due to angular momentum conservation. A similar design was also discussed in the context of a topological insulator nanowire [55].

Another important proposal is the so-called planar Josephson junction introduced in Refs. [56, 57], which is made up of a Rashba spin-orbit coupled 2DEG between two s-wave superconductors with a phase difference ϕ. In the absence of an in-plane magnetic field, the ABS spectra for the two Fermi surfaces that corresponds to opposite spins are degenerate and cross zero energy at $\phi = \pi$. This degeneracy can be lifted by an in-plane magnetic field, where the zero energy ϕ shifts toward the opposite directions, thereby opening up a topological regime in ϕ. The advantage of this set-up is that it exhibits robust Majorana zero modes in a wide parameter regime of magnetic field and chemical potential at $\phi \approx \pi$, where the critical field is determined by the Thouless energy scale $(\pi/2)v_F/W$, where v_F is the Fermi velocity and W is the junction width. Therefore, by increasing the width of the Josephson junction, one can decrease the critical Zeeman energy. Nevertheless, the ABS energy, which is the topological gap of the system, is inversely proportional to the width in the wide junction limit ($\sim 1/W^2$). As a result, a tradeoff exists between decreasing the critical Zeeman field and having a large topological gap. Recent experiments [58, 59, 60, 61] on the planar Josephson junction have observed signatures of the topological phase transition. On the other hand, attempts were also made to remove the Zeeman

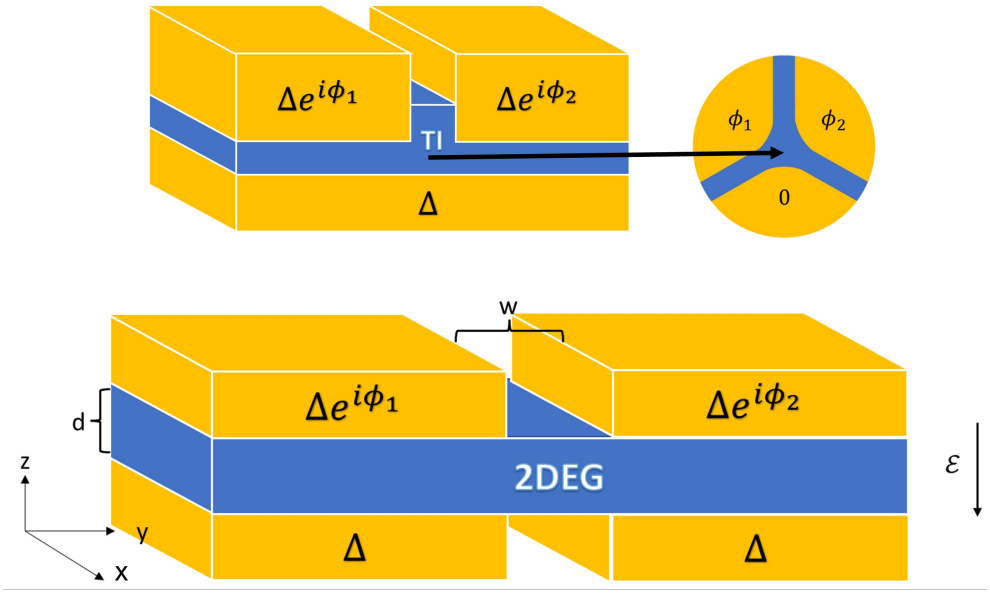

Figure 2.1: (Top panel) A set-up of the Fu and Kane tri-junction model which is topologically similar to our set-up in the top panel with the 2DEG replaced by a thick 3d TI. An MBS can appear at the intersection of the tri-junction when the three phases $(0, \phi_1, \phi_2)$ form a vortex. (Bottom panel) Our proposed set-up for MBS. Four s-wave superconductors are in contact with a quasi-2d spin-orbit coupled semiconductor. An external electric field $\mathcal{E}$ points to the $-z$ direction through the whole 2DEG. The MBS pair is expected to appear at the two ends of the planar Josephson junction in the middle as the phases $\phi_{1,2}$ are tuned across a topological phase transition.

field from the system completely. Such designs include biasing the phase of the superconductors in the direction parallel to the Josephson junction [62], where a supercurrent to break time-reversal symmetry driven along the Josephson junction. Another example system is an SNSNS junction set-up [63] with the three superconductors biased to phases $(-\theta, \phi, \theta)$, which allows a window for Majorana zero mode in the $\theta - \phi$ space when there is inequality between the Fermi velocities of the two Fermi surfaces.

In this project, we propose a family of devices (see Fig. 2.1) for MZM without a Zeeman field that interpolates between a topological insulator thin film to a spin-orbit coupled semiconductor. We will find that the device also support a class DIII at a phase boundary of the topological superconducting phase [64]. Our system is controlled by three s-wave superconductor phases

$(0, \phi_1, \phi_2)$ [29]. An external electric field in the vertical direction is used to control the strength of the proximity effect at the top and bottom interface, whose mechanism will be discussed in more detail in Sec. 2.4.2. Utilizing the inequality in the Cooper pair tunneling amplitude across the boundary for the two Fermi surfaces, the system can be tuned into a topological superconductor, where a pair of Majorana zero modes appear at the two ends of the normal region in the middle. When the phase bias $\phi_{1,2}$ on one of the sides is at a time-reversal symmetric point (0 or π), the side becomes a two-dimensional class DIII system, whose $\mathcal{Z}_2$ topological invariant corresponds to the parity of the number of Fermi surfaces with a negative pairing potential that encloses a time-reversal invariant momentum [64, 65, 66, 67, 68]. In the parameter regime where the proximity effect is stronger on the opposite interfaces for the two Fermi surfaces, the system is topological at $\phi = \pi$, hosting helical Majorana edge modes at the boundary. Note that the mechanism for topological superconductivity is similar to the one-dimensional system proposed in Ref. [69], but here an electric field is required to break the mirror symmetry in the z direction explicitly.

2.2 Andreev Bound State Spectrum Beyond the Andreev Limit

In our system, the MZM originates from the planar Josephson junction, with its topological properties mainly influenced by the evolution of the Andreev bound state [70] (ABS) spectrum. In the well-known Andreev limit, where the chemical potential μ is much greater than the pairing strength $|\Delta|$ and the junction's width $w \to 0$, the ABS energy is given by the simple form $\Delta \cos(\phi_1 - \phi_2)$, where ϕ_1 and ϕ_2 are the phases of the superconductor on the two sides of the junction. In this section, we derive the ABS energy for two particular scenarios that is relevant to our proposal. In Sec. 2.2.1, we address a situation where band curvature is significant, typically

encountered near band minima. Next, in Sec. 2.2.2 we will examine the effect of varied pairing strengths on the ABS energy.

2.2.1 ABS Spectrum Close to the Band Minimum

We consider a spinless 1d s-n-s Josephson junction described by the Hamiltonian

$$H(x) = H_0 + \left[\Theta(x - d/2)e^{i\phi/2} + \Theta(-d/2 - x)e^{-i\phi/2}\right] H_{sc}, \tag{2.36}$$

where d is the width of the junction and ϕ is the superconducting phase difference across the junction. Close to the band minima, we assume quadratic dispersion for H_0,

$$\begin{aligned} H_0 &= \int_x \Psi^\dagger(x)(-\partial_x^2/2m - \mu)\Psi(x) \\ H_{sc} &= \int_x \int_y \Delta(x-y)\Psi^\dagger(x)\Psi^\dagger(y) + h.c. \end{aligned} \tag{2.37}$$

On the two superconductor sides, the wave function in the spinor representation $\gamma_k^\dagger = u_k c_k^\dagger + v_k c_{-k}$ satisfies the Bogoliubov-de Gennes equation given by

$$\begin{pmatrix} \frac{k^2}{2m} - \mu & \Delta(k) \\ \Delta^*(k) & -\frac{k^2}{2m} + \mu \end{pmatrix} \begin{pmatrix} u_k \\ v_k \end{pmatrix} = E \begin{pmatrix} u_k \\ v_k \end{pmatrix} \tag{2.38}$$

where we assume the p-wave form $\Delta(k) = \Delta_0 e^{-i\theta(k)}$. This gives the relation between the momentum k and energy E

$$k = \pm\sqrt{2m\left(\mu \pm \sqrt{E^2 - \Delta_0^2}\right)}. \tag{2.39}$$

The ABSs are in-gap states ($|E| < \Delta_0$) whose wave function decays exponentially within the superconductors. That is, for $x > d/2$, $k = \kappa$ or $-\kappa^*$ and for $x < -d/2$, $k = -\kappa$ or κ^*, where

$$\kappa = \sqrt{2m\left(\mu + \sqrt{E^2 - \Delta_0^2}\right)} \tag{2.40}$$

and in the middle ($-d/2 < x < d/2$), $k = \pm q_e$ or $\pm q_h$, where

$$\begin{aligned} q_e &= \sqrt{2m(\mu + E)} \\ q_h &= \sqrt{2m(\mu - E)}. \end{aligned} \tag{2.41}$$

Consequently, the wave function in the three regions satisfies the general form

$$\begin{aligned} |\psi_L\rangle &= A_L \begin{pmatrix} e^{-i\phi/2}\Delta(-\kappa) \\ E - \sqrt{E^2 - \Delta_0^2} \end{pmatrix} e^{-i\kappa x} \\ &\quad + B_L \begin{pmatrix} e^{-i\phi/2}\Delta(\kappa^*) \\ E + \sqrt{E^2 - \Delta_0^2} \end{pmatrix} e^{i\kappa^* x} \\ |\psi_M\rangle &= \begin{pmatrix} A_M e^{iq_e x} + B_M e^{-iq_e x} \\ C_M e^{iq_h x} + D_M e^{-iq_h x} \end{pmatrix} \\ |\psi_R\rangle &= A_R \begin{pmatrix} e^{i\phi/2}\Delta(\kappa) \\ E - \sqrt{E^2 - \Delta_0^2} \end{pmatrix} e^{i\kappa x} \\ &\quad + B_R \begin{pmatrix} e^{i\phi/2}\Delta(-\kappa^*) \\ E + \sqrt{E^2 - \Delta_0^2} \end{pmatrix} e^{-i\kappa^* x} \end{aligned} \tag{2.42}$$

By imposing the continuity condition at the boundaries $x = \pm d/2$, one can solve for the Andreev spectrum.

In the Andreev limit $\xi_0 \gg \lambda_F$ or equivalently, $\mu \gg \Delta_0$, the set boundary condition for the states in Eq. 2.42 is particularly simple, and the ABS energy is given by the usual form [71]

$$\frac{E}{\Delta_0} = \pm \cos\left(\bar{w}\frac{E}{\Delta_0} + \frac{\phi}{2}\right), \tag{2.43}$$

where $\bar{w} = w/(\hat{p}\cdot\hat{n}\xi_0)$ is the effective width measured by the coherence length $\xi_0 = v_F/\Delta_0$.

2.2.2 ABS Spectrum between Superconductors of Different Pairing Amplitude

As introduced in Ref. [72, 73], the ABS spectrum in an SNS junction can be obtained through the scattering theory of the BdG Hamiltonian with the step function pairing potential. In the Andreev limit $\mu \gg |\Delta|$ and considering the bound state regime $E < |\Delta|$, pure Andreev reflection happens at an ideal NS interface. The reflection coefficients can be obtained by considering the continuous boundary conditions at the 0^{th} order in E/μ and $|\Delta|/\mu$, which are given by

$$\begin{aligned} r_{ee} &= 0 \\ r_{hh} &= 0 \\ r_{he} &= e^{-i(\phi+\beta)} \\ r_{eh} &= e^{i(\phi-\beta)} \end{aligned} \tag{2.44}$$

where $\beta = \arccos(E/|\Delta|)$ and ϕ is the order parameter phase of the superconductor. On the other hand, across the normal metal, the transmission amplitude is simply the phase acquired by

the plane wave $t_{e/h}(k, \Delta y) = \exp(\pm ik\Delta y)$, and the momentum of the electron and hole branch can be approximated by the linear relation $k_{e/h}(E) \approx k_F \pm E/v_F$. The quantization condition is that the transmission amplitude of a round trip equals unity. That is,

$$t_{\circlearrowleft} = r_{he}^{R} t_h \left(-k(E), -w\right) r_{eh}^{L} t_e \left(k(E), w\right) = 1. \tag{2.45}$$

Assuming the order parameters on the left/right superconductors to be $\Delta_{L/R} e^{i\phi_{L/R}}$, the ABS energy satisfies

$$2w\frac{E}{v_F} - \arccos\left(E/\Delta_L\right) - \arccos\left(E/\Delta_R\right) = 2n\pi + \Delta\phi \tag{2.46}$$

where $\Delta\phi \equiv \phi_R - \phi_L$. Note that the Eq. 2.46 can be reduced to Eq. 2.43 when taking the superconducting strength to be equal on both sides $\Delta_L = \Delta_R = \Delta_0$,

An important property of Eq. 2.46 is that at $\phi = \pi$ there is always a zero energy ABS. This band inversion point $\phi = \pi$ is independent of the relative superconducting strength of the two superconductors. As a result, the topological phase boundary of the planar Josephson junction can be determined solely by the effective phase difference across the Josephson junction for different Fermi surfaces at the symmetry point $k_x = 0$.

2.3 Proposal: Tri-junction Setup

2.3.1 Connection to the Fu and Kane Tri-junction

Our proposal to realize Majorana modes without external magnetic fields is topologically similar to the tri-junction proposal by Fu and Kane in Ref. [28] where superconductors are deposited to cover all faces of a thick 3d topological insulator (TI) as illustrated in Fig. 2.1. The uncovered regions on the sides of the TI will become a planar Josephson junction along the y direction whose tunneling current is carried by the surface state. Together with the Josephson junction between the top superconductors, a tri-junction structure is formed at the intersection of the top and side Josephson junctions. In the presence of the proximitized s-wave pairing, the surface of the strong TI forms an effective p+ip superconductor, which allows the tri-junction to trap a Majorana bound state (MBS) when the three phases ϕ_1, ϕ_2 and $\phi = 0$ (bottom superconductor) forms a vortex [28].

2.3.2 Elimination of 3D Bulk TI

The central question we focus on is whether the bulk 3D TI in Fig. 2.1 can be replaced by a spin-orbit coupled semiconductor. A TI slab is technically a quasi two-dimensional structure and one expects the vortex Majorana modes to be robust as long as the overlap between surface states is small enough. In this work, we focus on the opposite limit where we replace the TI by a spin-orbit coupled semiconductors slab that is thin enough in the z direction so that the separation of energy levels is much greater than the energy gap of the superconductors . In this limit, similar to a TI, the semiconductor will have a single spin split Fermi surface before

including superconductivity.

Our setup is depicted in the bottom panel of Fig. 2.1. We consider a 2DEG with spin-orbit coupling in proximity to four s-wave superconductors under an external electric field in the $-z$ direction. The phases of the two bottom superconductors are fixed to be $\phi = 0$ while the top two have phases $\phi_{1,2}$. The separation between the bottom superconductors does not have any theoretical relevance other than it allows for the possibility of dual gating where the electric field and electron density in the junction can be controlled independently. The thickness d of the 2DEG and gap width w between the superconductors on the left and right sides are assumed to be smaller than the coherent length ξ of the superconductors, forming a planar Josephson junction in the middle. Finally, translational symmetry is assumed in the x direction.

The split bands from the spin-orbit interaction will create multiple fermi surfaces in the two-dimensional momentum space. These fermi surfaces form the basis states of the ABS in the planar Josephson junction at the middle that is along the x direction. Similar to the proposal by Fu and Kane, our system exhibits particle-hole symmetry due to proximitized superconductivity, while time-reversal symmetry is broken from the phase bias $\phi_{1,2}$. Therefore, it belongs to class D in the Altland–Zirnbauer classification [9]. The Z_2 topological invariant in the junction is described by the fermion parity [24], which will be determined by the Andreev spectrum.

As we will show in Sec. 2.4.1, through the application of an external electric field E that breaks the mirror symmetry in the z direction, the band inversion points of the split bands can be separated in the ϕ_1, ϕ_2 space. The separation of band inversion points at the symmetry momentum $k_x = 0$ then creates windows for odd fermion parity, where the system becomes topological and the MBSs appear at the ends of the planar Josephson junction. The resulting topological phase diagram of our setup will be similar and, in specific parameter regimes, identical to the phase

diagram of the Fu and Kane tri-junction model.

2.4 Model

2.4.1 Proximitized p-wave Pairing in the 2DEG

We consider a 2DEG described by the Hamiltonian,

$$H = H_0 + H_D \tag{2.47}$$

with $H_0 = (p_x^2 + p_y^2 + p_z^2)/2m + V(z)$ where $V(z)$ is the confinement potential $V(z) = 0$ for $0 \leq z \leq d$ and ∞ otherwise. H_D represents a Dresselhaus spin-orbit interaction

$$H_D \sim p_x(p_y^2 - p_z^2)\sigma_x + p_y(p_z^2 - p_x^2)\sigma_y + p_z(p_x^2 - p_y^2)\sigma_z \tag{2.48}$$

Due to the z confinement, we can assume $\langle p_z^2 \rangle \gg \langle p_x^2 \rangle, \langle p_y^2 \rangle$ in the low energy limit. In this case, the leading order effect is the linear Dresselhaus effect in the $x - y$ plane.

$$H^{(0)} = \frac{1}{2m}\left(p_x^2 + p_y^2\right) + \frac{\beta}{\hbar}\left(-p_x\sigma_x + p_y\sigma_y\right) \tag{2.49}$$

The eigen-energy is given by

$$\varepsilon_{\pm}(\vec{p}) = \frac{p^2}{2m} \pm \frac{\beta}{\hbar}p \tag{2.50}$$

where $p = \sqrt{p_x^2 + p_y^2}$ and the corresponding fermion operators are

$$\begin{pmatrix} c^\dagger_{k,+} \\ c^\dagger_{k,-} \end{pmatrix} = \frac{1}{\sqrt{2}} \begin{pmatrix} e^{i\theta_k} & 1 \\ e^{i\theta_k} & -1 \end{pmatrix} \begin{pmatrix} c^\dagger_{k,\uparrow} \\ c^\dagger_{k,\downarrow} \end{pmatrix} \tag{2.51}$$

where $\theta_k = \tan^{-1}(k_y/k_x)$ is the polar angle of momentum k in the k_x-k_y plane.

Next, we consider a proximitized s-wave superconductivity,

$$H_{sc} = \Delta \sum_k c^\dagger_{k,\uparrow} c^\dagger_{-k,\downarrow} + h.c. \tag{2.52}$$

Plugging in Eq. 2.51 into Eq. 2.52 leads to a pairing potential that takes the $p + ip$ form.

$$H_{sc} = \frac{\Delta}{2} \sum_k e^{-i\theta_k} \left(c^\dagger_{k,+} c^\dagger_{-k,+} - c^\dagger_{k,-} c^\dagger_{-k,-} \right) + h.c. \tag{2.53}$$

As a result, in the presence of a proximitized s-wave pairing, the split bands ($\pm$) from Dresselhaus spin-orbit coupling exhibit spinless p-wave superconductivity separately.

2.4.2 Effective Pairing Potential from the Two Surfaces

Next, we consider one side of the Josephson junction as in Fig. 2.1 with a pair of s-wave superconductors attached to the top and bottom surfaces of the 2DEG. As described in Sec. 2.4.1, the p-wave pairing potential acts separately on the two Fermi surfaces. We assume phase bias ϕ for the superconductor at the top surface and phase 0 for the superconductor at the bottom surface.

The proximitized pairing potential across an SN interface is determined by the tunneling

amplitude from the superconductor into the 2DEG [74], which depends on the partial derivative of the wave function in the z direction at the boundaries [75]. That is, $\Delta \propto |\partial_z \varphi(z = z_0)|^2$ where $z_0 \in \{0, d\}$. In the limit $d \ll \xi$, the effective pairing potential is simply the sum of contributions from the top and bottom superconductors

$$\Delta_{\text{eff}} = \Delta_b + \Delta_t \tag{2.54}$$

where

$$\begin{aligned} \Delta_t &\propto |\partial_z \varphi(z = d)|^2 \\ \Delta_b &\propto |\partial_z \varphi(z = 0)|^2 \end{aligned} \tag{2.55}$$

Assuming both superconductors has the same pairing strength, the effective pairing potential can be expressed as

$$\Delta_{\text{eff}} = \Delta_0 \left(|\partial_z \varphi(z = 0)|^2 + |\partial_z \varphi(z = d)|^2 e^{i\phi} \right). \tag{2.56}$$

2.4.3 Topological Phase Boundaries

The quasi 1-d Josephson junction in the middle exhibits particle-hole symmetry but time-reversal symmetry is absent. Therefore, it belongs to class D in the AZ classes [9]. As discussed in Ref. [24] by Kitaev, the Z_2 topological invariant in this system corresponds to the fermion parity, which flips whenever an odd number of superconducting gap closing appears in the band structure. Due to the mirror symmetry in the x direction $(x, \sigma_x) \to (-x, -\sigma_x)$, the ABS energies for the two Fermi surfaces are doubly degenerate for $k_x \neq 0$, or $E_{\text{ABS}\pm}(k_x, k_y) =$

$E_{\text{ABS}\pm}(-k_x, k_y)$. Therefore, the topological invariant is determined solely by the fermion parity at the symmetry point $k_x = 0$.

Focusing on states at $k_x = 0$, the system becomes one-dimensional. Dropping the subscripts in k_y for simplicity, the Josephson junction formed by the two Fermi surfaces is described by the Hamiltonian

$$H_\pm = \sum_k \left(\varepsilon_\pm(k) - \mu\right) c^\dagger_{k,\pm} c_{k,\pm} + H_{sc,\pm} \tag{2.57}$$

where the superconducting pairing term is given by Eq. 2.53 with spatial dependence

$$\begin{aligned} H_{sc,\pm} = \frac{1}{2} \sum_k \big[&\Theta(-y - w/2)\Delta_{1,\pm} \\ &+\Theta(y - w/2)\Delta_{2,\pm}\big]\, e^{-i\theta_k} c^\dagger_{k,\pm} c^\dagger_{-k,\pm} + h.c. \end{aligned} \tag{2.58}$$

where $\Delta_{i,\pm}$ is the effective pairing on side $i \in \{1, 2\}$ for the $\pm$ bands, as shown in Eq. 2.56,

$$\Delta_{i,\pm} = \Delta_0 \left(|\partial_z \varphi_\pm(z = 0)|^2 + |\partial_z \varphi_\pm(z = d)|^2\, e^{i\phi_i}\right) \tag{2.59}$$

where $\varphi_\pm$ is the z-dependent part of the wave function at $k_x = 0$ for the two Fermi surfaces.

As derived in Sec. 2.2.2, in the Andreev limit ($\mu \gg \Delta_{i,\pm}$), the ABS gap always closes when the phase difference across the junction becomes π. This corresponds to the condition

$$\frac{\epsilon_\pm + e^{i\phi_1}}{|\epsilon_\pm + e^{i\phi_1}|} = -\frac{\epsilon_\pm + e^{i\phi_2}}{|\epsilon_\pm + e^{i\phi_2}|}. \tag{2.60}$$

where $\epsilon_\pm$ is the relative proximitized pairing amplitude between the top and bottom surfaces for the outer $(+)$ or the inner $(-)$ fermi surfaces, $\epsilon_\pm = |\partial_z \varphi_\pm(z = 0)|^2 / |\partial_z \varphi_\pm(z = d)|^2$. Note that a

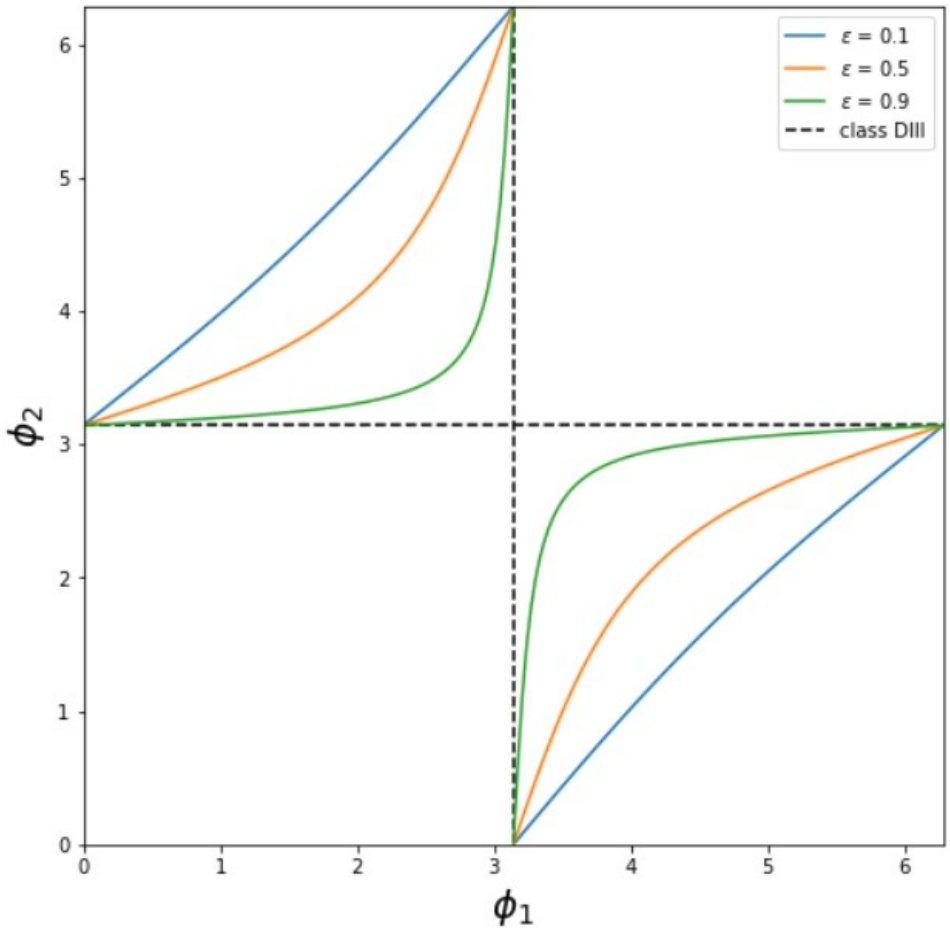

Figure 2.2: Gap-closing curves in the ϕ_1, ϕ_2 space for different ϵ. The dashed line corresponds to the helical Majorana states in the class DIII limit at $\phi_{1,2} = \pi$. As an example, assuming that $\epsilon_+ = 0.9$ and $\epsilon_- = 0.5$, the boomerang-shaped regimes between the orange and green curves in the second and the fourth quadrants are topological, while everything else is trivial.

necessary condition to satisfy Eq. 2.60 is $\epsilon < 1$.

The gap-closing curves in Eq. 2.60 for different $\epsilon < 1$ is shown in Fig. 2.2. Due to the combined effect of external electric field and the higher order p_z term in the Dresselhaus effect (Eq. 2.48), the values for $\epsilon_\pm$ are in general different for the two states $\pm$. Consequently, as shown in Fig. 2.2, there will be two regimes in the ϕ_1, ϕ_2 space enclosed by the two curves that correspond to $\epsilon_\pm < 1$. Across the boundaries, only one band inversion takes place and the fermion parity flips, resulting in a topological phase transition. Since the system is known to

be topologically trivial at phases $\phi_{1,2} = 0$, the two enclosed regimes correspond to topological superconductor phases. Finally, following similar arguments presented in Ref. [28], the topological phase will host a pair of MBSs at the two ends of the planar Josephson junction.

2.4.4 Gapless Majorana Edge Mode in the Class DIII Limit

Now we consider the case where ϵ is greater than 1 for one of the ABSs at $k_x = 0$, or $(\epsilon_+ - 1)(\epsilon_- - 1) < 0$. In this case, only one of the two fermi surfaces exhibits band inversion in the Andreev spectrum according to Eq. 2.60 and it seems that there is no enclosed regime in the topological phase diagram. In fact, the other topological phase boundaries can appear through a different mechanism. For $(\epsilon_+ - 1)(\epsilon_- - 1) < 0$, the 2DEG on the left or right sides of the junction becomes a class DIII topological superconductor [64, 65, 66, 67, 68] at the time-reversal symmetric point, $\phi = \pi$, with the topological number being the parity of Fermi surfaces that has negative pairing potential. In this case, helical Majorana edge states appear and the boundaries of the 2DEG are described by 1d Dirac equations. As a result, there will be gap closing at $\phi_1 = \pi$ and $\phi_2 = \pi$. This gives rise to the topological phase boundaries for fermi surfaces with $\epsilon > 1$ (See Fig. 2.2).

2.5 Simulation with HgTe

2.5.1 8-band Model near the Γ Point

Near the conduction band edge of HgTe at the Γ point, the Bloch wave functions are eigenstates of total angular momentum $j = 1/2$ or $j = 3/2$ due to spin-orbit interaction. Following Ref. [76], under the $k \cdot p$ frame work, we can assume the eigenstates to take the

form

$$\psi_{k_\parallel}(\vec{r}) = \sum_n F_n^{k_\parallel}(\vec{r}) u_n(\vec{r}) \tag{2.61}$$

where the envelope function $F_n^{k_\parallel}(\vec{r}) = \exp\left\{(i\vec{k}_\parallel \cdot \vec{r})\right\} f_n^{k_\parallel}(z)$ can be separated into a plane wave and a z dependent part and u_n are the eigenstates at Γ point where n indexes the basis states of $j = 1/2$ and $j = 3/2$ that are formed by the s and p orbitals. In the presence of an external electric field $\mathcal{E}$, the wave function in the z direction satisfies

$$\sum_n \left[H(k_\parallel)_{mn} + V(z)\delta_{m,n}\right] f_n^{k_\parallel}(z) = E f_m^{k_\parallel}(z) \tag{2.62}$$

where $H(k_\parallel)$ is an 8x8 matrix derived in Ref. [76] and $V(z) = e\mathcal{E}z$ is the linear potential from the electric field.

2.5.2 Effective p-wave Pairing for Different Bands

As mentioned in Sec. 2.4.2, the proximitized pairing potential is proportional to the tunneling amplitude across the interface. We can therefore assume the superconducting term in the HgTe to take the form

$$\Delta \sum_{j\in\{S,X,Y,Z\}} \int dxdy \partial_z \Psi_{j\uparrow}^\dagger(\vec{r})\Big|_{z=z_0} \partial_z \Psi_{j\downarrow}^\dagger(\vec{r})\Big|_{z=z_0} + h.c. \tag{2.63}$$

where S, X, Y, Z represent the four atomic orbitals for $l = 0$ and $l = 1$ at the valence band edge and z_0 is the z coordinate of the interface. In the eigenbasis of Eq. 2.62, the field operator can be

written as

$$\Psi^{\dagger}_{j\sigma}(\vec{r}) = \sum_{m,k_{\parallel}} c^{\dagger}_{k_{\parallel},m} e^{i\vec{k}_{\parallel}\cdot\vec{r}} \sum_{n} f_n^{(k_{\parallel},m)}(z) C^n_{j\sigma} \tag{2.64}$$

where m is the band index and $C^n_{j,\sigma}$ is the Clebsh-Gordon coefficient of state (j,σ) in state n. Plugging-in Eq. 2.64 into Eq. 2.63 gives the Cooper pairing between the eigenstates,

$$\begin{aligned} H_{sc} =& \Delta \sum_{k_{\parallel},m,m'} c^{\dagger}_{k_{\parallel},m} c^{\dagger}_{-k_{\parallel},m'} \\ & \times \left\{ \sum_{j\in\{S,X,Y,Z\}} \left[\sum_{n,n'} \partial_z f_n^{(k_{\parallel},m)}(z_0) \partial_z f_{n'}^{(-k_{\parallel},m')}(z_0) C^n_{j\uparrow} C^{n'}_{j\downarrow} \right] \right\} \end{aligned} \tag{2.65}$$

In the limit where the pairing potential is much smaller than the band splitting, we can neglect the off-diagonal terms in m, m'. Considering the contributions from the top and bottom superconductors, the pairing Hamiltonian is given by

$$H_{sc} = \sum_{m,k} \Delta_m(k) c^{\dagger}_{k,m} c^{\dagger}_{-k,m} + h.c. \tag{2.66}$$

where we have dropped the $\parallel$ subscript and will only work in 2D later on. The k-dependent pairing potential for m band, $\Delta_m(k)$, exhibits p-wave symmetry,

$$\Delta_m(k) = \Delta \left[\epsilon_{k,m}(0) + e^{i\phi} \epsilon_{k,m}(d) \right] \tag{2.67}$$

where the thickness is assumed to be d and the weight ϵ is given by

$$\epsilon_{k,m}(z) = \\ i\mathrm{Im}\left[\sum_{j\in\{S,X,Y,Z\}}\left(\sum_{n,n'}\partial_z f_n^{(k,m)}(z)\partial_z f_{n'}^{(-k,m)}(z)C_{j\uparrow}^n C_{j\downarrow}^{n'}\right)\right] \tag{2.68}$$

The imaginary part is taken as contributions from k and $-k$ are combined.

2.5.3 Topological Superconductivity in HgTe

For simulation, we pick parameters $d = 10$nm and gate voltage $Ed = 0.05$V and solve for the eigenstates $f_n^{(k,m)}(z)$ in Eq. 2.62. The other band structure parameters of the 8-band model are taken directly from Ref. [76].

Without external field, the 8-band Hamiltonian is doubly degenerate throughout the Brillouin zone due to the combined symmetry of time-reveral and spatial-inversion symmetries $\mathcal{PT}$. Upon applying an electric field together with the infinite-well potential in the z-direction, the degeneracy is lifted. The dispersion relation for the four Γ_8 bands along $k_x = 0$ is shown in Fig. 2.3. We next choose the chemical potential $\mu = 0.15$ eV to have a pair of inner $(-)$ and outer $(+)$ Fermi surfaces. By plugging the wave functions into Eq. 2.68, we get the strength $\epsilon_{k,\pm}$ of the proximity effect from the top and bottom Fermi surfaces. The resulting relative proximitized pairing amplitude $\epsilon_\pm$ is

$$\epsilon_- \approx 12.70$$

$$\epsilon_+ \approx 0.01773 \tag{2.69}$$

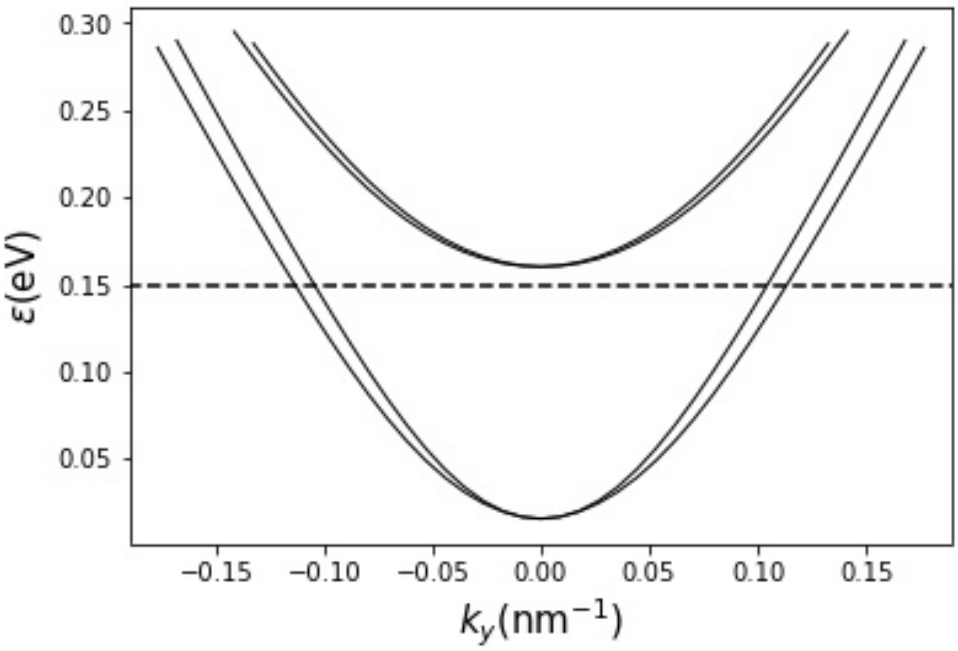

Figure 2.3: Dispersion relation along $k_x = 0$ of the Γ_8 bands of a slab of HgTe under external electric field. The thickness d is 10nm and the electric field $\mathcal{E}$ is set such that the electric potential difference across the slab $\mathcal{E}d = 0.05$V.

The $\epsilon_\pm$ satisfies $(\epsilon_+ - 1)(\epsilon_- - 1) < 0$. As discussed in Sec. 2.4.3, one side of the the topological regime is enclosed by the band inversion points in Andreev spectrum according to Eq. 2.60 and the other is from the class DIII mechanism which takes place at precisely $\phi_{1,2} = \pi$. The resulting phase diagram is shown in Fig. 2.4.

2.5.4 ABS Spectrum at Finite k_x

For the MBSs to be robust, the planar Josephson junction must be gapped throughout the Fermi surface. To verify this is true in our system, we simulate the Andreev spectrum at finite k_x. As an approximation, we will consider the dispersion of the two low energy bands in Fig 2.3 to be quadratic, or $\epsilon(\vec{k}) \approx (k_x^2 + k_y^2)/2m^*$. The Andreev spectrum can be obtained by matching the continuous boundary condition, as described in Sec. 2.2.1, with the effective chemical potential

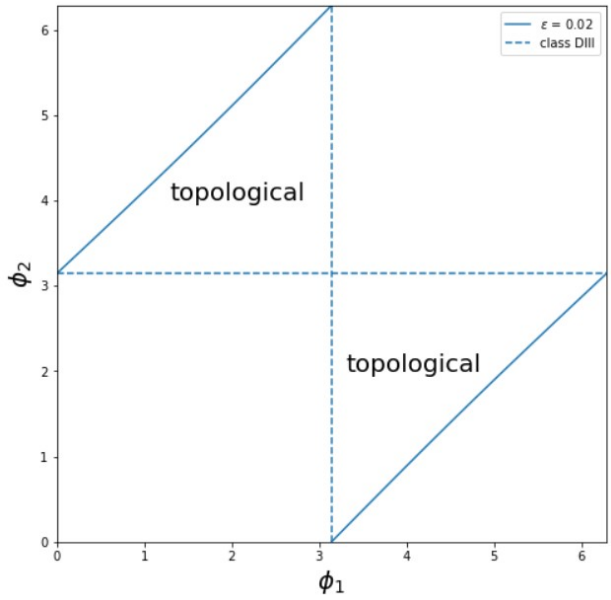

Figure 2.4: Topological phase diagram of HgTe with proximitized superconductivity under external electric field. The parameters are chosen to be $d = 10$nm and $Ed = 0.05$V. The solid line represents the phase boundary arising from Pientka's mechanism, and the dashed line represents that of the class DIII topological superconductor mechanism.

shifted to $\mu' = \mu - k_x^2/2m^*$. In Fig. 2.5, we show an example of the ABS energy gap along the Fermi surface. With chemical potential fixed to $\mu = 0.15$eV, we choose the pairing potential $\Delta_0 = 1$K, Josephson junction width $w = 100$nm. The phase differences for the two Fermi surfaces are set to be $\phi_{+(-)} = 0.01(3\pi/2)$ and the effective masses $m^*_{+(-)} = 0.0534(0.0469)m_e$ are obtained through fitting the curvatures at band minima in the dispersion shown in Fig. 2.3. Note that although there are visible discrepancies between the dispersion in Fig. 2.3 and the quadratic fit at k_y closer to k_F, the ABS gap in Fig. 2.5 at large k_x is expected to be accurate since we are effectively looking at the band minimum. On the other hand, at small k_x, the system is well approximated by the Andreev limit, where the gap does not depend on details of the dispersion of the energy band. This qualitatively justifies our approximation of the quadratic dispersion for the ABS gap calculation.

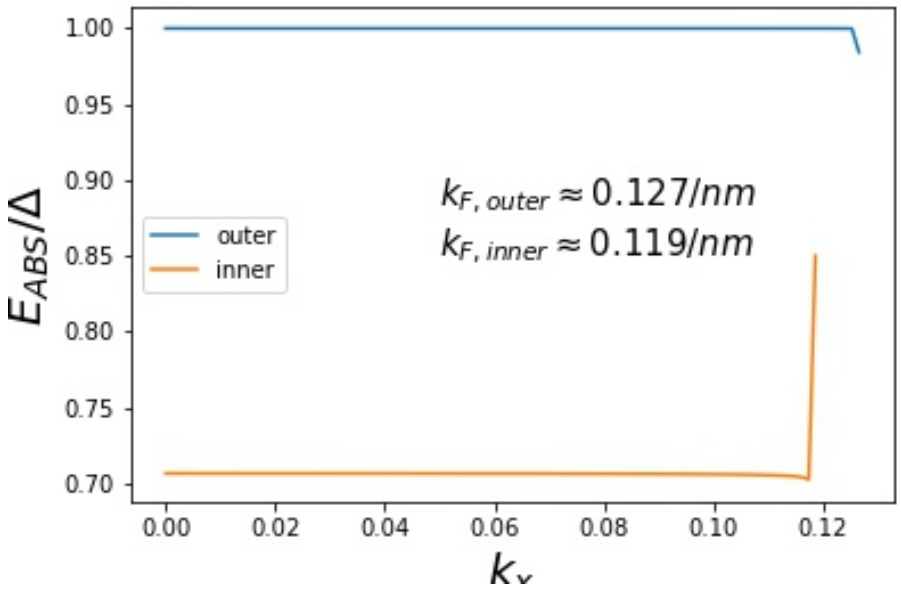

Figure 2.5: Energy gap of the Andreev spectrum as a function of k_x. The parameters are $\Delta_0 = 1\text{K}, m^*_{+(-)} = 0.0534(0.0469)m_e$, $\phi_{+(-)} = 0.01(3\pi/2)$ and Josephson junction width $d = 10\text{nm}$

2.6 Conclusion

In this work, we introduce a new type of planar Josephson junction that can host Majorana bound states. Our system is analogous to the Fu-Kane tri-junction model with the topological insulator replaced by a spin-orbit coupled 2DEG. The usual effect of magnetic field that splits the Andreev spectrum of the spin-orbit coupled bands is achieved by the three superconductor leads that controls the phase of the proximitized pairing potential.

The requirement for differentiating the effective pairing phase between the two Fermi surfaces is the coupling between k_z and $k_{\|}$, as presented explicitly in the higher order terms of the Dresselhaus interaction. This allows the electric field in the z-direction to change the wave function differently, resulting in distinct tunneling amplitude of Cooper pairs from the top and bottom surfaces.

In the more realistic model with HgTe, the electric field plays a slightly different role. Due to the combination of time-reversal and spatial inversion symmetry, the system exhibits two-fold degeneracy for all the Γ bands. Therefore, the breaking of the z-inversion symmetry by the electric field lifts this degeneracy. The fact that the two Fermi surfaces originate from a degenerate space allows the state to have highly imbalanced proximity effect from the top and bottom superconductors, as presented in Eq. 2.69. Otherwise, the unperturbed states are expected to by symmetric in the z-direction and a much stronger electric field will be needed. To realize the Majorana zero mode experimentally, the phase differences between the three superconductors can be controlled by external currents in the z direction across the two-dimensional Josephson junction on the two sides. The width w of the planar Josephson junction is required to be less than the coherent length of the superconductors to enable effective tunneling. Finally, in the topological regime, the existence of the Majorana zero mode can be verified through the zero-bias peak in the tunneling conductance.

Chapter 3: Coherent Phase Mode in the Insulating Josephson Junction Chain

3.1 Introduction

The quantum dynamics of many-body systems has been at the crux of recent conceptual developments such as the phenomena of many-body localization [77] and AdS-CFT correspondence [78]. This recent interest represents an attempt to extend our knowledge beyond the understanding of static quantum phenomena in terms of quantum field theory using the renormalization group [79]. It is becoming clearer that such traditional approaches, such as analytic continuation of imaginary time correlators [79], are insufficient to discuss quantum dynamical phenomena, which are becoming more accessible in experiments. One test-bed for understanding such dynamical quantum phenomena is the study of conductance at the superconductor-insulator critical point. Despite the static appearance of dc conductance, it is technically defined as a limit of vanishingly small frequency. The theory in two dimensions leads to a prediction of interesting consequences of the particle-vortex duality such as universal conductance [80] that are borne out by experiments [81, 82, 83]. Microwave measurements of the ac conductivity have revealed intriguing signatures of residual superfluid stiffness even in the insulating phase [84]. The superfluid-insulator transition in the Bose-Hubbard model [79, 85] also turned out to be quite interesting in the context of ultra-cold atoms where an under-damped Higgs mode [86] was observed [87].

A conceptually simpler context where the superfluid-insulator transition (SIT) was predicted

to occur [88] is that of one dimensional chains of Josephson junctions (JJ's). As we will derive in Sec. 3.2.1, in the vicinity of the SIT quantum critical point, such a system is described by the sine-Gordon Hamiltonian [89] (rescaled to fit the convention for SIT [90]) of the form

$$H = \int dx \frac{v_c}{2}[K\pi j^2 + (K\pi)^{-1}\partial_x\theta^2] + \frac{g}{2}\cos 2\theta, \tag{3.1}$$

where $\partial_x\theta \propto \rho(x)$, which is the density of Cooper pairs in the system and j is the current density operator that is canonically conjugate to θ and v_c is the speed of the superfluid phase oscillations (also equivalently the charge velocity). Since the microscopic origin of the charging energy K is from a combination of junction and ground capacitance, as detailed in Sec. 3.2.1, the microscopic Hamiltonian of the JJ chain can be quantitatively mapped to the sine-Gordon Hamiltonian Eq. 3.1 over a large parameter range. Note that at $g = 0$, the superconducting phase variable (defined as $\phi \propto \int dx j(x)$) is algebraically ordered allowing us to define superfluid phase oscillations. Such oscillations may also be thought of as plasma oscillations of the charge density $\rho(x)$ accompanied by coherent oscillation of the current density $j(x)$. The parameter g in Eq. 3.1 is related to the amplitude of phase slips in the chain that would manifest as decay of supercurrent [91, 92] and K is the Luttinger parameter, which manifests as the inverse of impedance of the chain and determines the transport of the chain at weak values of g. Specifically, the Hamiltonian H would describe a near-critical insulating phase for the clean JJ chain at long wave-lengths for $K < 2$ (or $3/2$ in the disordered case) [89, 90]. This transition was observed in SQUID arrays, where the effective Josephson coupling, which controls K and g, are tuned across the transition [93].

While the dc transport properties of the superconductor-insulator transition in JJ chains had been studied previously [93], the dynamical properties have only recently begun to be explored [1,

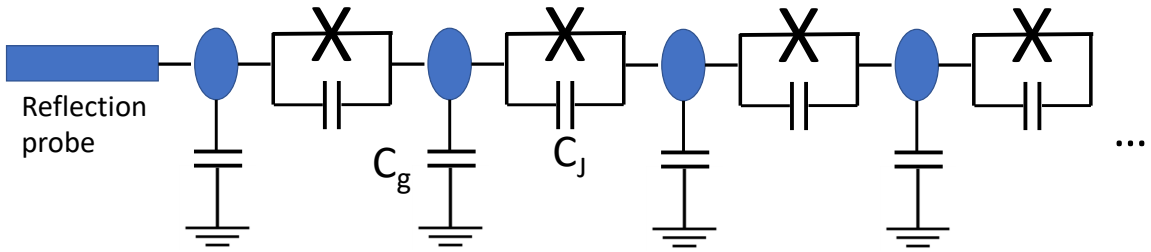

Figure 3.1: Absorption of a weakly coupled transmission probe on the left measures the dynamical conductivity $\sigma_R(\omega) = \omega\chi(\omega)$ at the end of a JJ chain. The JJ chain is composed of an array of islands with ground capacitance C_g coupled by JJ's. The JJ's have a capacitance C_J in addition to a Josephson coupling with strength E_J.

94]. One such study, which considered the microwave response (schematic shown in Fig. 3.1) of such JJ chains [1], have revealed coherent oscillations associated with superfluid phasecoherence deep in the insulating phase of such JJ chains, where the superfluid phase has been predicted to be disordered analogous to the two-dimensional XY model [88]. In contrast to microwave measurements of two dimensional films [84], these measurements [1] suggest phase coherence across the entire length of the JJ chain as opposed to puddles. The coherent oscillations in the JJ chain [1] are measured by a reflection probe in Fig. 3.1 that applies an ac electric field with frequency ω to the end island. The measured absorption can be related to the imaginary part of the ac polarizability of the system $\chi(\omega)$ at the end of the JJ chain. Here we are ignoring possible power law prefactors of ω that arise from coupling efficiency of χ to the transmission line. Sharp peaks in $\chi(\omega)$ represent resonant excitation of a collective mode in the wire. The recent measurement of the ac conductivity [1] observes a discrete frequency comb of such peaks that suggests excitation of a collective mode associated with phase coherence across the insulating chain. However, the peaks in the comb appear to broaden out and disappear as one goes to lower frequencies consistent with there being no dc conductance in the insulator.

In this work we calculate the ac polarizability $\chi(\omega)$ of an ideal sine-Gordon insulator described by Eq. 3.1 near the Luther-Emery point (i.e. $K \simeq 1$) [95] at vanishingly small temperatures. We find that in this limit, the ac polarizability shows sharp oscillations associated with the creation of soliton-antisoliton pairs. Additionally, we use numerical calculations for $K = 1$, where the model can be mapped to free-fermions, to include disorder to show that our conclusions apply qualitatively to the disordered case. Finally, we compare the results obtained with the perturbative decay rate of high frequency phase modes in the microscopic charge disordered JJ chain model. The decay of the single-plasmon state is studied by an application of Fermi's golden rule to quantum phase slips. This study allows us to put the theoretical results in the context of expectations from experimentally realistic superconducting JJ chain that has substantial charge disorder as well as a non-linear plasmon dispersion.

3.1.1 Superconductor-Insulator Transition in Josephson Junction Chains

One of the most important properties of a Josephson junction chain is the quantum phase transition between superconducting and insulating phase. The property of a Josephson junction chain is governed by three energy scales, which are the Josephson energy E_J, the charge coupling energy between the superconductor islands $E_1 = 2e^2/C_J$, and that between an island and the ground plane $E_0 = 2e^2/C_g$. In the simplified regime where the ground capacitance C_g dominates over the island-island capacitance C_J, E_1 becomes irrelevant and the quantum transport property is determined by the ratio E_J/E_0. At $E_J/E_0 \gg 1$, the Josephson junction chain is in the superconducting regime, where the chain remains phase coherent and is able to carry supercurrent. On the other hand, at $E_J/E_0 \ll 1$, the chain enters an insulating regime or the Coulomb blockade

regime, which is exhibits the opposite behavior of superconductivity: zero current in the presence of a finite voltage difference. This superconductor-insulator transition was observed [96, 97, 98, 99, 100] in arrays of SQUIDs, which act as tunable Josephson junctions with the effective Josephson energy $E_J = E_J^0 |\cos \pi\Phi/\Phi_0|$, where Φ is the magnetic flux through the SQUID loop.

This phenomenon was first predicted by Bradley and Doniach [88], who show the connection of the quantum phase transition to to the renowned Kosterlitz-Thouless (KT) transition in a classical 2D XY model [101]. In the self-charging limit, $C_g \gg C_J$, the chain is described by the Hamiltonian

$$H = \sum_i \left(E_0 \, p_i^2 - 2E_J \cos(\phi_{i+1} - \phi_i) \right) \tag{3.2}$$

where ϕ_i represents the phase of the i^{th} island and $p_i = -i\partial/\partial\phi_i$ is the conjugate momentum representing the number of Cooper pairs on the i^{th} island. The quantum partition function of the system $Z \equiv \text{Tr}\, e^{-\beta H}$ can be expanded in the ϕ basis.

$$Z = \int \prod_i d\phi_i \langle \phi_1, ..., \phi_{N_x}| \, e^{-\beta H} \, |\phi_1, ..., \phi_{N_x}\rangle \tag{3.3}$$

In the regime where $T \ll E_0, E_J \ll \Delta$, with Δ being the superconducting gap, the partition function integral can be decomposed into imaginary time evolution of interval Δ^{-1}. That is, $e^{-\beta H} = \left(e^{-\Delta^{-1} H}\right)^{N_\tau}$ where $N_\tau \equiv \Delta\beta \gg 1$. Following the standard procedure of the path integral formalism, we can insert complete basis of ϕ's at each divisions. This turns the partition function (Eq. 3.3) into an integral over the two dimensional grid of ϕ's.

$$Z = \int \prod_{i,j} d\phi_{i,j} \langle \vec{\phi}_1 | e^{-\Delta^{-1} H} | \vec{\phi}_2 \rangle \langle \vec{\phi}_2 | e^{-\Delta^{-1} H} | \vec{\phi}_3 \rangle ... \langle \vec{\phi}_{N_\tau} | e^{-\Delta^{-1} H} | \vec{\phi}_1 \rangle \tag{3.4}$$

where $|\vec{\phi}_j\rangle \equiv |\phi_{1,j}, \phi_{2,j}, ..., \phi_{N_x,j}\rangle$. Using the Baker-Campbell-Hausdorff identity and discarding the second order terms in $E_{0,J}/\Delta$, the matrix element is given by

$$\langle\vec{\phi}_j|e^{-\Delta^{-1}H}|\vec{\phi}_{j+1}\rangle \approx \langle\vec{\phi}_j|\exp\left\{\left(-\frac{E_0}{\Delta}\sum_i p_i^2\right)\right\}|\vec{\phi}_{j+1}\rangle \exp\left\{\left[\frac{2E_J}{\Delta}\sum_i \cos(\phi_{i+1,j}-\phi_{i,j})\right]\right\} \tag{3.5}$$

The momentum term can be expanded through inserting the complete basis of momentum eigenstates,

$$\begin{aligned}\langle\vec{\phi}_j|\exp\left\{\left(-\frac{E_0}{\Delta}\sum_i p_i^2\right)\right\}|\vec{\phi}_{j+1}\rangle &= \langle\vec{\phi}_j|\left(\sum_{\vec{m}}|\vec{m}\rangle\langle\vec{m}|\right)\exp\left\{\left(-\frac{E_0}{\Delta}\sum_i p_i^2\right)\right\}|\vec{\phi}_{j+1}\rangle \\ &= \frac{1}{2\pi}\sum_{\vec{m}}\exp\left\{\left[i\vec{m}\cdot\left(\vec{\phi}_j-\vec{\phi}_{j+1}\right)-\frac{E_0}{\Delta}m^2\right]\right\}\end{aligned} \tag{3.6}$$

where $|\vec{m}\rangle$ represents the basis states with fixed Cooper pair numbers. Using the Villain approximation, which states that $e^{\beta\cos\theta} \approx e^{\beta}\sum_{n=-\infty}^{\infty} e^{-\frac{1}{2}\beta(\theta-2\pi n)^2}$ in the limit $\beta \gg 1$, the summation in Eq. 3.6 can be approximated as

$$\langle\vec{\phi}_j|\exp\left\{\left(-\frac{E_0}{\Delta}\sum_i p_i^2\right)\right\}|\vec{\phi}_{j+1}\rangle \approx \exp\left[\frac{\Delta}{2E_0}\sum_i \cos(\phi_{i,j+1}-\phi_{i,j})\right]. \tag{3.7}$$

As a result, the partition function Z can be approximated as

$$Z \approx \int\prod_{i,j} d\phi_{i,j}\exp\left\{\left[\sum_{i,j}\frac{2E_J}{\Delta}\cos(\phi_{i+1,j}-\phi_{i,j})+\frac{\Delta}{2E_0}\cos(\phi_{i,j+1}-\phi_{i,j})\right]\right\}. \tag{3.8}$$

This is precisely the partition function of an anisotropic 2d XY model where the coupling in the τ direction is much stronger than that of the x direction. Through rescaling the lattice size in the τ direction ($d\tau \to d\tau\sqrt{E_J E_0}$), it can be shown that the critical behavior of this model is equivalent

to the isotropic XY model with $\beta J = -\sqrt{E_J/E_0}$

$$Z_{XY} = \int \prod_{\vec{r}} d\phi_{\vec{r}} \exp\left\{ \left[\sqrt{\frac{E_J}{E_0}} \sum_{\langle \vec{r},\vec{r}' \rangle} \cos(\phi_{\vec{r}} - \phi_{\vec{r}'}) \right] \right\} \tag{3.9}$$

where $\vec{r}$ labels the two-dimensional position. Due to the Mermin-Wagner theorem [102], the two dimensional XY model is prohibited to spontaneously develop a long-range order. That is, $\langle \phi \rangle = 0$. However, the system is known to undergo a Kosterlitz-Thouless type transition from the regular disorder phase at high temperature, where the order-parameter-order-parameter correlation function decays exponentially with distance, to the quasi-long-range ordered phase at low temperature, where the correlation function becomes algebraically decaying [101, 103]. Accordingly, at low $\sqrt{E_J/E_0} > K_C \sim 0.81$, it can be shown [88] that the quasi-long-range ordered phase exhibits a delta-function peak at dc-conductivity $\sigma(\omega) \sim \delta(\omega)$ representing a superconducting phase. On the other hand, in the disorder phase $\sqrt{E_J/E_0} \ll 1$, the conductivity has a characteristic frequency corresponding to the charging energy $\sigma(\omega) \sim \delta(\omega - 2E_0)$ [104] and there is no dc-conductivity. Consequently, the Kosterlitz-Thouless transition manifests as a superconductor-insulator transition within the clean Josephson junction chain, which is controlled by the parameter E_J/E_0.

3.1.2 Pinning of Charge Density Wave under Disorder

For a fermionic system in one dimension, the low energy physics is captured by the Luttinger model. In the non-interacting limit, the density-density correlation has a characteristic wavelength determined by the Fermi momentum, $2k_F$ that exhibits a power-law decay given by $\langle \rho_{2k_F}(x)\rho_{-2k_F}(0) \rangle \sim x^{-2}$. Due to the fact that the Fermi surface in one-dimension is at two discrete momenta ($\pm k_F$),

the effect of interaction is determined by the two scattering processes for spinless fermions. The g_4 process couples fermions on the same side of the Fermi surface and the g_2 process represents the forward scattering of fermions on the opposite sides of the fermi surface, with the Hamiltonian density

$$\mathcal{H}_{int}(x) = g_4 \left(\rho_R^2(x) + \rho_L^2(x)\right) + 2g_2\rho_R(x)\rho_L(x) \tag{3.10}$$

where L and R labels the left and right moving branch, respectively. With interaction, the correlation becomes a non-universal power-law function

$$\langle \rho_{2k_F}(x)\rho_{-2k_F}(0)\rangle \sim x^{-2K}, \tag{3.11}$$

where K is the Luttinger parameter given by,

$$K = \left(\frac{1 + y_4/2 - y_2/2}{1 + y_4/2 + y_2/2}\right)^{1/2} \tag{3.12}$$

where $y \equiv g/(\pi v_F)$. The correlation function obeys the Mermin-Wagner theorem, which states that local interactions can not create a long range order in one dimensional systems. However, the power-law behavior suggests that the system is on the verge of instability towards developing a charge density wave (CDW), which is a state with periodic modulation of charges, with momentum $2k_F$. This instability appears as singularities in the CDW susceptibility $\chi_{\text{CDW}}(k, \omega)$, which can be obtained from the fluctuation-dissipation theorem in imaginary time, whose real time version will be discussed in Sec. 4.2.3.

$$\chi_{\text{CDW}}(k, i\omega_n) = \int_0^\beta d\tau \int dx \langle \rho(x,\tau)\rho(0,0)\rangle e^{-ikx + i\omega_n\tau} \tag{3.13}$$

and the dynamical susceptibility $\chi_{\text{CDW}}(k,\omega)$ can be obtained through analytic continuation $i\omega_n \to \omega + i\delta$. Utilizing the Lorentz invariance of the action, and the power-law correlation function at $2k_F$ Eq. 3.10, it can be argued through scaling analysis that at $\beta \to \infty$, the susceptibility scales as

$$\chi_{\text{CDW}}(k,\omega) \sim max\left[\left|k-2k_F\right|,\omega\right]^{2K-2} \tag{3.14}$$

Therefore, at the repulsive regime $K < 1$ (or $g_2 > 0$), the one-dimensional system has a divergent fluctuation for charge density wave at $k = 2k_F$.

Next, we consider a disorder potential in the Hamiltonian

$$\mathcal{H}_{\text{dis}} = V(x)\rho(x) \tag{3.15}$$

where the disorder potential $V(x) = \sum_i f(x - R_i)$ is the sum of contribution from different impurity sites. For high impurity density n_i with weak individual contribution f, $V(x)$ can be assumed to be a smooth potential described by the Gaussian distribution with correlation function

$$EV(x)V(x') = D(x - x'). \tag{3.16}$$

Assuming the impurity potentials f are short in range compared to k_F^{-1}, the correlation function can be approximated with the delta function form $D(x - x') \approx D\delta(x - x')$. In the low energy physics, the effect of V can be decomposed into two components, the forward scattering η and

the backward scattering ξ,

$$\mathcal{H}_{\text{dis}}(x) = \eta(x)\left(\psi_R^\dagger(x)\psi_R(x) + \psi_L^\dagger(x)\psi_L(x)\right) + \xi(x)\psi_R^\dagger(x)\psi_L(x) + \xi^*(x)\psi_L^\dagger(x)\psi_R(x) \tag{3.17}$$

where η is associated with a momentum transfer of $q \approx 0$ and ξ is associated with $q \approx \pm 2k_F$. Therefore, the two potentials are uncorrelated, that is,

$$\begin{aligned} E\eta(x)\eta(x') &= D_f\delta(x-x') \\ E\xi(x)\xi^*(x') &= D_b\delta(x-x') \\ E\eta(x)\xi(x') &= 0 \end{aligned} \tag{3.18}$$

where $D_f = D_b = D$ according to our approximation. Next, we will use the bosonization representation whose recipe for spinless fermion is given by [89],

$$\psi_r(x) = \frac{U_r}{\sqrt{2\pi\alpha}} e^{irk_F} e^{-i(r\phi(x)-\theta(x))}, \tag{3.19}$$

where α is a regularization parameter that represents a finite band width of the system, U_r is a so-called Klein factor that annihilates a fermion of species $r = \pm$ which corresponds to the right $(+)$ and the left $(-)$ moving electrons, respectively. ϕ and θ are fields that satisfies the commutation relation $[\phi(x_1), \theta(x_2)] = i\frac{\pi}{2}\text{Sign}(x_2 - x_1)$ and are related to the density operators of different

species by

$$\partial_x \phi = -\pi[\rho_R(x) + \rho_L(x)]$$
$$\partial_x \theta = \pi[\rho_R(x) - \rho_L(x)] \tag{3.20}$$

Using Eq. 3.19 and Eq. 3.20, we can rewrite Eq. 3.17 as

$$\mathcal{H}_{\text{dis}}(x) = -\frac{1}{\pi}\eta(x)\partial_x\phi + \frac{1}{2\pi\alpha}[\xi(x)e^{2ik_F+2i\phi(x)} + h.c.]. \tag{3.21}$$

In terms of the field operators, the clean Hamiltonian density is given by

$$\mathcal{H}_0(x) = \frac{u}{2}\left[\pi K(\Pi(x))^2 + \frac{1}{\pi K}(\partial_x\phi(x))^2\right], \tag{3.22}$$

where $\Pi \equiv \partial_x\theta/\pi$. Combining the two, first, we can see that the forward scattering (η) term that is linear in $\partial_x\phi$ can be absorbed into $\mathcal{H}_0$ by transforming

$$\tilde{\phi}(x) = \phi(x) - \frac{K}{u}\int_{-\infty}^{x} dx'\eta(x') \tag{3.23}$$

which results in

$$\mathcal{H}(x) = \mathcal{H}_0[\Pi(x), \tilde{\phi}(x)] - \frac{K}{2\pi u}\eta^2(x) + \left[\frac{\xi(x)e^{2ik_F - \frac{K}{u}\int^x dx'\eta(x')}}{2\pi\alpha}e^{2i\tilde{\phi}(x)} + h.c.\right] \tag{3.24}$$

due to the random nature of $\xi(x)$, adding the phase factor $e^{2ik_F - \frac{K}{u}\int^x dx'\eta(x')}$ does not change its distribution. That is, let $\tilde{\xi}(x) = \xi(x)e^{2ik_F - \frac{K}{u}\int^x dx'\eta(x')}$, the correlation function is given by

$E\tilde{\xi}(x)\tilde{\xi}^*(x') = D_b\delta(x-x')$. Accordingly, the ground state property of the system is determined by the effective Hamiltonian

$$\mathcal{H}(x) = \frac{u}{2}\left[\pi K(\Pi(x))^2 + \frac{1}{\pi K}(\partial_x\phi(x))^2\right] + \left[\frac{\xi(x)}{2\pi\alpha}e^{2i\phi(x)} + h.c.\right], \tag{3.25}$$

where we have dropped the scalar term and the tilde notations. Under electron-electron interaction $K \neq 1$, Eq. 3.25 describes a competition between the quantum fluctuation given by the conjugate field, and a tendency towards pinned charge density wave by the disorder potential. In the classical limit ($K, \hbar \to 0$ and $K/\hbar = const.$) and neglecting the kinetic term that is proportional to $(\partial_x\phi(x))^2$, it is energetically desirable for the field ϕ to follow the disorder potential ξ such that $\exp\{2i\phi + i\arg(\xi)\} = -1$. Note that the classical limit corresponds to an extremely strong repulsive interaction between electrons. This scenario can be understood as the charge density wave being pinged by the disorder potential to the impurity sites. Putting back the kinetic term, the sharp variation in ϕ will now be suppressed. The localization length Λ_{loc} can be estimated by the length scale at which the ϕ field is roughly constant. This would create an energy cost from the disorder potential of $E_{\text{dis}} \sim \sqrt{D_b\Lambda_{\text{loc}}}$ where the square-root scaling with Λ_{loc} comes from the uncorrelated assumption in Eq. 3.18 between ξ at different locations. On the other hand, the cost in kinetic energy is inversely proportional to the localization length $E_{\text{k}} \sim 1/\Lambda_{\text{loc}}$, as it represents the frequency of changes in the ϕ field. Through minimizing $E_{\text{k}} + E_{\text{dis}}$, we can estimate that the localization has a simple power-law relation with the strength of the back-scattering potential

$$\Lambda_{\text{loc}} \propto \left(\frac{1}{D_b}\right)^{1/3} \tag{3.26}$$

This argument and results is analogous of the Larkin length [105]of vortex pinning in superconductors and it is called the Fukuyama-Lee length [106] in the context of the CDW.

Away from the classical limit, the precise treatment of quantum fluctuations in the Π and ϕ fields are done by Giamarchi and Shultz [107] through the renormalization group (RG) technique. The RG equation was derived by considering the disorder as a perturbation on top of the Luttinger liquid. For the spinless fermion, the RG flow in the weak disorder limit $D_b \to 0$ is given by

$$\frac{dD_b}{dl} = (3 - 2K)D_b \tag{3.27}$$

This suggests a critical Luttinger parameter $K^* = 3/2$ in the weak disorder limit. For $K > K^*$, which is deep in the attractive regime, the disorder strength flows to 0 as length scale increases, corresponding to a delocalized state. On the other hand, for $K < K^*$, it flows to a localized state where the disorder dominates and the charge density wave are pinned by its potential.

While the above theories are originally formulated for one-dimensional spinless fermions, their implications extend broadly to one-dimensional bosonic systems. This is usually due to the formal equivalence between the field representation in Eq. 3.22 and the Hamiltonian of bosonic systems. The connection from the Josephson junction chain with weak charge disorder and the charge density wave pinning physics was discussed by Houzet and Glazman. [108]. The microscopic Hamiltonian of a Josephson junction chain is given by

$$H = \frac{1}{2}\sum_{nm} Q_n C^{-1}_{nm} Q_m - E_J \sum_n \cos(\phi_n - \phi_{n+1}) \tag{3.28}$$

where the charge and the phase satisfies the commutation relation $[\phi_n, Q_m] = 2ie\delta_{n,m}$ and C_{nm}

is the capacitance between islands n and m. Considering up to the nearest neighbor couplings, C is parametrized by the capacitance between the Josephson junctions C_J and that to the ground plane C_g. In the large E_J limit, the Hamiltonian in Eq. 3.28 can be approximated by its expansion to the quadratic term in $\phi_n - \phi_{n+1}$, yielding the dispersion relation

$$\omega(q) = \frac{v|q|}{\sqrt{1 + (vq/\Omega)^2}} \tag{3.29}$$

where the plasmon velocity is given by $v = a\sqrt{E_0 E_J}/\hbar$ and $\Omega = \sqrt{E_1 E_J}/\hbar$ is the plasma frequency across a single Josephson junction. The long-wavelength plasma modes that has a linear dispersion $\omega \approx v|q|$ can be modeled by the Hamiltonian that takes the exact same form as Eq. 3.22,

$$H_0 = \int \frac{v}{2}\left[\pi K(\Pi(x))^2 + \frac{1}{\pi K}(\partial_x \varphi(x))^2\right] dx, \tag{3.30}$$

where the field $\Pi = -\partial_x \phi/\pi$ is the gradient of the coarse-grained phase field and φ is the canonical conjugate of Π, satisfying $[\varphi(x), \Pi(x')] = i\hbar\delta(x - x')$. Accordingly, φ is related to the Cooper pair density by $\rho = -\partial_x \varphi/\pi$. The Luttinger parameter $K = \pi\sqrt{E_J/2E_0}$ has a simple relation with the low-frequency impedance of the Josephson junction chain Z by $K = \pi\hbar/(4e^2 Z)$. The most important correction to this linearized Hamiltonian is the phase slip effect, where the phase difference $\phi_{i+1} - \phi_i$ across a junction jumps by 2π. This process is generated by the operator $e^{2i\varphi(x)}$ that generates a 2π kink in the phase field ϕ at position x. The main source of disorder is the random stray charges ρ_x in the chain that couples to the Cooper pairs through Coulomb interaction. It appears in the Hamiltonian as an Aharaonov-Casher phase $\chi(x)$ in the

phase slip process, That is,

$$H_{QPS} = -\frac{\lambda}{a}\int dx \cos(2\varphi(x) + \chi(x)), \tag{3.31}$$

where $\chi(x) = 2\pi\int^x dx'\rho_b(x')$ and in the limit $E_J \gg E_1$, the phase slip amplitude λ is given by [108, 109]

$$\lambda = \frac{8}{\sqrt{\pi}}(2E_J^3E_1)^{1/4}e^{-\sqrt{32E_J/E_1}}. \tag{3.32}$$

The phase slip Hamiltonian with random Aharaonov-Casher phases acts as a pinning potential for the φ field, which is analogous to the random potential pinning the charge density wave for the fermionic systems mentioned above. The RG flow for the full Hamiltonian $H = H_0 + H_{QPS}$ in the perturbative regime follows the same scaling as Eq. 3.27,

$$\frac{dD(\Lambda)}{dl} \simeq (3 - 2K)D(\Lambda) \tag{3.33}$$

where $D(\Lambda)$ represents the phase slip probability at the momentum cutoff Λ. Therefore, under the charge disorder, the Josephson junction chain exhibits a similar transition from the Bose glass to the superfluid phase from $K < 3/2$ to $K > 3/2$.

3.2 Model

3.2.1 Formal sine-Gordon Representation of Phase Slips

We start with the microscopic Hamiltonian of the JJ, which is given by

$$H = \sum_{i,j}(N_i - Q_i)U_{ij}(N_j - Q_j) + E_J \sum_i (1 - \cos \Delta\phi_i) \tag{3.34}$$

where N_i is number of Cooper pairs on site i, with strayed charge Q_i that represents disorder, E_J is the Josephson energy of the junctions, and $\Delta\phi_i = \phi_i - \phi_{i-1}$ is phase difference between site i and $i-1$. U_{ij} is the charging energy between i and j. Starting with the canonical commutation relations for charge and phase

$$[\phi_m, N_n] = i\delta_{mn} \tag{3.35}$$

one can define a new variable

$$\theta_n = \sum_m K(n-m)N_m$$

$$K(n) = \pi \tanh \alpha(n - 1/2). \tag{3.36}$$

The new variable θ satisfies the commutation relation

$$[\phi_m, \theta_n] = iK(n-m). \tag{3.37}$$

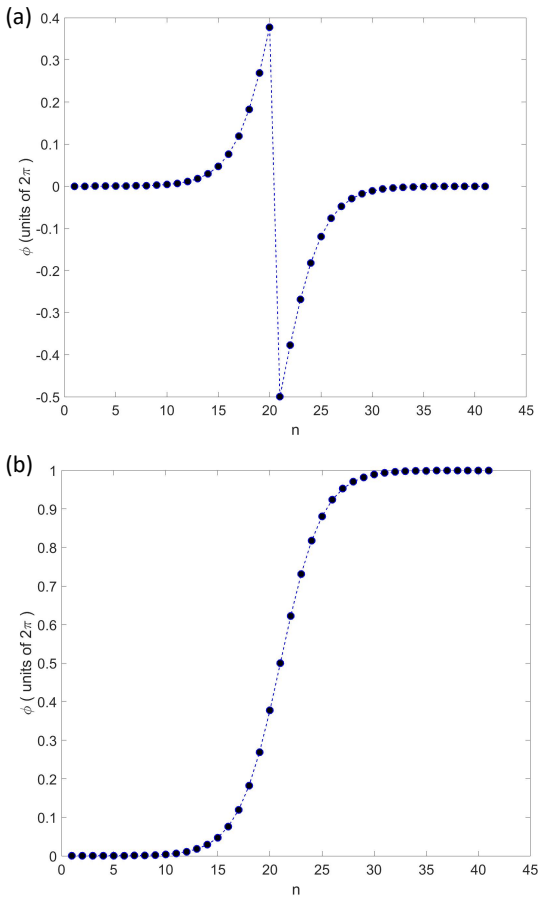

Figure 3.2: (a) Phase profile ϕ_n for the microscopic JJ chain model. The phase-slip phase profile is discontinuous but local in the sense that it vanishes away from the phase slip. (b) The discontinuity can be removed at the expense of introducing non-locality to produce an unwound phase-slip.

Using the Campbell-Baker-Hausdorf relation,

$$e^{-2i\theta_n}\phi_m e^{2i\theta_n} = \phi_m - 2K(n-m), \tag{3.38}$$

one can show that $e^{i\theta_n}$ creates a phase-slip with the profile shown in Fig. 3.2. Thus, the phase slip is generated by the sine term of the sine-Gordon model

$$H_{sine} = g\sum_i \cos 2\theta_i. \tag{3.39}$$

In order to properly include the variable θ, we need to transform to dual variables, which are defined by the momentum

$$\Pi_m = (\phi_{m+1} - \phi_m)/\pi, \tag{3.40}$$

which is canonicallly conjugate to θ_n as

$$[\theta_n, \Pi_m] = i\{K(n+1-m) - K(n-m)\} \approx i\delta_{nm}. \tag{3.41}$$

at length scale much larger than the width of the profile. In such limit, the JJ chain Hamiltonian, in terms of Π and θ, becomes

$$H = \sum_{i,j}\left(\frac{\theta_i - \theta_{i-1}}{\pi} - Q_i\right)U_{ij}\left(\frac{\theta_j - \theta_{j-1}}{\pi} - Q_j\right) + E_J\sum_i(1-\cos\pi\Pi_i) \tag{3.42}$$

In the regime that E_J dominates the charging energies U_{ij}, the Hamiltonian can be approximated

by expanding the Josephson energy to the quadratic term and include H_{sine} that represents the phase slip process. This changes the Hamiltonian to

$$H = \sum_{i,j} \left(\frac{\theta_i - \theta_{i-1}}{\pi} - Q_i \right) U_{ij} \left(\frac{\theta_j - \theta_{j-1}}{\pi} - Q_j \right) + \frac{E_J}{2} \sum_i (\pi \Pi_i)^2 + g \sum_i \cos 2\theta_i. \quad (3.43)$$

In the case that the ground capacitance is much greater than the junction capacitance, we can assume $U_{ij} = 4E_0\delta_{ij}$. Finally, we make a transformation $\theta_i \to \theta_i + \sum_{j \le i} Q_j$ and take the continuum limit. This yields the Hamiltonian that takes the sine-Gordan form

$$H = \int dx \, \frac{\pi^2 E_J}{2} \left(j(x)\right)^2 + \frac{4E_0}{\pi^2} \left(\partial_x \theta(x)\right)^2 + g \cos\left(2\theta(x) + \xi(x)\right) \quad (3.44)$$

where $\xi \equiv \int_{x'<x} dx' Q(x')$ and we substituted the notation $j \equiv \Pi$ to match that in Eq. 3.1.

3.2.2 Phase Slips from the Microscopic Model

In this section, we would like to make mathematical correspondence between a microscopic JJ chain model and sine-Gordon model through comparing the partition function of the two, which will be done by explicit derivation. The imaginary time action of the Hamiltonian in Eq. 3.42 is given by

$$S[\phi] = \int \frac{1}{4} \sum_{i,j} \dot{\phi}_i C_{i,j} \dot{\phi}_j + E_J \sum_i (1 - \cos \Delta\phi_i) d\tau, \quad (3.45)$$

where $C \equiv U^{-1}$ is the capacitance matrix. The partition function Z in path integral form is

$$Z_{JJC} = \oint \mathcal{D}[\phi] e^{-S[\phi]} \tag{3.46}$$

where the integration limit of S is from 0 to β. Due to the 2π periodicity in ϕ, the configurations can have B.C's with $2\pi n$ jumps in $\phi_{N+1} - \phi_1$ and $\int d\tau \partial_\tau \phi_i$. This is equivalent to including particular kinds of branch cuts into the configurations and restoring periodic boundary conditions on both time and position.

The branch cuts transforms $(\partial_\tau, \Delta) \rightarrow (\partial_\tau - a_0, \Delta - a_1)$ with a vector potential $\mathbf{a} = (a_0, a_1)$,

$$Z_{JJC} = \sum_{\mathbf{a}} \int \mathcal{D}[\phi] e^{-S_{\mathbf{a}}[\phi]} \tag{3.47}$$

and the $\mathbf{a}$ dependent action $S_{\mathbf{a}}$ are

$$\begin{aligned} S_{\mathbf{a}}[\phi] = \int d\tau [& \sum_{i,j} (\dot{\phi}_i - a_{i0}) \frac{C_{i,j}}{4} (\dot{\phi}_j - a_{j0}) \\ & + E_J \sum_i (1 - \cos(\Delta\phi_i - a_{i1}))] \end{aligned} \tag{3.48}$$

where $\mathbf{a}$ labels the sets of branch cuts. Since the path integral is invariant under a change of variable $\phi \rightarrow \phi + \Lambda$, $(a_0, a_1) \rightarrow (a_0 + \partial_\tau \Lambda, a_1 + \Delta\Lambda)$ is a gauge symmetry. Therefore, we can choose the non gauge equivalent branch cuts to be composed of vertical cuts,

$$\mathbf{a}_i(\tau) = (0, \pm 2\pi \delta_{i,x_v} \Theta(\tau_v - \tau)) \tag{3.49}$$

where x_v and τ_v are the coordinates of the end point of the branch cuts (vortices/antivortices), which are determined by the $(\pm)$ sign; and horizontal branch cuts,

$$\mathbf{a}_i(\tau) = (\pm 2\pi\delta(\tau)\Theta(x_{v_1} < i < x_{v_2}), 0). \tag{3.50}$$

Finally, there are also full branch cuts that does not have vortices. These are defined as $\mathbf{a}_i(\tau) = (0, \pm 2\pi\delta_{i,0})$ or $\mathbf{a}_i(\tau) = (\pm 2\pi\delta(\tau), 0)$.

Next, we split the field into smooth and fast part.

$$\phi = \phi_s + \phi_f \tag{3.51}$$

where ϕ_s is defined by $\sqrt{(\partial_\tau\phi_s - a_0)^2 + (\Delta\phi_s - a_1)^2}$ being small. The configurations that contribute more are ones with $\phi_f \simeq 0$ everywhere except near the vortices ($(x,\tau) \sim (x_v, \tau_v)$), where $\mathcal{L}_{\mathbf{a}}(\dot{\phi}_f, \phi_f) \gg \mathcal{L}_{\mathbf{a}}(\dot{\phi}_s, \phi_s)$. Therefore,

$$\begin{aligned} Z_{JJC} &= \sum_{\mathbf{a}} \int \mathcal{D}[\phi_s]\mathcal{D}[\phi_f] e^{-S_{\mathbf{a}}[\phi_s+\phi_f]} \\ &\simeq \sum_{\mathbf{a}} \int \mathcal{D}[\phi_s] e^{-S_{\mathbf{a}}[\phi_s]} \int \mathcal{D}[\phi_f] e^{-S_{\mathbf{a}}[\phi_f]} \\ &\simeq \sum_{\mathbf{a}} \int \mathcal{D}[\phi_s] e^{-S_{\mathbf{a}}[\phi_s]} \prod_{v\in\mathbf{a}} \int \mathcal{D}[\phi_f] e^{-S_v[\phi_f]} \\ &\equiv \sum_{\mathbf{a}} \gamma^{n_{\mathbf{a}}} \int \mathcal{D}[\phi_s] e^{-S_{\mathbf{a}}[\phi_s]} \end{aligned} \tag{3.52}$$

where v labels vortices in the set of branch cuts $\mathbf{a}$, $S_v[\phi_f] = \sum_{x\sim x_v} \int_{\tau\sim\tau_v} d\tau \mathcal{L}(\dot{\phi}_f, \phi_f)$ and γ is the contribution from integrating ϕ_f near a single vortex/antivortex, $n_{\mathbf{v}}$ is the number of

vortices. Finally, since ϕ_s is smooth, we can approximate $S_{\mathbf{a}}[\phi_s]$ by the free action $S_{0,\mathbf{a}}[\phi_s] = \int d\tau[\sum_{i,j}(\dot{\phi}_i - a_{i0})\frac{C_{i,j}}{4}(\dot{\phi}_j - a_{j0}) + \frac{E_J}{2}\sum_i(\Delta\phi_i - a_{i1})^2]$, this gives the following form of the partition function.

$$Z_{JJC} = \sum_{\mathbf{a}} \gamma^{n_{\mathbf{a}}} \int \mathcal{D}[\phi_s] e^{-S_{0,\mathbf{a}}[\phi_s]} \tag{3.53}$$

To solve for Z_{JJC}, it is more convenient to work in the Fourier space,

$$\begin{aligned} \phi_m(\tau) &= \frac{1}{\sqrt{M}} \sum_{k,\omega} \tilde{\phi}_{k,\omega} e^{i(km-\omega\tau)} \\ \mathbf{a}_m(\tau) &= \frac{1}{\sqrt{M}} \sum_{k,\omega} \tilde{\mathbf{a}}_{k,\omega} e^{i(km-\omega\tau)}, \end{aligned} \tag{3.54}$$

where M is the system size and $k \in \{\frac{2n\pi}{M} | n \in \{-M/2...M/2\}\}$, $\omega \in \{\frac{2n\pi}{\beta} | n \in \mathbb{Z}\}$. This gives

$$\begin{aligned} &S_{0,\mathbf{a}}[\phi_s]/\beta = \\ &\sum_{(k,\omega)\neq(0,0)} A_{k,\omega} |\tilde{\phi}_{k,\omega} - \frac{(E_J/2)(1-e^{ik})\tilde{a}_1 + i(\omega\tilde{C}_k/4)\tilde{a}_0}{A_{k,\omega}}|^2 \\ &+ \frac{\tilde{C}_0}{4}|\tilde{a}_{0;(0,0)}|^2 + \frac{E_J}{2}|\tilde{a}_{1;(0,0)}|^2 \\ &+ (\frac{E_J\tilde{C}_0}{8}) \sum_{(k,\omega)\neq(0,0)} \frac{|(1-e^{-ik})\tilde{a}_0 + i\omega\tilde{a}_1|^2}{A_{k,\omega}} \end{aligned} \tag{3.55}$$

where $\tilde{C}_k = \sum_m C_m e^{ikm}$, $A_{k,\omega} = \omega^2 \tilde{C}_k/4 + 2E_J \sin^2(k/2)$. Next, using $\mathcal{D}[\phi_s] = J \prod_{k,\omega} d\tilde{\phi}_{k,\omega}$,

$$
\begin{aligned}
Z_{JJC} = J \sum_{\mathbf{a}} \{ & \gamma^{n_{\mathbf{a}}} e^{-\beta[(\tilde{C}_0/4)|\tilde{a}_{0;(0,0)}|^2 + (E_J/2)|\tilde{a}_{1;(0,0)}|^2]} \\
& \times \prod_{(k,\omega)\neq(0,0)} [e^{-\frac{\beta E_J \tilde{C}_k}{8A_{k,\omega}}|(1-e^{-ik})\tilde{a}_0 + i\omega\tilde{a}_1|^2} \\
& \qquad \times \int d\tilde{\phi}_{k,\omega} e^{-\beta A_{k,\omega}|\tilde{\phi}_{k,\omega}|^2}]\} \\
\propto \sum_{\mathbf{a}} \{ & \gamma^{n_{\mathbf{a}}} e^{-\beta[(\tilde{C}_0/4)|\tilde{a}_{0;(0,0)}|^2 + (E_J/2)|\tilde{a}_{1;(0,0)}|^2]} \\
& \times \prod_{(k,\omega)\neq(0,0)} e^{-\frac{\beta E_J \tilde{C}_k}{8A_{k,\omega}}|(1-e^{-ik})\tilde{a}_0 + i\omega\tilde{a}_1|^2} \}
\end{aligned}
\tag{3.56}
$$

Note that the set of broken branch cuts $\mathbf{a}$ and the vortex configuration has a 1-to-1 correspondence. Therefore, we can relabel $\mathbf{a}$ by $(n_\tau, n_x, \mathbf{v})$ which denotes the number of 2π jumps at the x and τ boundary and the vortex configuration.

For the second term, by Eq. 3.49 and Eq. 3.50, $\tilde{\mathbf{a}}_{(0,0)}$ are related to the polarization of $\mathbf{v}$ up to full branch cuts,

$$
\begin{aligned}
\tilde{a}_{0;(0,0)} &= \frac{1}{\beta\sqrt{M}} \sum_m \int a_{0,m}(\tau) d\tau \\
&= \frac{2\pi}{\beta\sqrt{M}} (M n_\tau + \sum_{v\in\mathbf{v}} x_v s_v) \\
&\equiv \frac{2\pi}{\beta\sqrt{M}} (M n_\tau + P_{x,\mathbf{v}})
\end{aligned}
\tag{3.57}
$$

$$\begin{aligned}\tilde{a}_{1;(0,0)} &= \frac{1}{\beta\sqrt{M}}\sum_m \int a_{1,m}(\tau)d\tau \\ &= \frac{2\pi}{\beta\sqrt{M}}(\beta n_x + \sum_{v\in\mathbf{v}} \tau_v s_v) \\ &\equiv \frac{2\pi}{\beta\sqrt{M}}(\beta n_x + P_{\tau,\mathbf{v}}) \end{aligned} \tag{3.58}$$

where $s_v = \pm 1$ for vortices/antivortices. The polarization is defined as $P_{\mathbf{v}} = (\sum_{v\in\mathbf{v}} \tau_v s_v, \sum_{v\in\mathbf{v}} x_v s_v)$. Next, for the third term, the exponent contains a discrete version of $curl$ $\mathbf{a}$ which can also be rewritten as the vortex density,

$$|(1-e^{-ik})\tilde{a}_0 + i\omega\tilde{a}_1|^2 = \frac{4\pi^2}{\beta^2 M}|B_{\mathbf{v};k,\omega}|^2 \tag{3.59}$$

where $B_{\mathbf{v};k,\omega} \equiv \sum_{v\in\mathbf{v}} s_v e^{-i(kx_v - \omega\tau_v)}$. Therefore, the partition function representing in terms of the vortex configuration is

$$\begin{aligned} Z_{JJC} \sim \sum_{\mathbf{v}} \{\gamma^{n_{\mathbf{v}}} \sum_{n_x,n_\tau} & e^{-[\frac{\pi^2\tilde{C}_0}{\beta M}(Mn_\tau + P_{x,\mathbf{v}})^2 + \frac{2\pi^2 E_J}{\beta M}(\beta n_x + P_{\tau,\mathbf{v}})^2]} \\ & \times \prod_{(k,\omega)\neq(0,0)} e^{-\frac{\pi^2 E_J \tilde{C}_k}{2\beta M}(\frac{|B_{\mathbf{v};k,\omega}|^2}{A_{k,\omega}})}\} \end{aligned} \tag{3.60}$$

Finally, to make connection to the s-G model that is going to be introduced later, we perform a Poisson resummation on the discrete Gaussians. This gives

$$\begin{aligned} Z_{JJC} \sim \sum_{\mathbf{v}} \{\gamma^{n_{\mathbf{v}}} \sum_n & e^{-\frac{\beta}{M\tilde{C}_0}n^2 + i\frac{2\pi P_{x,\mathbf{v}}}{M}n} \sum_n e^{-\frac{M}{2\beta E_J}n^2 + i\frac{2\pi P_{\tau,\mathbf{v}}}{M}n} \\ & \times \prod_{(k,\omega)\neq(0,0)} e^{-\frac{\pi^2 E_J \tilde{C}_k}{2\beta M}(\frac{|B_{\mathbf{v};k,\omega}|^2}{A_{k,\omega}})}\} \end{aligned} \tag{3.61}$$

Next, we derive the partition function Z_{s-G} for sine-Gordon model defined as

$$H_{s-G} = \sum_{i,j} N_j U_{i,j} N_j + \frac{E_J}{2} \sum_j (\phi_j - \phi_{j-1})^2 + g \sum_j cos(\theta_j). \tag{3.62}$$

It is convenient to perform a charge-vortex transformation $(\phi, N) \rightarrow (\theta, \Pi)$, with the relation

$$\begin{aligned} N_i &= (\theta_i - \theta_{i-1})/2\pi \\ \Pi_i &= (\phi_{i+1} - \phi_i)/2\pi. \end{aligned} \tag{3.63}$$

One can easily check that the commutation relation $[\theta_i, \Pi_j] = i\delta_{i,j}$ is preserved. In terms of θ and Π,

$$\begin{aligned} H_{s-G} = &\sum_{i,j} (\theta_i - \theta_{i-1}) \frac{U_{i,j}}{4\pi^2} (\theta_j - \theta_{j-1}) \\ &+ 2\pi^2 E_J \sum_j \Pi_j^2 + g \sum_j cos(\theta_j). \end{aligned} \tag{3.64}$$

Using the path integral formalism, the partition function can be written as,

$$Z_{s-G} = \sum_{n_x, n_\tau} \int_{\theta(\beta)=\theta(0)} \mathcal{D}[\theta] e^{-S_{n_x, n_\tau}} \tag{3.65}$$

where n_x, n_τ labels the boundary condition defined by

$$\begin{aligned} \theta_{M+1}(\tau) &= \theta_1(\tau) + 2\pi n_x \\ \theta_j(\beta) &= \theta_j(0) + 2\pi n_\tau \end{aligned} \tag{3.66}$$

and the imaginary time action can be written as

$$S_{n_x,n_\tau} = \int_0^\beta d\tau [\frac{1}{8\pi^2 E_J} \sum_j (\dot{\theta}_j + \frac{2\pi n_\tau}{\beta})^2 + \sum_{i,j} (\theta_i - \theta_{i-1} + \frac{2\pi n_x}{M}) \frac{U_{i,j}}{4\pi^2} (\theta_j - \theta_{j-1} + \frac{2\pi n_x}{M}) + g \sum_j cos(\theta_j + \frac{2\pi j}{M} n_x + \frac{2\pi \tau}{\beta} n_\tau)]. \tag{3.67}$$

Working perturbatively in small g,

$$Z_{s-G} = \sum_{n_x,n_\tau} \sum_n \frac{1}{n!} (-\frac{g}{2})^n \sum_{l_1,l_2,\ldots,l_n} \int \prod_{j=1}^n d\tau_j \sum_{\{\mathbf{s}\}} \int \mathcal{D}[\theta] e^{-S_{0,n_x,n_\tau} + i \sum_j s_j [\theta_{l_j}(\tau_j) + \frac{2\pi l_j}{M} n_x + \frac{2\pi \tau_j}{\beta} n_\tau]} \tag{3.68}$$

where $\{\mathbf{s}\}$ sums over the signs (± 1) and the free action S_0 is given by

$$\begin{aligned} S_{0;n_x,n_\tau} &= \int_0^\beta d\tau [\frac{1}{8\pi^2 E_J} \sum_j (\dot{\theta}_j + \frac{2\pi n_\tau}{\beta})^2 \\ &\quad + \sum_{i,j} (\theta_i - \theta_{i-1} + \frac{2\pi n_x}{M}) \frac{U_{i,j}}{4\pi^2} (\theta_j - \theta_{j-1} + \frac{2\pi n_x}{M})] \\ &= \frac{M}{2\beta E_J} n_\tau^2 + \frac{\beta \tilde{U}_0}{M} n_x^2 \\ &\quad + \sum_{(k,\omega)\neq(0,0)} [\frac{\beta}{8\pi^2 E_J} \omega^2 + \frac{\beta \sin^2(k/2)}{\pi^2} \tilde{U}_k] |\tilde{\theta}_{k,\omega}|^2. \end{aligned} \tag{3.69}$$

where $\tilde{U}_k = \sum_l U_l e^{ikl}$ and the Fourier transformation of the θ fields are defined as

$$\begin{aligned}\theta_l(\tau) &= \frac{1}{\sqrt{M}} \sum_{k,\omega} \tilde{\theta}_{k,\omega} e^{i(kl-\omega\tau)} \\ \tilde{\theta}_{k,\omega} &= \frac{1}{\beta\sqrt{M}} \sum_{l} \int d\tau \theta_l(\tau) e^{-i(kl-\omega\tau)}\end{aligned} \tag{3.70}$$

where M, k, and ω has the same definition as above. Let $\mathcal{D}[\theta] = J \prod_{k,\omega} d\tilde{\theta}_{k,\omega}$,

$$\begin{aligned}Z_{s-G} = J \sum_{\mathbf{v}} (-\frac{g}{2})^{n_{\mathbf{v}}} \\ \times \sum_{n_\tau} e^{-\frac{M}{2\beta E_J} n_\tau^2 + i\frac{2\pi P_{\tau,\mathbf{v}}}{\beta} n_\tau} \sum_{n_x} e^{-\frac{\beta\tilde{U}_0}{M} n_x^2 + i\frac{2\pi P_{x,\mathbf{v}}}{M} n_x} \\ \times \prod_{k,\omega} \int d\tilde{\theta}_{k,\omega} e^{-\frac{\beta\tilde{U}_k}{2\pi^2 E_J} A_{k,\omega} |\tilde{\theta}_{k,\omega}|^2 + i\frac{1}{\sqrt{M}} B_{\mathbf{v};k,\omega} \tilde{\theta}_{k,\omega}}\end{aligned} \tag{3.71}$$

where $\sum_{\mathbf{v}} \equiv \sum_n \frac{1}{n!} \sum_{l_1,l_2,\ldots,l_n} \int \prod_j^n d\tau_j \sum_{\{\mathbf{s}\}}$ is an analog of the sum over vortex configurations and $n_{\mathbf{v}}$ represents the number of vortices. We will use this notation and index the vortices by v. Again, $A_{k,\omega} = \omega^2/4\tilde{U}_k + 2E_J \sin^2(k/2)$, $B_{\mathbf{v};k,\omega} = \sum_{v\in\mathbf{v}} s_v e^{i(kx_v - \omega\tau_v)}$ and $P_{\mathbf{v}}$ is the polarization of the charges with the same definition, $(P_{\tau,\mathbf{v}}, P_{x,\mathbf{v}}) \equiv (\sum_{v\in\mathbf{v}} \tau_v s_v, \sum_{v\in\mathbf{v}} x_v s_v)$. First, the integral over $\tilde{\theta}'s$ are Gaussian integrals

$$\begin{aligned}&\prod_{k,\omega} \int d\tilde{\theta}_{k,\omega} e^{-\frac{\beta\tilde{U}_k}{2\pi^2 E_J} A_{k,\omega} |\tilde{\theta}_{k,\omega}|^2 + i\frac{1}{\sqrt{M}} B_{\mathbf{v};k,\omega} \tilde{\theta}_{k,\omega}} \\ &= \prod_{k,\omega} \sqrt{\frac{\pi^3 E_J}{\beta\tilde{U}_k A_{k,\omega}}} e^{-\frac{\pi^2 E_J}{2\beta M\tilde{U}_k} (\frac{|B_{\mathbf{v};k,\omega}|^2}{A_{k,\omega}})} \\ &\propto \prod_{k,\omega} e^{-\frac{\pi^2 E_J}{2\beta M\tilde{U}_k} (\frac{|B_{\mathbf{v};k,\omega}|^2}{A_{k,\omega}})}\end{aligned} \tag{3.72}$$

Using the fact that the only configurations that are going to contribute are the charge neutral ones

with $\sum_{v\in\mathbf{v}} s_v = 0$ and $n_{\mathbf{v}}$ is thereby an even number,

$$\begin{aligned} Z_{s-G} \sim & \sum_{\mathbf{v}} (\frac{g}{2})^{n_{\mathbf{v}}} \\ & \times \sum_n e^{-\frac{M}{2\beta E_J} n^2 + i\frac{2\pi P_{\tau,\mathbf{v}}}{\beta} n} \sum_n e^{-\frac{\beta \tilde{U}_0}{M}^2 + i\frac{2\pi P_{x,\mathbf{v}}}{M} n} \\ & \times \prod_{k,\omega} e^{-\frac{\pi^2 E_J}{2\beta M \tilde{U}_k} (\frac{|B_{\mathbf{v};k,\omega}|^2}{A_{k,\omega}})}. \end{aligned} \tag{3.73}$$

One can see that this form exactly matches Z_{JJC} in (3.61) with g chosen as

$$g = 2\gamma \equiv 2 \int \mathcal{D}[\phi_f] e^{-\sum_{x\sim x_v} \int_{\tau\sim\tau_v} d\tau \mathcal{L}_v(\dot{\phi}_f, \phi_f)}. \tag{3.74}$$

3.2.3 Numerically Extracting g from Microscopic Calculation of the Decay Rate

In this section we introduce a method to obtain g from the microscopic model in the perturbative regime of the phase slip. We consider the decay rate of the original microscopic Hamiltonian H in Eq. 3.42 due to phase slip at a particular site corresponding to $e^{i\theta_1}$, whose profile is given in Eq. 3.36. This decay can be evaluated by Fermi's golden rule,

$$\Gamma_0(q) = \frac{1}{2\pi} \sum_n |M_{n,q}|^2 \delta(\omega_q - \epsilon_n) \tag{3.75}$$

where $M_{n,q} = \langle n|e^{-i\theta_1}(H - \langle H\rangle_q)|q\rangle$, $|n\rangle$ being eigenstates of H_0. The expectation value $\langle H\rangle_q \equiv \langle q|H|q\rangle$ is presented to account for the fact that states $|q\rangle$ and $e^{i\theta_1}|n\rangle$ are not exactly orthogonal to each other.

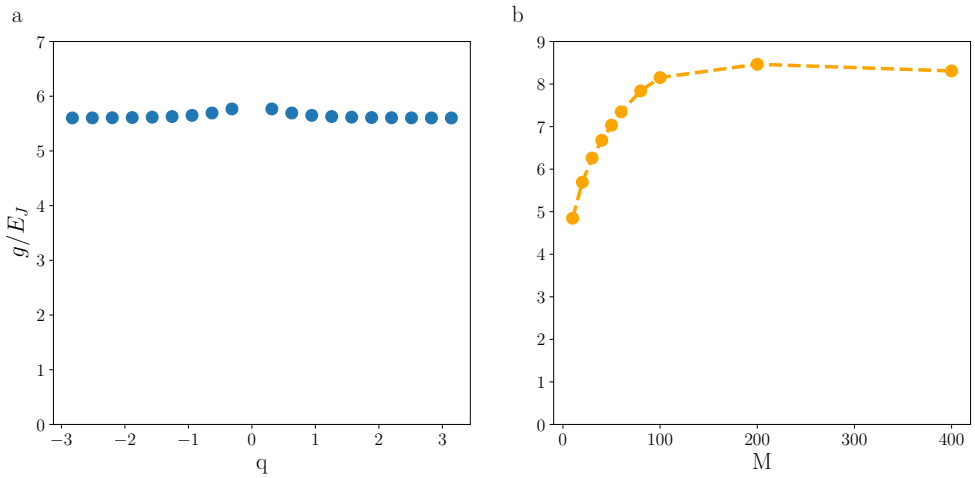

Figure 3.3: QPS strength g evaluated by (3.76) under (a) different momentum with fixed system size $M = 40$ and (b) different system size with $q = 0.2\pi$. System parameters are chosen to be $E_0/E_J = 2$, $E_1/E_J = 0.5$, and the energy broadening is set to be $\omega_{q_{min}}$.

The quantum phase slip strength (g) can then be obtained by taking the ratio between decay rate from (3.75) and that given by the sine-Gordon term

$$\frac{g^2}{4} = \frac{\Gamma_0(q)}{\Gamma_{SG}(q)} \tag{3.76}$$

where $\Gamma_{SG}(q) = \frac{1}{2\pi}\sum_n |\langle n|e^{-i\theta_1}|q\rangle|^2\delta(\omega_q - \epsilon_n)$. An example of the numerical simulation is shown in Fig. 3.3. As expected, g shows small q and system size M dependence at large M. Therefore, g can be evaluated by taking averages over all momentum q's.

3.2.4 Soliton-antisoliton Pair Excitation Rates

The elementary excitations of the sine-Gordon model described by Eq. 3.1 are solitons (antisolitons) where the phase θ jumps by $\pm\pi$ between different minima of the cosine potential in Eq. 3.1. Since the phase θ is related to the charge density $\rho(x) \propto \partial_x\theta$, so that such solitons (antisolitons) are associated with charge $\pm 2e$. A more exact treatment of these apparently static

domain walls in the sine-Gordon Hamiltonian reveals that such solitons can be viewed as essentially non-interacting relativistic quantum particles with a dispersion (energy versus momentum relation) that is written as

$$\omega_{s/a}(q) = \pm\sqrt{m^2 + q^2 v_c^2} \tag{3.77}$$

and is plotted in Fig. 3.4(a). The index s/a stand for solitons and antisolitons respectively. The energy of the anti-soliton is shown with a negative sign for convenience of later discussion. The mass parameter is given by [110]

$$m = \Upsilon \left[g \frac{\pi\Gamma(1-K/2)}{4\Upsilon\Gamma(K/2)} \right]^{1/(2-K)} \frac{2\Gamma(\xi/2)}{\sqrt{\pi}\Gamma((1+\xi)/2)}, \tag{3.78}$$

where $\xi = K/(2-K)$ and Υ is a momentum cut-off scale.

Let us now discuss qualitatively the origin of the oscillations in the ac polarizability $\chi(\omega)$ in terms of the solitons and anti-solitons discussed above. The polarizability $\chi(\omega)$ is measured by the absorption of photons from the probe at the end of the JJ chain (see Fig. 3.1), so that $\chi(\omega)$ must be associated with the cross-section for generating neutral excitations. More formally

$$\chi(\omega) = \left\langle \rho(x;\omega)^\dagger \rho(x;\omega) \right\rangle = \sum_n |\langle 0|\rho(x)|n\rangle|^2 \delta(E_n - \omega), \tag{3.79}$$

where $\rho(x)$ is the charge density operator at the end of the chain. The state $|0\rangle$ represents the ground state of the system and $|n\rangle$ is an excited state with energy E_n above the ground state. Such neutral excitations can be constructed by pairing the elementary solitons and antisolitons, which are charged, into soliton-antisoliton pairs (SAPs). One such pair with center of mass

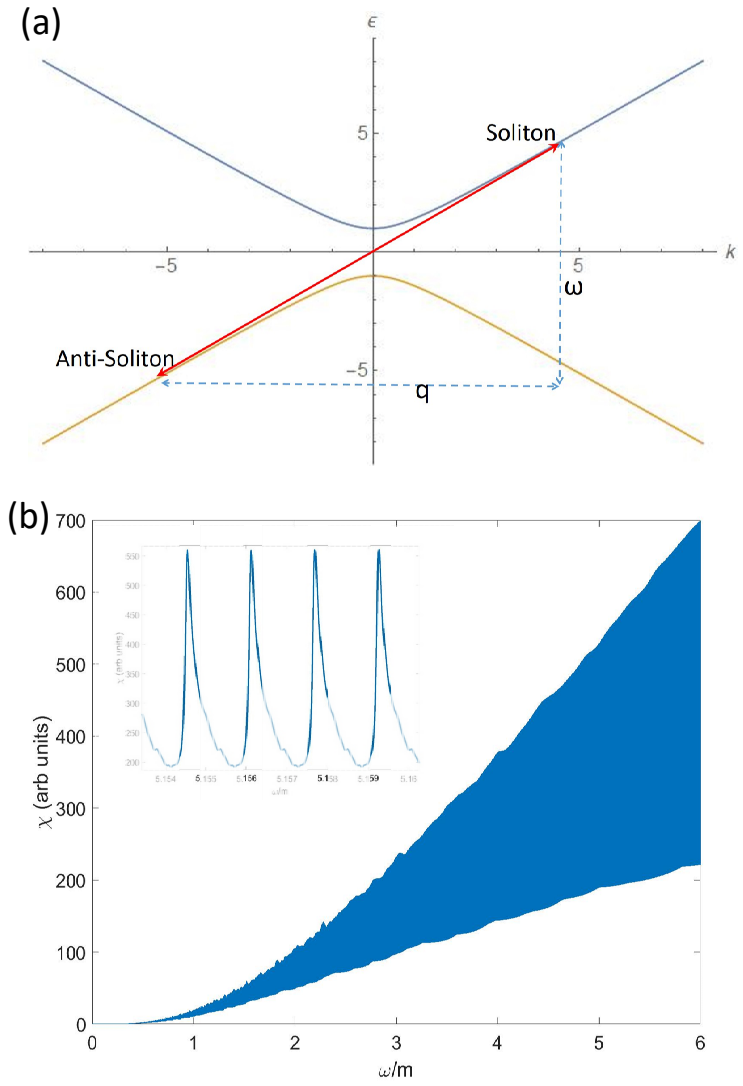

Figure 3.4: (a) Dispersion (ε versus k) of excitations of the sine-Gordon model with anti-solitons at negative energy. The bold arrow shows charge neutral soliton-antisolition pairs with momentum q and energy ω. Large q pairs have a large near-degeneracy with $\omega \simeq q$ constituting a coherent excitation peak. (b) Local dynamical polarizability χ of a sine-Gordon model as a function of ω. The parameter set is chosen to be $L = 3000, v_c = 1, m = 0.1$. The polarizability shows coherent peaks (see inset) spaced by finite size $1/L$ dominating over the incoherent background as frequency increases. Near $\omega \to 0$, a mass gap of $2m$ appears, in consistent with the insulating phase of the chain.

momentum q is shown in Fig. 3.4(a). In this figure, we have flipped the sign of the anti-soliton energy (as mentioned in the previous paragraph) so that we can extract the energy of the SAP from the separation along the axis $\omega_{SAP}(q) = \omega$ (see Fig. 3.4(a)). However, the pair shown in Fig. 3.4(a) represents one of a continuum of such pairs at momentum q, that are parametrized by the relative momentum k so that $|n\rangle$ would be the state $|n\rangle \equiv \left|S_{k+q/2}, A_{k-q/2}\right\rangle$ where S_k is the soliton with momentum k and A_k is an anti-soliton with momentum k. Therefore the more general energy of such a pair is given by

$$\omega_{SAP,k}(q) = \omega_s(k + q/2) - \omega_a(k - q/2). \tag{3.80}$$

Clearly the energy of of SAPs $\omega_{SAP,k}(q)$ acquires a natural broadening from the dependence on k while q is held fixed. In fact, the energy of the SAPs at momentum q can take any value $\omega > \sqrt{q^2 + 4m^2}$ by choosing

$$k = \frac{\omega}{2}\sqrt{\frac{\omega^2 - q^2 - 4m^2}{\omega^2 - q^2}}. \tag{3.81}$$

The density of states (DOS) for the SAPs in the vicinity of a given energy ω, is proportional to $dk/d\omega$, which diverges as

$$\frac{dk}{d\omega} \sim (q^2 + 4m^2)^{3/4}(\omega - \sqrt{q^2 + 4m^2})^{-1/2}. \tag{3.82}$$

This leads to a broadened peak in optical absorption near $\omega \sim \sqrt{q^2 + 4m^2}$. This is reminescent of the broadening of the magnon mode in the transverse field Ising model where a magnon fractionalizes into domain walls [79]. The prefactor $(q^2+4m^2)^{3/4}$ in Eq. 3.82 also shows that this

peak increases in height as q approaches the ultra-relativistic limit $q \gg 2m$. The experimental set-up shown in Fig. 3.1 does not conserve total momentum q. In contrast, one can excite an array of momenta $q = 2\pi n/L$, where L is the length of the chain. Considering all possible q can expect $\sigma_{ac}(\omega)$ to contain an array of peaks corresponding to the divergent DOS of SAPs in Eq. 3.82 from each of the allowed values of q. In principle, one should also consider discrete k so that the absorption spectrum should have a discrete set of peaks with no broadening. However, the spacing of the frequency arising from discreteness of k is expected to vanish as one approaches the peak of the DOS.

The above qualitative argument ignores the matrix elements that would determine the absorption cross-sections of the allowed SAPs. To obtain a more quantitative understanding of the dynamical charge susceptibility we compute $\sigma_{ac}(\omega)$ directly. Unfortunately, for general values of K, the charge operator can couple to multiple SAPs simultaneously (even though we expect this to be rare). To avoid this complication we restrict our attention to $K \simeq 1$, which is deep in the insulating phase. The sine-Gordon model is known to be dual to the massive Thirring model [89, 95, 111], which describes massive Dirac fermions with current-current interaction $H_{int} = g_T j^\mu j_\mu$ whose strength is given by $g_T = \pi(1 - 1/K)$. Therefore, at $K = 1$, the solitons and antisolitons are mapped to free Dirac fermions and the charge density operator couples to exactly one soliton-antisoliton pair. This is not necessarily a huge restriction because even at K significantly different from 1, at small values of g, the low frequency properties are still dominated by $K = 1$, which is one of the Luther-Emery fixed points [89, 95]. For the rest of this and the next section we set the charge velocity $v_c = 1$. In the limit $K = 1$, the sine-Gordon

model Eq. 3.1 is equivalent [111] to the massive 1D Dirac model with Hamiltonian

$$H = \sum_k \psi_k^\dagger [k\sigma_z + m\sigma_x]\psi_k, \tag{3.83}$$

where $\psi_k^\dagger$ are spinors of creation operators for solitons and anti-solitons in Eq. 3.1. The imaginary part of the local dynamical (i.e. ω dependent) polarizability χ is given by [112]

$$\chi(\omega) \simeq \sum_q \frac{2m^2q^2}{(\omega^2 - q^2)^{3/2}\sqrt{\omega^2 - q^2 - 4m^2}} \Theta(\omega^2 - q^2 - 4m^2). \tag{3.84}$$

The sum over momentum states q takes a discrete set of multiples of $2\pi/L$, where L is the length of the chain. This result suggests that the susceptibility χ diverges at an array of frequencies near $\omega_n^2 \simeq (2n\pi/L)^2 + 4m^2$, where χ diverges as $(\omega - \sqrt{q^2 + 4m^2})^{-1/2}$. In contrast, χ decays as $\chi \sim 2m^2q^2/\omega^4$ for $\omega \gg q$. Thus, we expect the susceptibility χ to be a broadened set of peaks qualitatively similar to that seen experiment [1].

This expectation is confirmed from the direct numerical evaluation of Eq. 3.79 for a finite system as is plotted in Fig. 3.4(b). As shown in the inset of Fig. 3.4(b), the shaded areas in Fig. 3.4(b) are really a closely spaced set of peaks on an incoherent background. The shape of the peaks is consistent with the analytic expectations. Considering the shaded areas in Fig. 3.4(b), which elucidates the height of the coherent peaks, we see that the height of the oscillations increases with frequency relative to the height of the incoherent background, which is consistent with the experiments [1]. For the numerical evaluation, we have broadened the delta functions in Eq. 3.79 by $0.1(2\pi/L)$ (where L is the chain length), which is much smaller than the plasmon level spacing. The value of the broadening does not appear to affect the result as long as it

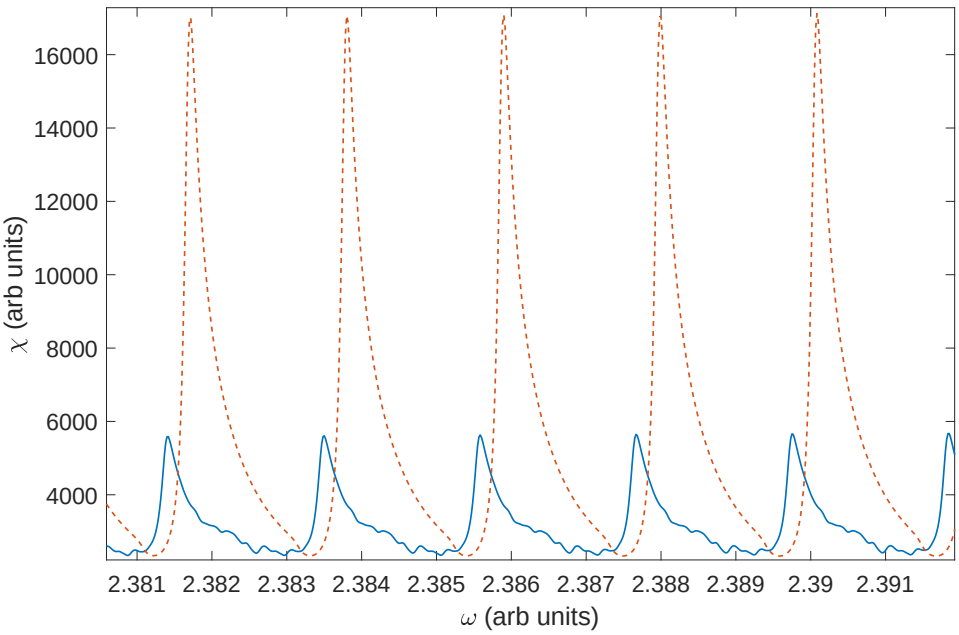

Figure 3.5: Luttinger parameter K dependence of resistance oscillations. Change in Luttinger parameter decreases the mass gap m and enhances the oscillation for $K = 1.4$ (red dashed line). The solid blue curve shows suppressed oscillations at $K = 1$ since the frequency is of order mass.

is smaller than the peak spacing since $o(L)$ SAPs contribute to each peak that are spaced by $o(1/L)$. Thus we do not expect the broadening to affect the shape of the peaks as long as it is larger than $o(1/L^2)$.

The discussion above for $K = 1$ also applies for $K \gtrsim 1$. In this case the excitation process in the non-interacting massive Dirac model is replaced by the form factor for creating an unbound SAPs [113]. For the general interacting case, contributions from multiple pairs must be considered. However, such contributions are likely to be small at low energies because of phase space constraints as well as weak interactions near $K \sim 1$. The dominant interaction of changing the Luttinger paramter K is to renormalize the mass downwards with increasing K following Eq. 3.78. Reducing the mass m, effectively increases the dimensionless frequency ω/m, which determines the height of peaks in the dynamical polarizability χ. This suggests, following the results in Fig. 3.4(b), that increasing the Luttinger parameter K enhances the

strength of oscillations in χ for a fixed frequency.

An additional contribution to the K dependence of the dynamical charge polarizability χ is the matrix element for the charge density operator ρ. Specifically, Bethe ansatz methods have been used to show that this matrix element is modified by a factor [114]

$$f_{-}(\vartheta) = \frac{\cosh\frac{i\pi-\vartheta}{2}}{2\cosh\frac{(i\pi-\vartheta)K}{2}} \times \exp\int_0^\infty \frac{dt}{t}\frac{\sinh\frac{(K-1)t}{2K}[1-\cosh t(1+\frac{i\vartheta}{\pi})]}{\sinh(t)\sinh\left(\frac{t}{2K}\right)\cosh\left(\frac{t}{2}\right)} \tag{3.85}$$

and ϑ_j are the rapidities of the solitons that are defined by the equation $k_j = m\sinh\vartheta_j$. For weakly attractive fermions, $K \gtrsim 1$, the interaction part of the form factor $f \sim \vartheta$ for small ϑ and $f \sim e^{\alpha\vartheta}$ for $\vartheta \gg 1$, where α is a K dependent constant. For $q \gg m$, $\vartheta \sim \log q$ so $f \propto q^{2\alpha}$. This leads to a K dependent power law for the increasing of the absorption peaks as one goes to more strongly attractive fermions i.e. towards the superfluid phase. A stronger K dependence of the peaks arises from the soliton mass in Eq. 3.78.

The dynamical polarizability χ at $K \gtrsim 1$, computed using Eq. 3.79 within the one SAP approximation described above, is plotted in Fig. 3.5. Consistent with the theoretical expectation, Fig. 3.5 shows the suppression of oscillations as one increases the Luttinger parameter K towards the the superfludi phase. The results for deep in the insulating phase (i.e. $K \sim 1$), which are shown in the solid blue curve, shows suppressed oscillations consistent with recent experiments [1]. In comparison the red dashed curve 3.5, which is less insulating (i.e. $K \sim 1.4$), shows much stronger oscillations. As discussed earlier, the one SAP approximation cannot be used to consider Luttinger parameter K far from the non-interacting point $K = 1$.

3.2.5 Disordered Massive Dirac Model

Let us now consider the effect of weak potential disorder, which is an intrinsic part of the JJ chain set-up. As will be elaborated in the next section, the long range nature of the Coulomb interaction converts the uncorrelated random background charge into a smooth potential disorder. This allows the disorder potential to be consistent with the low-energy and long-wavelength limit required for the applicability of the sine-Gordon model. In this section, we restrict our analysis to $K \sim 1$ where we can map the sine-Gordon model with disorder potential to the massive Dirac model [111]:

$$H = \int dx \psi^{\dagger}(x)[(iv\partial_x \sigma_z + m\sigma_x - \mu(x))]\psi(x), \tag{3.86}$$

where $\psi^{\dagger}(x)$ are the Fourier transform of the spinors in Eq. 3.83. The disorder potential is included in $\mu(x)$, which is an uncorrelated potential that is assumed to be smooth on the scale of the spacing of the JJ chain. The fluctuations in the local potential $\mu(x)$ leads to back-scattering of fermions at energy E.

In this fermion picture, we can solve for the mean free path which corresponds to the localization length of the soliton/antisolitons Under the transformation $\psi \rightarrow i\sigma_z \psi$, the Dirac equation for $v = 1$ is written as

$$\partial_x \psi + [m\sigma_y - i\mu(x)\sigma_z]\psi = 0. \tag{3.87}$$

Transforming $\psi \to e^{i\phi(x)\sigma_z}\psi$, where $\phi(x) = \int_{x_1}^{x} dx'\mu(x')$, the equation becomes

$$\partial_x \psi = -m[\cos\phi(x)\sigma_y - \sin\phi(x)\sigma_x]\psi. \tag{3.88}$$

Considering the evolution of $\psi(x)$ from $x = x_1$ to $x = x_2$

$$\psi(x_2) = e^{-i\phi(x_2)\sigma_z}[1 - m\int dx'\{\cos\phi(x')\sigma_y - \sin\phi(x')\sigma_x\}]\psi(x_1) \tag{3.89}$$

$$\equiv e^{-i\phi(x_2)\sigma_z}(1 + mA)\psi(x_1), \tag{3.90}$$

where

$$A = -\int dx'\{\cos\phi(x')\sigma_y - \sin\phi(x')\sigma_x\}$$

$$\equiv S\sigma_x + C\sigma_y. \tag{3.91}$$

The localization length λ can be found by extracting the decay of the wave function correlation with distance,

$$e^{-2(\frac{x_2-x_1}{\lambda})} \sim 1 - 2(\frac{x_2 - x_1}{\lambda}) = \langle(1 + mA)^2\rangle$$

$$= 1 + 2m(SX + CY) + m^2(C^2 + S^2) \tag{3.92}$$

where $X \equiv \langle\sigma_x\rangle$ and $Y \equiv \langle\sigma_y\rangle$. At $m = 0$, the uniform (Haar measure) distribution on the unit sphere is a stationary distribution. Therefore, this can be solved in the small m limit. For a

stationary distribution, expectation value of a local operator $\hat{O}$ should satisfy

$$\frac{\langle (1+mA)e^{i\phi(x_2)\sigma_z}\hat{O}e^{-i\phi(x_2)\sigma_z}(1+mA)\rangle}{\langle (1+mA)^2\rangle} = \langle \hat{O}\rangle. \tag{3.93}$$

By choosing $\hat{O} = \sigma_{x,y}$, we obtain the following equations,

$$\begin{aligned} X &= \frac{\langle (1+mA)[\cos\phi(x_2)\sigma_x - \sin\phi(x_2)\sigma_y](1+mA)\rangle}{\langle (1+mA)^2\rangle} \\ Y &= \frac{\langle (1+mA)[\sin\phi(x_2)\sigma_x + \cos\phi(x_2)\sigma_y](1+mA)\rangle}{\langle (1+mA)^2\rangle}. \end{aligned} \tag{3.94}$$

To lowest order in m,

$$\begin{aligned} \begin{pmatrix} X \\ Y \end{pmatrix} &= \frac{m}{1-\cos\phi(x_2)} \\ &\times \begin{pmatrix} \cos\phi(x_2)-1 & -\sin\phi(x_2) \\ \sin\phi(x_2) & \cos\phi(x_2)-1 \end{pmatrix} \begin{pmatrix} S \\ C \end{pmatrix}. \end{aligned} \tag{3.95}$$

Plugging X and Y into Eq. 3.92, we find that

$$2(\frac{x_2-x_1}{\lambda}) = m^2(C^2+S^2) \tag{3.96}$$

Next, we solve for the C^2+S^2. This involves averaging over disorder potential $\mu(x) = E+\xi(x)$. At length scale where ξ becomes uncorrelated, we can assumed $\langle\langle \xi(x)\xi(y)\rangle\rangle = V_0^2\Lambda\delta(x-y)$

where $V_0^2\Lambda$ characterizes the strength of the fluctuations in $\mu(x)$. Therefore,

$$\begin{aligned} C^2 + S^2 &= \int_{x_1}^{x_2} \langle\langle \cos\phi(x-x')\rangle\rangle dx dx' \\ &= 2\int_{x_1}^{x_2} dx \int_{x_1}^{x} dx' \cos(E(x-x')) e^{-\frac{V_0^2\Lambda}{2}(x-x')} \end{aligned} \tag{3.97}$$

In the large $x_2 - x_1$ limit, this gives

$$C^2 + S^2 \sim \frac{4V_0^2\Lambda}{4E^2 + V_0^4\Lambda^2}(x_2 - x_1). \tag{3.98}$$

Accordingly, we can conclude that the localization length, or the fermion mean-free path, is given by

$$\lambda = \frac{4E^2 + V_0^4\Lambda^2}{2m^2V_0^2\Lambda} \tag{3.99}$$

The mean-free path increases from $V_0^2\Lambda/2m^2$ to $2E^2/m^2V_0^2\Lambda$ as the energy E of the excited soliton/antisoliton increases from 0. Such a chain appears insulating for lengths that are longer than $L \gg V_0^2\Lambda/2m^2$. Note that the localization length diverges if the mass m drops to zero as is expected to occur near the superfluid phase from Eq. 3.78. Furthermore, we expect SAPs to be localized at low-frequency and not contribute to resonant excitations. In contrast, the dynamical polarizability χ at frequencies above $\omega \gg mV_0\sqrt{\Lambda L/2}$, is dominated by high energy delocalized (see Eq. 3.99) SAPs and should show sharp resonances similar to the clean result in Fig. 3.4.

These expectations can be verified from χ, which is calculated by a numerical evaluation of Eq. 3.79 for the Hamiltonian Eq. 3.86 and is plotted in Fig. 3.6. The result shows a disorder gap at

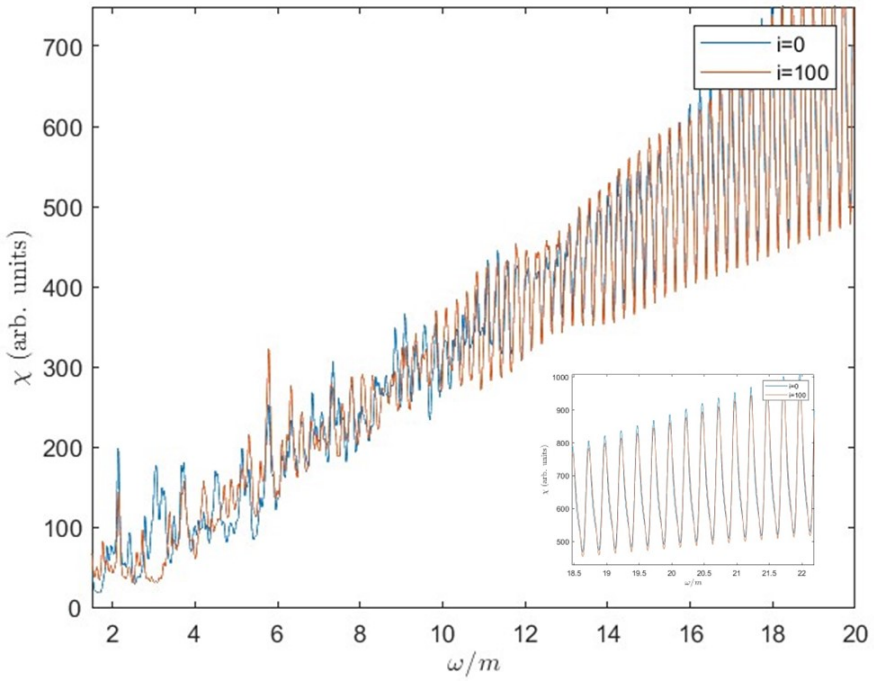

Figure 3.6: Local dynamical polarizability χ of the disordered massive Dirac model as a function of ω shows coherent peaks at high frequencies and smaller random absorption peaks at low frequencies. The low-frequency peaks are distinct between different sites, suggesting that the solitons and antisolitons are Anderson-localized. Inset shows that the peak shape in the disordered system, which is more symmetric compared to that in the clean system shown in the inset in Fig. 3.5.

low frequency and plasma oscillations at high frequency. Consistent with the intuitive argument at the beginning of this section, high frequency SAPs that contribute to χ with frequencies $\omega \gg m$ are not scattered by the disorder and therefore lead to coherent oscillations in $\chi(\omega)$ seen in Fig. 3.6. On the other hand, the low energy SAPs are pinned by the disorder domain walls. The low energy excitation constitutes bound resonances from exciting vibration modes of such bound solitons. Such solitons being localized and random appear as a sequence of random peaks in Fig. 3.6 that are qualitatively different from Fig. 3.4(b).

Despite the fact that such disorder breaks integrability, we can generalize these arguments to $K \gtrsim 1$. For a general sine-Gordon model (Eq. 3.1), weak potential disorder works as introducing a pinning potential for the massive solitons. For $K < 3/2$ and weak disorder, such potentials lead to pinning of all low energy solitons leading to an insulating phase [107]. Higher energy solitons, which can be obtained by applying a Lorentz boost, have shorter length scales and are therefore not scattered by smooth charge disorder. The coherent high energy SAPs can generate large coherent oscillations in the dynamical polarizability χ at high frequencies.

3.2.6 Nearly Superfluid Limit of the JJ Chain

We now consider the case where the array is closer to the superfluid phase. In this limit, the Luther-Emery model (Eq. 3.83) is no longer valid. Furthermore, the sine-Gordon model Eq. 3.1 ignores curvature effects in the energy. However, the effect of phase slips (i.e. g in Eq. 3.1) is perturbatively weak in this limit so that one can compute the decay directly from the microscopic model for a JJ chain that includes both island capacitance C_g, JJ capacitance C_J as well as charge disorder. In this section, we consider a more microscopically justified Hamiltonian for the system

that is written as:

$$H = \sum_{i,j} U_{i,j}(N_i - Q_i)(N_j - Q_j) + E_J \sum_i [1 - \cos(\phi_i - \phi_{i-1})] \tag{3.100}$$

where N_i and ϕ_i are number of Cooper pairs and phase at site i, E_J is the Josephson energy of junctions and

$$U_{i,j} = \frac{1}{M} \sum_q U_q e^{iq(R_i - R_j)} \tag{3.101}$$

where M is the system size and $U_q = 4E_0E_1/[E_1 + 4E_0 \sin^2(q/2)]$ charging energies $E_{0,1}$ are defined as $E_0 = e^2/2C_g$ and $E_1 = e^2/2C_J$. $\{Q's\}$ are normally distributed random stray charges which satisfy $\langle\langle Q_iQ_j\rangle\rangle = D\delta_{i,j}$. The corresponding random potential $\mu_i = \sum_j U_{i,j}Q_j$, has a Fourier transform

$$\langle\langle |\mu_q|^2 \rangle\rangle \approx D \frac{16E_0^2E_1^2}{(E_1 + E_0q^2)^2},$$

which is strongly peaked at $q \sim 0$ for $E_0 \gg E_1$. Thus the potential in this case can be assumed to be smooth as assumed in Eq. 3.86.

For energy of states below the Josephson energy E_J, we expect $(\phi_i - \phi_{i-1}) \ll 2\pi$. However, at low energies rare events called phase-slips locally shift one of the phase differences $(\theta_i - \theta_{i-1})$ by 2π. Such a phase slip is local i.e. it doesn't affect the phase ϕ_j for $|j - i| \gg 1$. This implies that the remaining of the phase differences add up to 2π immediately following the phase slip.

The phase-slip operator is simpler to represent in dual variables defined as

$$\pi_j = \phi_{j+1} - \phi_j \tag{3.102}$$

$$\theta_j = \sum_{l \leq j} N_l. \tag{3.103}$$

The commutation relation of these operators

$$[\theta_l, \pi_j] = \sum_{m \leq l} [N_m, \phi_{j+1} - \phi_j] \tag{3.104}$$

$$= i \sum_{m \leq l} (\delta_{j-m} - \delta_{j-m+1}) = i\delta_{j-l}. \tag{3.105}$$

A quantum phase slip at site j is created by an operator $e^{-i\bar{\theta}_j}$, where

$$\bar{\theta}_j = \sum_l w_{l-j} \theta_l, \tag{3.106}$$

where $w_l \geq 0$ are normalized weights peaks at $l = 0$ such that $\sum_l w_l = 2\pi$. The width of w_l represents the length-scale of the phase slip. Thus, phase-slips can be considered to be nucleated by a term $-g \sum_j \cos \bar{\theta}_j$. We can write the the low-energy effective Hamiltonian where the phase difference variables $\pi_j \ll 2\pi$, including the phase-slip term as

$$\begin{aligned} H = & \sum_{i,j} U_{i,j} (\theta_i - \theta_{i-1} - Q_i)(\theta_j - \theta_{j-1} - Q_j) \\ & + \frac{E_J}{2} \sum_i \pi_i^2 + g \sum_i \cos \bar{\theta}_i. \end{aligned} \tag{3.107}$$

The disorder from Q_j can be eliminated by a unitary transformation $e^{-i \sum_j Q_j \phi_j}$ which shifts $\bar{\theta}_j$ to

$\bar{\theta}_j + \Lambda_j$, where $\Lambda_j = \sum_l w_{l-j} \sum_{m=1}^{l} Q_m$.

Ignoring g for the moment, diagonalizing H under open boundary condition $\pi_1 = \pi_{M-1} = 0$ gives rise to sound-like plasmonic excitation ($\hbar = 1$),

$$\begin{aligned} H_0 &= \sum_q \frac{E_J}{2}\pi_q^2 + 4\sin^2(q/2)U_q\theta_q^2 \\ &= \sum_q \Omega_q(a_q^\dagger a_q + \frac{1}{2}), \end{aligned} \tag{3.108}$$

where q takes integer multiples of π/M, and

$$\Omega_q = \sqrt{\frac{32E_0E_1E_J}{E_1 + 4E_0\sin^2(q/2)}}\sin(q/2) \tag{3.109}$$

is the dispersion of the plasmonic mode that becomes linear ($\sim v_c q$) with speed $v_c = \sqrt{8E_0E_J}$ as q goes to 0 and reaches a maximum at the plasma frequency $\omega_p = \sqrt{8E_1E_J}$.

At finite $g \neq 0$, phase-slips couple single-plasmon state $|q\rangle \equiv a_q^\dagger|0\rangle$ to multi-plasmon states. To get the plasmon lifetime, we calculate self-energy Σ. For the lowest order in Σ, we consider specifically the cubic term in the normal-ordered interaction

$$\frac{1}{3!}g\sum_i \xi_i \sin\Lambda_i : \bar{\theta}_i^3 : \tag{3.110}$$

where ξ_i is the factor arises from normal-ordering defined by $\cos\bar{\theta}_i = \xi_i : \cos\bar{\theta}_i :$. Combining

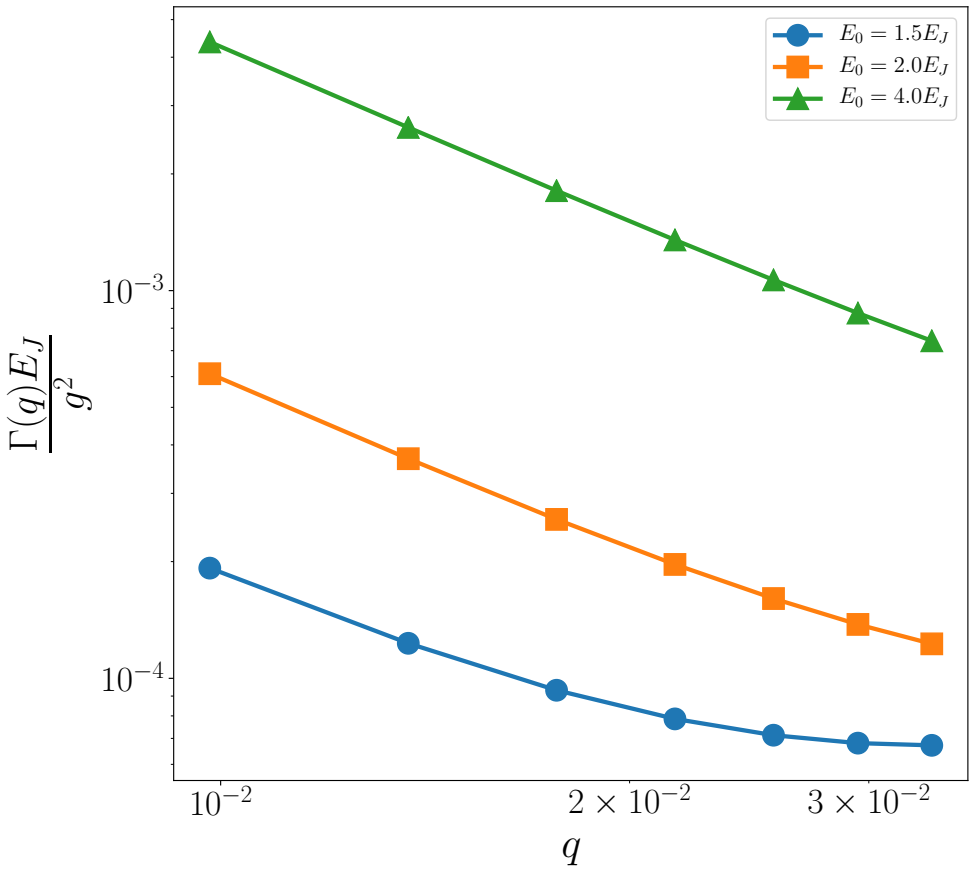

Figure 3.7: Decay rate from single-plasmon states into two-plasmon states on a chain of length $M = 1600$ with system parameters $D = 0.02, E_1/E_J = 0.5$ under different E_0. The decay rate increase at lower wave vectors (i.e. $q \to 0$) is consistent with weaker peaks at smaller frequencies obtained from the sine-Gordon model. Moreover, the suppresion of decay rate as E_0 decreases is again consistent with the experiment [1].

with the free part, followed by a rescaling $\theta \to \sqrt{E_J}\theta$, the full action is

$$S[\theta] = \sum_{q,\omega} \frac{1}{2}(\omega^2 - \Omega_q^2)|\theta_{q,\omega}|^2$$
$$- \frac{g}{3!} \sum_{\{q,\omega\}} 2\pi\delta(\omega_1 + \omega_2 + \omega_3)\Gamma_{q_1,q_2,q_3}\theta_{q_1,\omega_1}\theta_{q_2,\omega_2}\theta_{q_3,\omega_3}, \tag{3.111}$$

where the matrix element is

$$\Gamma_{q_1,q_2,q_3} = (E_J)^{3/2} \sum_i \xi_i \sin\Lambda_i A^i_{q_1} A^i_{q_2} A^i_{q_3} \tag{3.112}$$

with $A^i_q = \sqrt{2/M}\sum_l w_{l-i}\sin ql$.

The plasmon self-energy obtained by second order perturbation theory on Eq. 3.111 is

$$\Sigma(k,\omega) = -ig^2 \sum_{q_1,q_2} \frac{(\Gamma_{k,q_q,q_2})^2}{4\Omega_{q_1}\Omega_{q_2}}$$
$$\times [\frac{1}{-\omega + \Omega_{q_1} + \Omega_{q_2} - i\eta} - \frac{1}{\omega + \Omega_{q_1} + \Omega_{q_2} - i\eta}], \tag{3.113}$$

which gives the damping of plasmon with momentum k as

$$\frac{1}{\tau_k} = \mathrm{Im}\,[i\frac{\Sigma(k,\Omega_k)}{2\Omega_k}]$$
$$= \pi g^2 \sum_{q_1,q_2} (\Gamma_{k,q_q,q_2})^2 \frac{\delta(\Omega_k - \Omega_{q_1} - \Omega_{q_2})}{8\Omega_k\Omega_{q_1}\Omega_{q_2}} \tag{3.114}$$

Next, we perform disorder average on the inverse lifetime,

$$\langle\langle \frac{1}{\tau_k} \rangle\rangle = \pi \sum_{q_1,q_2} \langle\langle (\Gamma_{k,q_q,q_2})^2 \rangle\rangle \frac{\delta(\Omega_k - \Omega_{q_1} - \Omega_{q_2})}{8\Omega_k \Omega_{q_1} \Omega_{q_2}}. \tag{3.115}$$

Using the fact that the correlation function of the Aharonov-Casher phase shift, $\langle\langle e^{\Lambda_i - \Lambda_j} \rangle\rangle = e^{-D\sum_l (w_{l-i} - w_{l-j})^2/2}$,

$$\begin{aligned} \langle\langle (\Gamma_{k,q_q,q_2})^2 \rangle\rangle =& \frac{(E_J)^3}{2} \sum_{i,j} \xi_i \xi_j e^{-\frac{D}{2}\sum_l (w_{l-i} - w_{l-j})^2} \\ & \times (A^i_k A^i_{q_1} A^i_{q_2})(A^j_k A^j_{q_1} A^j_{q_2}) \end{aligned} \tag{3.116}$$

The inverse lifetime for single-plasmon states evaluated using Eq. 3.115 is shown in Fig. 3.7. The phase slip profile is chosen such that $w_{l-j} = \tanh[(l-j+1/2)/5] - \tanh[(l-j-1/2)/5]$, which expands through a length scale of 5 sites. System parameters are chosen to be $M = 1600$, $D = 0.02$ and $E_1/E_J = 0.1$ while E_0/E_J is tuned. Next, we set the factor ξ_i's, which are expected to be a constant of i in the $M \to \infty$ limit, to be 1. This would avoid some finite size effects. Finally, to obtain a finite result from Eq. 3.115, we introduce a Gaussian broadening $\eta = 0.5\omega_{q_{min}}$ in the energy conservation delta function. Such a broadening is essential to obtain a result from the zero temperature approach for a finite system with curvature in the dispersion relation. This issue may be circumvented at finite temperature, where the broadening is created using the decay rate.

3.3 Discussion and Conclusions

In this work we have calculated the imaginary part of the local dynamical polarizability χ in the limit where the Luttinger parameter $K \sim 1$ (corresponding to impedance of order of a conductance quantum) where χ is dominated by the cross-section of generation of SAPs. We find that the resulting χ, for $K = 1$, shows an array of peaks (see Eq. 3.84) whose height increases with increasing frequency in a way that is qualitatively consistent with recent experimental measurements [1]. Increasing K towards the superfluid limit reduces the effective mass (see Eq. 3.78) of the solitons leading to larger oscillations. Such oscillations in χ are surprising at first glance because a JJ chain in the insulating phase, which does not have superconducting phase coherence. We show that the observed oscillations are essentially a consequence of the Lorentz-invariance of the sine-Gordon model description of the chain (Eq. 3.1). The coherent phase oscillations in this model are gapped by a Lorentz-invariant phase-slip (cosine) term, for weak Josephson coupling E_J, resulting in an insulating JJ chain. Such a sine-Gordon model turns out to be a good approximation for long JJ chains in the limit of large JJ capacitance [115]. This is because the Luttinger parameter K (inverse impedance) and the phase-slip amplitude g are independently controlled by the long and short ranged part of the effective screened Coulomb interaction in the micoscopic model (see Sec. 3.2.6). Such clean sine-Gordon models have been proposed to be realized in strongly interacting ultra-cold Bose gases [116]. We expect similar broadened above gap oscillations in χ to apply to a superfluid-insulator transition in the context of ultra-cold atoms [116].

The coherent phase peaks in χ are also found to be robust to charge disorder that is present in JJ chains [1]. The long-range nature of the Coulomb interactions that are encoded

in the capacitances in the JJ chain model ensures that the uncorrelated charge disorder appears smooth on the lattice scale, ensuring the validity of the sine-Gordon model treatment. We have shown analytically that the mean-free path for solitons increases for with frequency for SAPs. However as the frequency of the perturbation is lowered the mean-free path of the SAPs become short leading to localized excitations. This leads to increased broadening of the resonances at lower frequency consistent with recent experiments [1]. We also find that the resonances rest on an incoherent background also seen in the experimental data for high impedance wires [1]. Additionally, the models considered here all have a gap leading to insulating transport in dc, which is also consistent with the recent experiments [1]. The insulating behavior maybe understood as charge disorder pinning of the charged solitons [107].

In the last section of this work, we consider the perturbative decay of plasmons due to quantum phase slips, similar to recent work [117]. However, in contrast to previous work [117], we avoid analytic continuation and directly use Fermi's Golden rule with the quantum phase slip term in Eq. 3.1 being treated as a perturbation. The analytic continuation is particularly difficult for finite size and disordered system. Furthermore, we explicitly exclude disorder broadening of single-plasmon states. Such broadening is included in the disorder averaged self-energy [117]. However, as shown in recent work [108], disorder-induced fluctuations can also lead to extrinsic broadening of the resonances. We also find that strictly speaking such a perturbative decay may be limited or artificially enhanced by energy conservation in a finite chain. We formally circumvent this problem by introducing an intrinsic broadening of the states. We find that the calculated decay rates that increase as one reduces wave-vector q consistent with both experiment [1] and recent theory [117]. However, it is not clear that the intrinsic source of broadening is justified at the low temperatures required to have an insulator.

Finally, we note that our work relies on the integrability of the sine-Gordon model in the clean limit. We have also assumed that this integrability extends to the disordered sine-Gordon model near the Luther-Emery point [89, 95] ($K \simeq 1$) to describe finite real frequency dynamics. On the other hand, the general disordered sine-Gordon model is not integrable and likely exhibits interesting dynamical behavior related to many-body localization [77]. This likely leads to avenues for interesting work on this system in the future regarding low frequency equilibration at this system.

Chapter 4: Classical Model for sub-Planckian Thermal Diffusivity in Complex Crystals

4.1 The Plackian Diffusivity

Despite the diversity of strongly interacting quantum materials, the low energy response of such systems is mostly found to be described by weakly interacting excitations. Paradigmatic examples of these are the quasiparticles in Fermi liquid theory or Goldstone bosons such as phonons or magnons [118]. Notable exceptions to this, in the form of so-called incoherent metals [14, 119], have been proposed in the form of non-Fermi liquids [120, 121, 122, 123] and Bose metals [124], though definitive experimental evidence for such phases is lacking. Signatures of incoherent metals were discovered experimentally in high-Tc superconductors [125, 126, 127, 128, 129], where linear-T resistance appears and persists beyond the Mott-Ioffe-Regel limit [130] where the mean free path becomes smaller than the Fermi wavelength. Surprisingly, the linear-T resistance is also observed at apparently low temperatures [14]. Such a scaling is in direct contradiction to the T^2 behavior expected from the low temperature limit of Boltzmann scattering transport of Fermi liquid quasiparticles [3] from electron-electron interaction. On the other hand, if the electrons are assumed to scatter from other low-energy excitations with a scattering rate τ_s^{-1}, then the conductivity of a material in the semiclassical approximation is expected to follow

the Drude formula $\sigma \propto \omega_p^2 \tau_s$ [119, 131], where ω_p is the plasma frequency. The existence of well-defined quasiparticles, which are the crucial ingredients for Boltzmann theory, are expected to be meaningful when their lifetime induced energy broadening $\hbar\tau^{-1}$ is smaller than the energy of the quasiparticles. Since the typical energy of quasiparticles are of order $k_B T$, this leads to the suggestion of a minimal conductivity $\sigma > \omega_p^2 \tau_P$ where $\tau_P = k_B T/\hbar$ is the Planck scattering time [119]. Interestingly, a significant number of systems presents conductivity near the minimal limit [14, 132, 133, 134]. The description of transport in such systems requires a fully quantum mechanical treatment, which has inspired significant theoretical effort [17, 135, 136, 137, 138].

These ideas have been extended [17] beyond the semiclassical regime to relate more general transport coefficients such as momentum, charge and heat diffusion to viscosity bounds that had been proposed based on holographic methods [139]. A similar instance of universal diffusion bound described by fundamental physical constants is also discovered in liquid systems [140, 141, 142]. In fact, the heat or thermal diffusion coefficient in incoherent metals, where quasiparticles are absent, was studied extensively [143, 144, 145, 146, 147, 148] and was shown to be related to the scrambling time [149] that is bounded by the inverse of the Lyapunov exponent, $\lambda_L^{-1} \geq 2\pi k_B T/\hbar$ whose form is close to the Planckian time τ_P. A complication of measuring thermal diffusion, as was done in cuprate superconductors in the bad metal regime [150, 151] is that it contains contributions from both phonons and electrons. The thermal diffusivity contributions from electrons and phonons in materials approaching the Planckian bound are expected to be described by the form

$$D_P = v_s^2 \tau_P \tag{4.1}$$

where v_s is the sound velocity or the Fermi velocity depending on the relevant carrier [151]. Accordingly, we restrict our discussion to crystalline systems with a well-defined sound velocity in this work. Correlating the thermal diffusion and charge diffusion measurements leads to the conclusion that that the electron and phonon behaves like a soup where both contribute to the thermal transport in an incoherent way [151]. A simpler testing ground for these ideas are provided by the thermal diffusion in insulators where the thermal diffusion is contributed exclusively by phonons. In this case it has been proposed [15, 18] that Eq. 4.1 provides a lower bound for thermal diffusivity for temperatures at or above the order of Debye temperature T_D. Interestingly, this bound appears to be reached for insulators with complex unit cell [15, 18]. Such slow thermal diffusivity has been attributed to be a signature of quantum chaos [19].

Recently, Mousatov et al. [152] have pointed out that the diffusivity bound (Eq. 4.1) can be understood to be a consequence of the fact that the sound velocity v_s is bounded by the melting velocity v_M. This suggests that the thermal diffusivity in complex oxides where v_s approaches v_M could approach the bound in Eq. 4.1. It is also possible that this thermal diffusivity bound motivated by the connection [17] to the viscosity bound is modified for complex insulators. This is because the viscosity bound has been shown to be lowered in multi-component fluids [139].

In this paper, we study the thermal diffusion in a model of a strongly anharmonic crystal and show that in certain parameter regimes the thermal diffusivity can drop below the Planckian bound given in Eq. 4.1. To simplify the problem, we will assume that the temperature T of the system is high enough that the dynamics of the atoms in the crystal can be approximated as classical. However, Planck's constant $\hbar$ enters through the requirement that all phonon frequencies must be below $k_B T/\hbar$. The model we consider has a unit cell with a large number of atoms with very anharmonic interactions that lead to incoherent intracell atomic dynamics. We will show

that these modes contribute negligibly to heat transport, while contributing to heat capacity in a way similar to Einstein phonons [153]. This reduces the thermal diffusivity of the system. In Sec. 4.3, we will first discuss the complex phonon system in the context of Boltzmann transport theory and show that thermal diffusivity must obey the Planckian bound (Eq. 4.1) as long as all phonons are well-defined in the system. In Sec. 4.4.1, we derive an expression for thermal diffusivity of lattice systems with strongly anharmonic intra-cell dynamics connected by weakly anharmonic springs. In Secs. 4.4.2 and 4.4.2, we construct and simulate an example of the model discussed in Sec. 4.4.1 and demonstrate the breaking of the Planckian thermal diffusivity.

4.2 Relevant Aspects in Non-equilibrium Statistical Mechanics

4.2.1 Langevin Equation

In 1828, botanist Robert Brown noticed the irregular movement of Clarkia pulchella pollen in water. This phenomenon, later termed "Brownian motion," results from the random motion of the much lighter particles of the medium that was caused by thermal fluctuations. In general, the motion of a particle in a Brownian system can be described by the equation,

$$m\frac{d\vec{v}}{dt} = \vec{F}(t), \tag{4.2}$$

where $\vec{v}$ is the particle velocity and $\vec{F}(r)$ represents the force acting on the particle by the environment. Langevin [154, 155] suggested that this random force $\vec{F}$ is composed of a viscous force $-\lambda\vec{v}$ that represents the drag at longer time scale, and a rapid fluctuating term $\vec{\eta}$. This gives

the Langevin equation,

$$m\frac{d\vec{v}}{dt} + \lambda\vec{v}(t) = \vec{\eta}(t) \tag{4.3}$$

where the fluctuating term $\vec{\eta}$ does not correlate with the state of the particle and averages to zero $\langle\vec{\eta}\rangle = \vec{0}$. Eq. 4.3 is a stochastic differential equation and due to its linearity, $\vec{v}(t)$ can be solved analytically, which is done by multiplying both sides by $e^{\lambda t/m}$ and integrate over time.

$$\vec{v}(t) = e^{-t/\tau}\left[\vec{v}(0) + \frac{1}{m}\int_0^t e^{t'/\tau}\vec{\eta}(t')dt'\right] \tag{4.4}$$

where $\tau \equiv m/\lambda$ is the system's relaxation time, indicating the time scale over which the average velocity relaxes to zero. This is illustrated by

$$\langle\vec{v}(t)\rangle = \langle\vec{v}(0)\rangle e^{-t/\tau} \tag{4.5}$$

Next, we consider the time evolution of $\langle v^2\rangle = \langle\vec{v}\cdot\vec{v}\rangle$,

$$\langle v^2(t)\rangle = e^{-2t/\tau}\left[v^2(0) + \frac{1}{m^2}\int_0^t\int_0^t e^{(t_1+t_2)/\tau}\langle\vec{\eta}(t_1)\cdot\vec{\eta}(t_2)\rangle dt_1 dt_2\right] \tag{4.6}$$

where the cross term vanishes due to $\langle\vec{\eta}(t)\rangle = 0$. To evaluate the integral

$$\mathcal{I} = \int_0^t\int_0^t e^{(t_1+t_2)/\tau}\langle\vec{\eta}(t_1)\cdot\vec{\eta}(t_2)\rangle dt_1 dt_2, \tag{4.7}$$

we have to model the noise $\vec{\eta}$ from the environment. First, the environment is assumed to be stationary, meaning that the noise correlation should be independent of the absolute time t.

Equivalently, the correlation function must take the form $K_\eta(t_2 - t_1) = \langle \vec{\eta}(t_1) \cdot \vec{\eta}(t_2) \rangle$. Next, the environment should be memory-less beyond some characteristic time scale τ^*. As a result, the correlation should vanish as t becomes much greater than τ^*, or $K_\eta(t \gg \tau^*) \to 0$. Finally, if we further assume that the characteristic time is much less than the relaxation time, the integral 4.7 can be well-approximated by

$$\mathcal{I} \approx C \int_0^t e^{2t_1/\tau} dt_1 = C\frac{\tau}{2}(e^{2t/\tau} - 1) \tag{4.8}$$

where C is the zero-frequency component of the noise auto-correlation function.

$$C = \int_{-\infty}^{\infty} K_\eta(t) dt \tag{4.9}$$

Plugging Eq. 4.8 back to Eq. 4.6, we get

$$\langle v^2(t) \rangle = v^2(0) e^{-2t/\tau} + \frac{C\tau}{2m^2} \left(1 - e^{-2t/\tau}\right). \tag{4.10}$$

The functional form indicates that the initial squared velocity decays over the time scale τ and $\langle v^2(t) \rangle$ approaches a constant value of $C\tau/2m^2$ as $t \to \infty$. We can then make connections between C and the temperature T through the equipartition principle $\langle v^2 \rangle = 3k_B T/m$. That is,

$$C = \frac{6k_B T m}{\tau} = 6k_B T \lambda \tag{4.11}$$

Accordingly, we can rewrite Eq. 4.10 as

$$\langle v^2(t)\rangle = v^2(0)e^{-2t/\tau} + \frac{3k_BT}{m}\left(1 - e^{-2t/\tau}\right). \tag{4.12}$$

which has a stationary solution at the equipartition point $\langle v^2(t)\rangle = 3k_BT/m$.

4.2.2 Mori-Zwanzig Theory

The original Langevin equation presented in Sec. 4.2.1, is formulated as a Markovian process. This means the future evolution of the system is determined solely by its current state, not by its past history. In a broader context, considering the relaxation process of the background medium, the system's evolution should reflect memory effects. Such systems are better described by the generalized Langevin equation.

$$m\frac{d\vec{v}}{dt} = -\int_0^t K(t-t')v(t')dt' + \vec{\eta} \tag{4.13}$$

with the viscous term $-\lambda\vec{v}$ in Eq. 4.3 is replaced by a non-Markovian drag defined by the memory kernel $K(t-t')$.

Mori-Zwanzig formalism is a projection-based method to separate the relevant and irrelevant degrees of freedom of a statistical system to produce the macroscopic equation of motion of the relevant variable. It demonstrates that the evolution of the relevant variable $A(\Gamma)$ defined in the phase space $\Gamma = (\vec{p}, \vec{q})$ takes the common form of the generalize Langevin equation, where the contribution of the irrelevant degrees of freedom takes the form of a noise term $F(t)$ that is uncorrelated with A. It is important to note that the Mori-Zwanzig formalism does not specify

the relevant variables which are typically found as the slow degrees of freedom from empirical observations.

The idea of the formalism is based upon projecting the system variables onto the slow variables. We define the inner product (X, Y) between two variables $X(\vec{p}, \vec{q})$ and $Y(\vec{p}, \vec{q})$,

$$(X, Y) = \int d\Gamma \rho_0(\Gamma) X(\Gamma) Y(\Gamma) \tag{4.14}$$

where ρ_0 represents the equilibrium distribution for the system and $d\Gamma \equiv d^N\vec{p}d^N\vec{q}$. For simplicity, assuming that there is only one relevant variable $A(\Gamma)$, we define a projection operator P to project a variable onto A,

$$PB \equiv \frac{(A, B)}{(A, A)} A \tag{4.15}$$

which is the usual form of a one dimensional projection operator for a given inner product. The projection onto the orthogonal subspace of A is then given by $Q = I - P$, which has the interpretation of projection to the fast variables. As standard projection operators, P and Q are idempotent and self-adjoint. That is, $P^2 = P, Q^2 = Q, (PX, Y) = (X, PY)$, and $(QX, Y) = (X, QY)$. Following Hamiltonian mechanics, time evolution of the variable $A(\vec{p}, \vec{q}, t)$ is given by

$$\frac{dA}{dt} = \left(\frac{\partial}{\partial t} + iL \right) A, \tag{4.16}$$

where iL is called the Liouvillian that can be represented in terms of Poisson bracket with the Hamiltonian $iL = \{\cdot, H\}$. The Poisson bracket is defined as $\{X, Y\} = \sum_{i=1}^{N} \left(\frac{\partial X}{\partial q_i} \frac{\partial Y}{\partial p_i} - \frac{\partial X}{\partial p_i} \frac{\partial Y}{\partial q_i} \right)$. Assuming that the relevant variable $A(\vec{p}, \vec{q})$ has no explicit time dependence, the equation of

motion becomes

$$\frac{dA}{dt} = iLA. \tag{4.17}$$

As a result, the variable A at time t is related to A at time 0 through the evolution operator e^{iLt},

$$A(t) = e^{iLt}A. \tag{4.18}$$

By replacing the $A(t)$ and inserting $(P+Q)$, which is equivalent to I, into the right hand side of Eq. 4.17, the equation of motion becomes,

$$\begin{aligned} \frac{dA}{dt} &= e^{iLt}i(P+Q)LA \\ &= e^{iLt}iPLA + e^{iLt}iQLA. \end{aligned} \tag{4.19}$$

The first term corresponds to the drive that is in parallel with A in the phase space. Therefore, it represents an oscillation in A,

$$\begin{aligned} e^{iLt}iPLA &= ie^{iLt}\frac{(A, LA)}{(A, A)}A \\ &= i\Omega e^{iLt}A \\ &= i\Omega A(t) \end{aligned} \tag{4.20}$$

where the frequency Ω is given by $(A, A)^{-1}(A, LA)$. Next, to decompose the $e^{iLt}iQLA$ term into a pair of dissipation term and a random force, we will employ a mathematical identity on exponential of operators called the Dyson identity. It states that, for a pair of operators X and Y,

the operator $\exp\{[(X+Y)t]\}$ can be decomposed as

$$e^{(X+Y)t} = e^{Xt} + \int_0^t d\tau\, e^{X\tau}\, Y\, e^{(X+Y)(t-\tau)}. \tag{4.21}$$

Plugging in $X = -iQL$ and $Y = -iPL$ to Eq. 4.21 and taking the adjoint on both sides of the equation yields

$$e^{iLt} = e^{iQLt} + \int_0^t d\tau\, e^{iL(t-\tau)}\, iPL\, e^{iQL\tau} \tag{4.22}$$

where we have used the fact that operators L, P, Q are self-adjoint. Plugging Eq. 4.20 and Eq. 4.22 back into Eq. 4.19, we get

$$\frac{dA(t)}{dt} = i\Omega A(t) + \int_0^t d\tau\, e^{iL(t-\tau)}\, iPL\, e^{iQL\tau}\, iQLA + e^{iQLt}\, iQLA \tag{4.23}$$

The last term $F(t) \equiv e^{iQLt}\, iQLA = QF(t)$ is in the orthogonal space of A. Accordingly, it can be shown that the equilibrium average of $F(t)A$ vanishes

$$\begin{aligned} \langle F(t)A\rangle_0 &= (F(t), A) \\ &= (QF(t), A) \\ &= (F(t), QA) = 0 \end{aligned} \tag{4.24}$$

where we have use the self-adjoint property of Q and the fact that $QA = 0$. As a result, $F(t)$ can be identified as a random force. Finally, we will focus on the second term in Eq. 4.23, whose

integrand involves the term

$$\begin{aligned} iPL\, e^{iQL\tau}\, iQLA &= iPLF(\tau) = iPLQF(\tau) \\ &= \frac{(iLQF(\tau), A)}{(A,A)}A = \frac{(F(\tau), -iQLA)}{(A,A)}A \\ &= -\frac{(F(\tau), F(0))}{(A,A)}A \equiv -K(\tau)A. \end{aligned} \tag{4.25}$$

Plugging Eq. 4.25 back into Eq. 4.23 and using the fact that $A(t) = e^{iLt}A$, the equation of motion for A becomes takes the form of a generalized Langevin equation [156, 157]

$$\frac{dA(t)}{dt} = i\Omega A(t) - \int_0^t d\tau\; K(\tau)A(t-\tau) + F(t). \tag{4.26}$$

and the memory kernel $K(\tau)$ is related to the autocorrelation function of the random force in equilibrium $(A,A)^{-1}(F(\tau), F(0))$. Finally, taking the inner product with A on both side, we get the evolution of the correlation function $C(t) = (A(t), A)$

$$\frac{dC(t)}{dt} = i\Omega C(t) - \int_0^t d\tau\; K(\tau)C(t-\tau) \tag{4.27}$$

It is important to note that $\langle A\; F(t)\rangle = 0$ holds only for the equilibrium ensemble ρ_0. Therefore, the two main results of the Mori-Zwanzig theory, given by Eq. 4.26 and 4.27, are limited to describing fluctuations in proximity to the equilibrium.

4.2.3 Fluctuation-Dissipation Theorem

From Eq. 4.11, we can see that there is a linear relation between the viscosity coefficient λ and the zero-frequency fluctuation of the random force C. This result was first discovered by Kirkwood in 1964 [158] and it is an example of the so-called fluctuation-dissipation theorem, which states that for every process that dissipates energy into heat, there is a corresponding fluctuation of a physical quantity of the system at its thermal equilibrium. In this section, we will derive the fluctuation dissipation theorem through the standard procedure of using the linear-response theorem [159]. Our derivation here aligns with the steps described in the textbook by Pathria [160].

To derive the fluctuation-dissipation theorem, it is useful to consider the response of a physical quantity under weak external drive. We will derive fluctuation-dissipation theorem in quantum statistics through the linear response theory by Kubo [161], and the classical version can be obtained by simply sending $\hbar \to 0$. We consider a system described by an unperturbed Hamiltonian H_0 with a small time-dependent perturbation from an external field $h(t)$ that couples with an observable B,

$$H(t) = H_0 - h(t)B. \tag{4.28}$$

In the absence of the perturbation and at finite temperature, the equilibrium density matrix is given by

$$\hat{\rho}_0 = \frac{\exp\left(-\beta H_0\right)}{\mathrm{Tr}\left(\exp\left(-\beta H_0\right)\right)} \tag{4.29}$$

and we will use $\langle\cdot\rangle$ to denote the expectation value in the equilibrium

$$\langle A\rangle = \mathrm{Tr}\,(A\hat{\rho}_0) \tag{4.30}$$

At presence of the perturbation, the density matrix is driven away from the equilibrium. In the regime of linear response, we can assume the density matrix to fluctuate weakly around $\hat{\rho}_0$,

$$\hat{\rho}(t) = \hat{\rho}_0 + \delta\hat{\rho}(t). \tag{4.31}$$

In the linear response regime, the equation of motion can be written as

$$\frac{\partial\hat{\rho}}{\partial t} = \frac{\partial\delta\hat{\rho}}{\partial t} = \frac{1}{i\hbar}\left[H, \hat{\rho}(t)\right] \approx \frac{1}{i\hbar}\left(\left[H_0, \delta\hat{\rho}\right] - h(t)\left[B, \hat{\rho}_0\right]\right) \tag{4.32}$$

where the higher-order terms in $h(t)$ and $\delta\hat{\rho}$ are neglected. In the interaction picture $\hat{A}_I \equiv e^{iH_0t}\hat{A}e^{-iH_0t}$, Eq. 4.32 can be simplified to be

$$\frac{\partial\delta\hat{\rho}_I(t)}{\partial t} = \frac{i}{\hbar}h(t)[B_I(t), \hat{\rho}_0] \tag{4.33}$$

where the commutation between the equilibrium density matrix and unperturbed Hamiltonian is used $[\hat{\rho}_0, H_0] = 0$. The resulting fluctuation of the density matrix is given by,

$$\delta\hat{\rho}_I(t) = \frac{i}{\hbar}\int_{-\infty}^{t} h(t')\left[B_I(t'), \hat{\rho}_0\right] dt' \tag{4.34}$$

where we have assumed the perturbation is turned on in the distant past, or $\lim_{t\to-\infty} h(t) = 0$.

The change in the density matrix can then affect the expectation value of an observable A

$$\begin{aligned}\langle \delta A(t) \rangle &\equiv \langle A(t) \rangle - \langle A \rangle \\ &= \mathrm{Tr}\left(A_I(t) \delta \hat{\rho}_I(t) \right)\end{aligned} \tag{4.35}$$

where $\langle A \rangle \equiv \mathrm{Tr}(A\hat{\rho}_0)$ denotes taking expectation value over the equilibrium density matrix. By plugging in Eq. 4.34, we get the famous result known as the Kubo formula,

$$\langle \delta A(t) \rangle = \frac{i}{\hbar} \int_{-\infty}^{t} h(t') \left\langle [A_I(t), B_I(t')] \right\rangle dt' \tag{4.36}$$

where the circular property of matrix trace is Used. Kubo formula connects the linear-order change of an observable A to a perturbative time-dependent drive coupled to the observable B. In the frequency space, defining the Fourier components $\delta\tilde{A}(\omega) \equiv \int_{\infty}^{-\infty} \langle \delta A(t) \rangle e^{i\omega t} dt$, Eq. 4.36 becomes

$$\begin{aligned}\delta\tilde{A}(\omega) &= \frac{i}{\hbar} \int_{-\infty}^{\infty} dt e^{i\omega t} \int_{-\infty}^{t} dt' h(t') \left\langle [A_I(t), B_I(t')] \right\rangle \\ &= \frac{i}{\hbar} \int_{0}^{\infty} d\tau e^{i\omega \tau} \left\langle [A_I(\tau), B_I(0)] \right\rangle \int_{-\infty}^{\infty} dt' e^{i\omega t'} h(t') \\ &\equiv \tilde{\chi}_{AB}(\omega) \tilde{h}(\omega)\end{aligned} \tag{4.37}$$

where we have used the stationary property of the equilibrium distribution, $\langle [A_I(t), B_I(t')] \rangle = \langle [A_I(t-t'), B_I(0)] \rangle$, and $\tilde{h}(\omega) \equiv \int_{\infty}^{-\infty} h(t) e^{i\omega t} dt$ is the Fourier component of $h(t)$ at frequency

ω. The generalized susceptibility $\tilde{\chi}_{AB}(\omega)$ is then given by

$$\tilde{\chi}_{AB}(\omega) = \frac{i}{\hbar}\int_0^\infty d\tau e^{i\omega\tau}\left\langle [A_I(\tau), B_I(0)]\right\rangle . \tag{4.38}$$

Since the correlation function $\langle [A_I(\tau), B_I(0)]\rangle$ is real, the imaginary part of $\tilde{\chi}_{AB}$ is given by

$$\mathrm{Im}[\tilde{\chi}_{AB}(\omega)] = \frac{1}{2\hbar}\int_{-\infty}^\infty d\tau e^{i\omega\tau}\left\langle [A_I(\tau), B_I(0)]\right\rangle \tag{4.39}$$

The generalized susceptibility function $\tilde{\chi}_{AB}(\omega)$ of a real physical system has to satisfy two mathematical properties. First, due to causality, the $\tilde{\chi}_{AB}(\omega)$ should not have any pole in the upper half plane. Moreover, the magnitude of the susceptibility vanishes above the shortest characteristic timescale of the system. As a result, $\tilde{\chi}_{AB}(\omega)$ will decay faster than $1/|\omega|$ as $\omega \to \infty$. The combination of the two properties guarantees that the real and imaginary part are related through the Kramers-Kronig relation [162, 163],

$$\mathrm{Re}[\tilde{\chi}_{AB}(\omega)] = \frac{1}{\pi}P\int_{-\infty}^\infty \frac{\mathrm{Im}[\tilde{\chi}_{AB}(\omega')]}{\omega' - \omega}d\omega' \tag{4.40}$$

where P denotes the Cauchy principle value. Eq. 4.40 is a direct result of performing a contour integral of $\tilde{\chi}_{AB}(\omega')/(\omega' - \omega)$ over the infinite semi-circle of the upper half plane.

The fluctuation-dissipation theorem connects the power spectrum of the fluctuation of observables A and B, $S_{AB}(\omega)$ to the imaginary part of the generalized susceptibility $\tilde{\chi}_{AB}(\omega)$. The power spectrum $S_{AB}(\omega)$ is defined as the Fourier transform of the correlation function between

A and B in equilibrium,

$$S_{AB}(\omega) = \int_{-\infty}^{\infty} \langle \delta A_I(t) \delta B_I(0) \rangle \, e^{i\omega t} dt \tag{4.41}$$

where $\delta O \equiv O - \langle O \rangle$ represents the fluctuation of O about its mean. Next, we consider the integral on the left hand side of Eq. 4.39,

$$\begin{aligned}
\int_{-\infty}^{\infty} d\tau e^{i\omega\tau} \langle [A_I(\tau), B_I(0)] \rangle &= \int_{-\infty}^{\infty} d\tau e^{i\omega\tau} \langle A_I(\tau) B_I(0) - B_I(0) A_I(\tau) \rangle \\
&= \int_{-\infty}^{\infty} d\tau e^{i\omega\tau} \langle \delta A_I(\tau) \delta B_I(0) \rangle - \langle \delta B_I(0) \delta A_I(\tau) \rangle \\
&= (1 - e^{-\beta\hbar\omega}) \int_{-\infty}^{\infty} d\tau e^{i\omega\tau} \langle \delta A_I(\tau) \delta B_I(0) \rangle \\
&= \left(1 - e^{-\beta\hbar\omega}\right) S_{AB}(\omega),
\end{aligned} \tag{4.42}$$

Plugin the results back in Eq. 4.39, we get the quantum version of the fluctuation-dissipation theorem,

$$\mathrm{Im}\left[\tilde{\chi}_{AB}(\omega)\right] = \frac{1}{2\hbar}\left(1 - e^{-\beta\hbar\omega}\right) S_{AB}(\omega) \tag{4.43}$$

By taking the limit $\hbar \to 0$, we obtain the fluctuation-dissipation theorem in the classical regime,

$$\mathrm{Im}\left[\tilde{\chi}_{AB}(\omega)\right] = \frac{\omega}{2k_B T} S_{AB}(\omega). \tag{4.44}$$

4.2.4 Green-Kubo Formula for Thermal Conductivity

The thermal conductivity κ is a material property denoting its efficiency in conducting heat. It is defined in the Fourier's law as the ratio between the generated energy flux, $\vec{J}_q$, to the gradient

in temperature T,

$$\vec{J}_q = -\kappa \vec{\nabla} T. \tag{4.45}$$

Due to energy conservation, the heat flux and energy density u should satisfy the continuity equation $\frac{\partial u}{\partial t} + \vec{\nabla} \cdot \vec{J}_q = 0$. Together with the fact that $dT = du/C$, where C is the specific heat per unit volume, Eq. 4.45 can be rewritten as a diffusion equation of the energy density

$$\frac{\partial u}{\partial t} = D_{th} \nabla^2 u \tag{4.46}$$

where $D_{th} \equiv \kappa/C$ is the thermal diffusivity. It is important to note that this diffusion equation, which is based on Fourier law, applies on large time and length scales. More generally, if we consider the memory effect and fluctuations in fluid density, the diffusion is described by

$$\frac{\partial u(r,t)}{\partial t} = \int dr' \int_0^t dt' D(r - r', t - t') \, \nabla^2 u(r', t'). \tag{4.47}$$

Considering the fluctuation around the equilibrium $\delta u = u - \langle u \rangle$, it can be shown that the auto-correlation function of the of the energy density fluctuation $C_{\delta u}(r,t) \equiv \langle \delta u(r,t) \delta u(0,0) \rangle$ follows similar evolution,

$$\frac{\partial C_{\delta u}(r,t)}{\partial t} = \int dr' \int_0^t dt' D(r - r', t - t') \, \nabla^2 C_{\delta u}(r', t') \tag{4.48}$$

Performing a Fourier transform on the spatial coordinate and a Laplace transform on the time coordinate yields

$$\tilde{C}_{\delta u}(k,\omega) = \frac{\hat{C}_{\delta u}(k,0)}{i\omega + k^2 \tilde{D}(k,\omega)} \tag{4.49}$$

where tilde denotes the components of Fourier-Laplace transform over both r and t while the hat indicates Fourier-transformed components solely in r. The thermal diffusivity is related to $\tilde{D}(k,\omega)$ by

$$D_{th} = \lim_{\omega\to 0}\lim_{k\to 0}\tilde{D}(k,\omega). \tag{4.50}$$

To solve for $\tilde{D}$ we consider the double time derivative on $\hat{C}_{\delta u}(k,t)$,

$$\begin{aligned} f_k(t) \equiv \frac{\partial^2 \hat{C}_{\delta u}(k,t)}{\partial t^2} &= \frac{\partial}{\partial t}\left\langle \frac{\partial}{\partial t}\delta\hat{u}(k,t)\ \delta\hat{u}(-k,0)\right\rangle \\ &= \frac{\partial}{\partial t}\left\langle iL\delta\hat{u}(k,t)\ \delta\hat{u}(-k,0)\right\rangle \\ &= \left\langle iL\delta\hat{u}(k,t)\ - iL\delta\hat{u}(-k,0)\right\rangle \\ &= -\left\langle \frac{\partial\delta\hat{u}(k,t)}{\partial t}\ \frac{\partial\delta\hat{u}(-k,0)}{\partial t}\right\rangle \\ &= -k^2\left\langle \hat{J}_{qx}(k,t)\hat{J}_{-qx}(-k,0)\right\rangle \end{aligned} \tag{4.51}$$

where we have applied the continuity equation in the last equality and assumed $\pi/2$ rotational symmetry about each of the x, y, z axis. To make connection with Eq. 4.49, we next take a Laplace transform of $f_k(t)$, which yields,

$$\begin{aligned} \tilde{f}_k(s) &= \int_0^\infty \partial_t^2\hat{C}_{\delta u}(k,t)e^{-st}dt \\ &= \partial_t\hat{C}_{\delta u}(k,t)e^{-st}\Big|_0^\infty + s\int_0^\infty e^{-st}\partial_t\hat{C}_{\delta u}(k,t)dt \\ &= se^{-st}\hat{C}_{\delta u}(k,0)\Big|_0^\infty + s^2\int_0^\infty e^{-st}\hat{C}_{\delta u}(k,t)dt \\ &= -s\hat{C}_{\delta u}(k,0) + s^2\tilde{C}_{\delta u}(k,s) \end{aligned} \tag{4.52}$$

Combining the results of Eq. 4.51 and 4.52 with Eq. 4.49, $\tilde{D}(k,\omega)$ can be rewritten as

$$\tilde{D}(k,\omega) = \frac{-\tilde{f}_k(i\omega)/k^2}{\hat{C}_{\delta u}(k,0) + \tilde{f}_k(i\omega)/i\omega} \tag{4.53}$$

By taking the limits in the order specified in Eq. 4.50, the thermal diffusivity can be written as

$$D_{th} = \frac{\int_0^\infty \langle \hat{J}_{qx}(0,t)\ \hat{J}_{-qx}(0,0)\rangle dt}{\langle \delta\hat{u}(0,0)\ \delta\hat{u}(0,0)\rangle} \tag{4.54}$$

Finally, by applying the energy fluctuation formula in canonical ensembles $\langle \delta\hat{u}(0,0)\ \delta\hat{u}(0,0)\rangle = k_B T^2 C/V$, we get the Green-Kubo formula for thermal conductivity [164],

$$\kappa = D_{th}C = \frac{V}{k_B T^2}\int_0^\infty \langle \hat{J}_{qx}(0,t)\ \hat{J}_{-qx}(0,0)\rangle\ dt \tag{4.55}$$

4.3 Thermal Diffusion in the Boltzmann Regime

The thermal transport of a complex phonon system in the classical regime is qualitatively captured by the Boltzmann transport theory in many cases. Under the relaxation time approximation, the thermal conductivity κ, as derived by Peierls [20], takes a form similar to that from kinetic theory,

$$\kappa = \frac{1}{d}\sum_{\vec{q},\lambda} C(\vec{q},\lambda)v^2(\vec{q},\lambda)\tau(\vec{q},\lambda) \tag{4.56}$$

where d is the dimension, $\vec{q}$ and λ are the wave vector and mode index, respectively. C is the specific heat per unit volume, v is the mode velocity, and τ is the relaxation time. In the

classical regime, all normal modes satisfy equipartition principle. That is, $T > \hbar\omega_{max}$ where ω_{max} represents the highest phonon frequency in the system, and $C(\vec{q}, \alpha)$ can be approximated by k_B/V. In this case, the thermal diffusivity $D_{th} \equiv \kappa / \sum_{\vec{q},\lambda} C(\vec{q}, \lambda)$ is given by

$$D_{th} = \frac{1}{Nd} \sum_{\vec{q},\lambda} v^2(\vec{q}, \lambda)\tau(\vec{q}, \lambda), \tag{4.57}$$

where N represents the number of modes.

The central assumption behind the Boltzmann formalism requires the phonons to be well-defined. Therefore, the scattering rate τ^{-1} should not exceed the frequency spacing between different modes. Assuming equal level spacing, this further imposes a lower bound on $\tau(\vec{q}, \lambda)$,

$$\tau(\vec{q}, \lambda) > \frac{N}{\omega_{max}(\vec{q})} > N\tau_P, \tag{4.58}$$

where the second inequality comes from the classical requirement with $\omega_{max}(\vec{q})$ being the highest optical phonon frequency with momentum $\vec{q}$. That is, the distribution is classical equipartition rather than Bose-Einstein distribution. $\tau_P \equiv \hbar/k_B T$ is the Planckian time. Plugging in Eq. 4.58 to Eq. 4.56 and taking the fastest phonon velocity to be the longitudinal sound velocity v_s, we can deduce a lower bound for thermal diffusivity within the Boltzmann regime,

$$D_{th} > \frac{1}{d} v_s^2 \tau_P \sim D_P. \tag{4.59}$$

Therefore, the energy diffusion obtained from Boltzmann transport of phonon will be bounded by the Planckian diffusivity [15, 17, 150].

4.4 Model

4.4.1 Thermal transport with Incoherent Intra-cell Dynamics

To go beyond Boltzmann regime, we consider a lattice model with highly non-linear intra-cell dynamics as illustrated in Fig. 4.1(a). The unit cells are coupled to each other through weakly anharmonic springs acting on an external degrees of freedom $\vec{r} = (r_x, r_y, r_z)$ to form a 3d lattice. Such a model can be considered as a more tractable version of atomic motion in insulators with complex unit cell where thermal diffusivity close to the Planckian limit has been reported [19], which will be elaborated in Sec. 4.5.

The spring force acting on the i^{th} unit cell (circles in Fig. 4.1(a)) is written as

$$\vec{F}(i) = \sum_{\alpha \in \{x,y,z\}} \vec{f}(i,\alpha) - \vec{f}(i-\alpha,\alpha) \tag{4.60}$$

where $\vec{f}(i,\alpha)$ represents the force from the spring to the α direction of site i

$$\vec{f}(i,\alpha) = -k(\vec{r}_i - \vec{r}_{i+\alpha}) + A \sum_{u \in \{x,y,z\}} (r_{u,i} - r_{u,i+\alpha})^2 \, \hat{u} \tag{4.61}$$

with spring constant k and a weak cubic anharmonicity A. Next, at finite temperature T, we assume the intra-cell dynamics to be described by the response function χ. That is,

$$\vec{r}_i(t) = \int dt' \chi(t-t') \vec{f}_i(t') \tag{4.62}$$

where $\vec{f}_i$ represents a force acting on $\vec{r}_i$ and $\chi(t) = 0$ for all $t < 0$. Note that since the center

of mass motion of the unit cell is decoupled from any intra-cell motion, the acoustic phonons at long wavelength will not be damped efficiently by the intra-cell dynamics. This is the reason for having to introduce A in Eq. 4.61, which in turn leads to damping of the acoustic modes. In principle, Eqs. 4.60, 4.61, and 4.62 constitute the equations of motion for the unit cells and one can determine the trajectories $\vec{r}_i(t)$ by solving them self-consistently.

As mentioned in Sec. 4.3, the Boltzmann formalism does not apply in regimes with ill-defined phonons such as the case of strongly anharmonic intra-cell interactions. In this case, one can instead use the discrete version of the Green-Kubo formula in Eq. 4.55, which is given by

$$\kappa = \frac{1}{k_B T^2} \int_0^\infty d\tau \sum_n \langle q_{i,\alpha}(t) q_{i+n,\alpha}(t+\tau) \rangle \,. \tag{4.63}$$

where $q_{i,\alpha}$ represents the heat flux in the α direction at site i which can be written as the rate of energy transfer across the spring connecting sites i and $i+\alpha$,

$$q_{i,\alpha} = -\frac{\vec{f}(i,\alpha) \cdot \left(\dot{\vec{r}}_i + \dot{\vec{r}}_{i+\alpha} \right)}{2}. \tag{4.64}$$

A crucial assumption for the consistency of Eq. 4.64 is that the average power absorbed by the spring

$$\tilde{q}_{i,\alpha} = -\vec{f}(i,\alpha) \cdot \left(\dot{\vec{r}}_i - \dot{\vec{r}}_{i+\alpha} \right) \tag{4.65}$$

vanishes. This is clearly satisfied by the conservative force in Eq. 4.61.

Ultimately, the combination of Eqs. 4.60, 4.61, and 4.62 is a complex non-linear system of equations that requires numerical molecular dynamics to solve [165, 166]. However, in the

limit of weak anharmonicity, the anharmonic part of the force on a spring i.e. $\vec{f}^A(i,\alpha) = A\sum_u (r_{u,i} - r_{u,i+\alpha})^2\,\hat{u}$ can be approximated as being random and uncorrelated $\vec{f}^A(i,\alpha) \approx \vec{\eta}(i,\alpha)$. The mean value of $\vec{\eta}(i,\alpha,t)$ contributes to thermal expansion [4] and can be set to zero by shifting the lattice constants. The variance of $\vec{\eta}$ will be determined self-consistently by solving the combination of Eqs. 4.60, 4.61, and 4.62 at finite T (see Sec. 4.4.4). A random stochastic driving force in a spring would violate the vanishing of the average power $\tilde{q}$ absorbed by the spring. This is remedied by adding a damping term with a coefficient λ determined by the fluctuation-dissipation theorem as

$$\langle \eta_u(i,\alpha,t)\eta_v(j,\beta,t')\rangle = 2\lambda k_B T \delta_{u,v}\delta_{i,j}\delta_{\alpha,\beta}\delta(t-t'). \tag{4.66}$$

where $u, v \in \{x, y, z\}$ represents the different components of the $\vec{\eta}$. The anharmonic part of the force approximated as the combination of random and damping terms is written as:

$$\vec{f}^A(i,\alpha) \approx -\lambda(\dot{\vec{r}}_i - \dot{\vec{r}}_{i+\alpha}) + \vec{\eta}(i,\alpha,t). \tag{4.67}$$

The above equation together with Eqs. 4.61 and 4.62 are now linear so that the correlation functions of the position are Gaussian. The distribution is then completely determined by the 2-point correlation function $\langle r_{u,i}(0) r_{v,j}(t)\rangle$, which can be found by solving Eq. 4.60, 4.61, 4.62, 4.66, and 4.67 in a self-consistent way.

Next, we plug the linearized force $\vec{f}(i,\alpha) = -k(\vec{r}_i - \vec{r}_{i+\alpha}) - \lambda(\dot{\vec{r}}_i - \dot{\vec{r}}_{i+\alpha}) + \vec{\eta}(i,\alpha)$ back into the Green-Kubo formula (Eq. 4.55). Due to the isotropy, we simply pick $\alpha = x$ without loss of generality. Furthermore, the contributions to κ from motions in the x, y, z directions are equal.

This enables us to rewrite κ as

$$\kappa = \frac{3}{k_B T^2} \int_0^\infty d\tau \sum_n \left\langle q^x_{i,x}(t) q^x_{i+n,x}(t+\tau) \right\rangle \tag{4.68}$$

where

$$\begin{aligned} q^x_{i,x} = & [-k(r_{x,i} - r_{x,i+x}) - \lambda(v_{x,i} - v_{x,i+x}) + \eta^x(i,x)] \\ & \times (v_{x,i} + v_{x,i+x}) \end{aligned} \tag{4.69}$$

with $v = \dot{r}$. Approximating the intracell motion to be Gaussian, we can apply the Wick's theorem, which allows decomposing the averages of quartic terms as products of two-point correlation

functions. Considering time-reversal symmetry, the non-vanishing terms are

$$
\begin{aligned}
&\langle q^x_{i,x}(t) q^x_{i+n,x}(t+\tau)\rangle = \\
&\quad k^2\{[2C_{xx}(n,\tau) - C_{xx}(n-x,\tau) - C_{xx}(n+x,\tau)] \\
&\qquad \times [2C_{vv}(n,\tau) + C_{vv}(n-x,\tau) + C_{vv}(n+x,\tau)] \\
&\quad +[C_{xv}(n-x,\tau) - C_{xv}(n+x,\tau)] \\
&\qquad \times [C_{vx}(n-x,\tau) - C_{vx}(n+x,\tau)]\} \\
&+\lambda^2\{[2C_{vv}(n,\tau) - C_{vv}(n-x,\tau) - C_{vv}(n+x,\tau)] \\
&\qquad \times [2C_{vv}(n,\tau) + C_{vv}(n-x,\tau) + C_{vv}(n+x,\tau)] \\
&\quad +[C_{vv}(n-x,\tau) - C_{vv}(n+x,\tau)] \\
&\qquad \times [C_{vv}(n-x,\tau) - C_{vv}(n+x,\tau)]\} \\
&+2\lambda k_B T \delta_{n,0}\delta(\tau)[2C_{vv}(0,0) + C_{vv}(-x,0) + C_{vv}(x,0)].
\end{aligned} \tag{4.70}
$$

where $C_{AB}(n,\tau) \equiv \langle A_i(t) B_{i+n}(t+\tau)\rangle$ and the last term corresponds to the contribution from η. Substituting Eq. 4.70 into Eq. 4.68 and performing a Fourier transform, the thermal conductivity can be represented completely in terms of the position-position power spectrum $S_{xx}(\vec{q},\omega) \equiv \sum_j \int d\tau e^{-i(\vec{q}\cdot\vec{r}_{ij} - \omega\tau)} C_{xx}(\vec{r}_{ij},\tau)$

$$
\begin{aligned}
\kappa = \frac{12}{k_B T^2} &\int_{\vec{q},\omega} \omega^2(k^2 + \omega^2\lambda^2)\sin^2 q_x \left[S_{xx}(\vec{q},\omega)\right]^2 \\
&+\frac{6\lambda}{T}\int_{\vec{q},\omega} \omega^2(1+\cos^2 q_x) S_{xx}(\vec{q},\omega)
\end{aligned} \tag{4.71}
$$

where $\int_{\vec{q},\omega} \equiv \int \frac{d^3q}{(2\pi)^3}\frac{d\omega}{2\pi}$ and the relations $S_{vv} = \omega^2 S_{xx}$, $S_{xv} = i\omega S_{xx}$, and $S_{vx} = -i\omega S_{xx}$ are

applied.

According to fluctuation-dissipation theorem [159], $S_{xx}(\vec{q},\omega)$ is related to the imaginary part of the response function by

$$S_{xx}(\vec{q},\omega) = \frac{2k_BT}{\omega}\text{Im}\left[D(\vec{q},\omega)\right] \tag{4.72}$$

where $D(\vec{q},\omega)$ is the response function in frequency-momentum space defined by

$$\vec{r}(\vec{q},\omega) = D(\vec{q},\omega)\vec{F}(\vec{q},\omega). \tag{4.73}$$

As shown in Sec. 4.4.4, the response function D can be approximated by that of a damped phonon system which is written as:

$$D(\vec{q},\omega) = \frac{1}{\chi^{-1}(\omega) + 4(k - i\omega\lambda)\sum_{u\in\{x,y,z\}}\sin^2 q_u/2}. \tag{4.74}$$

The damping coefficient λ , which scales linearly in T (as derived in the appendix), is related to the anharmonic force through fluctuation-dissipation theorem [159].

4.4.2 Shell-ball Model for Unit Cell

The response function χ in Eq. 4.62 in the last section is determined by the structure of the complex unit cell in Fig. 4.1. In this section, we consider a specific model for the complex unit cell consisting of N identical balls with mass m contained in a spherical shell of radius R with mass M as illustrated in Fig. 4.1. Within each shell, the balls act as point masses that do

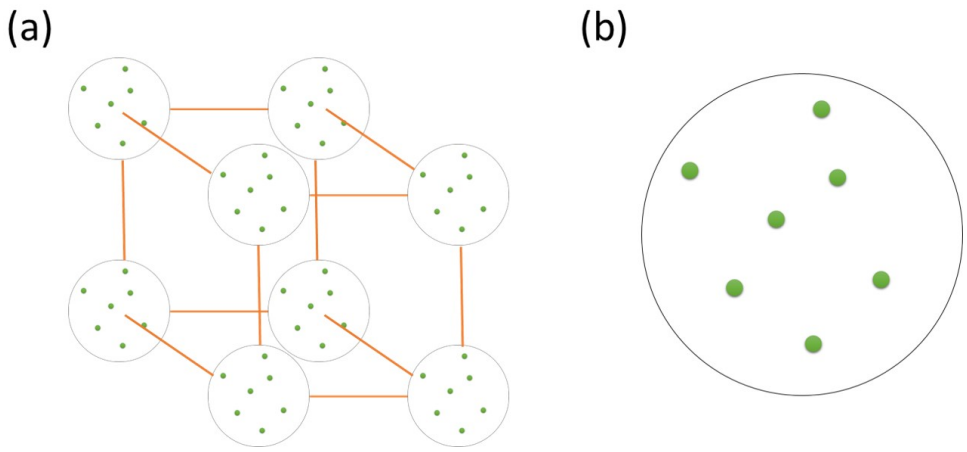

Figure 4.1: (a)Schematics of our cubic lattice. The orange lines represent non-linear springs. Each unit cell is composed of free balls (green circles) of mass m moving within a finite mass M spherical shell of radius R, as illustrated in (b).

not interact with each other and move freely until colliding to the shell, which we assumed to be elastic.

The shell-ball unit cell is studied by direct simulation. N point masses with a total kinetic energy of $3Nk_BT/2$ are placed randomly inside a spherical shell of radius R. The shell velocity is inferred by $\vec{v}_{com} = 0$. Next, we allow the balls to collide with the shell following energy and momentum conservation between the two. After each collision, the updated shell velocity as well as the time of collision are recorded. These data can then be used to calculate the velocity probability distribution and velocity auto-correlation function. The total number of collisions is up to 5×10^6 to reach statistical equilibrium after a warmup of 10^5 collisions. In this work, we will choose units so that $k_BT = 1$ and $m = 1$. The radius R is chosen to be 10 which is much larger than the thermal de Broglie wavelength $\lambda_{th} = \sqrt{2\pi/mk_BT}$ and the shell mass M is chosen to be $M = m = 1$. Fig. 4.3 is the simulation result for $N = 40$ balls. During our simulation, the shell motions between collisions are free. Therefore, within the time interval $t_{i+1} - t_i$ between the i^{th} and $(i+1)^{th}$ collisions, the shell velocity $\vec{v}_i = (v_{x,i}, v_{y,i}, v_{z,i})$ is a constant. In this case, it

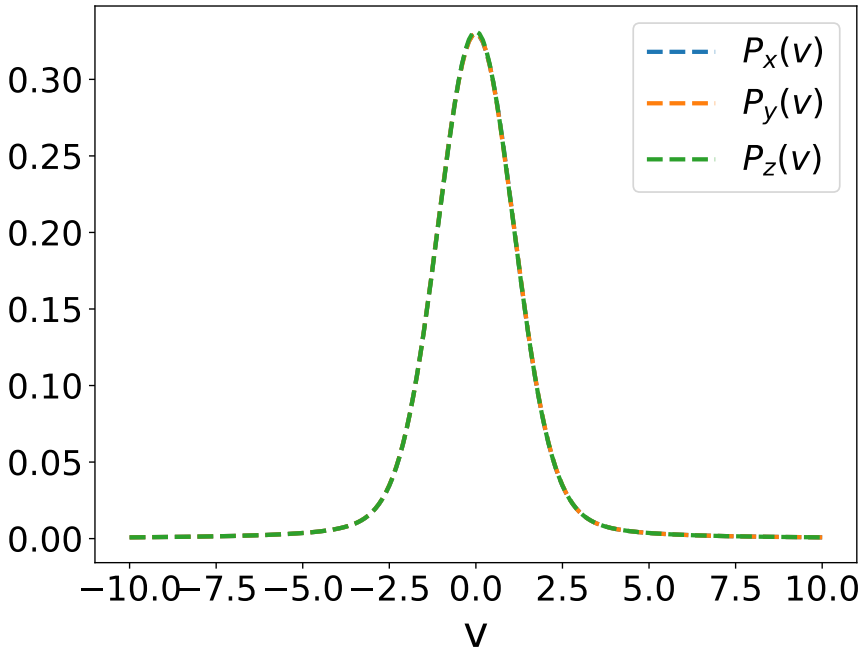

Figure 4.2: Velocity probability distribution of the shell coordinate in different directions for $N = 40$ obtained from simulation with 5×10^6 collisions. The distribution functions match with each other and exhibit Gaussian shapes.

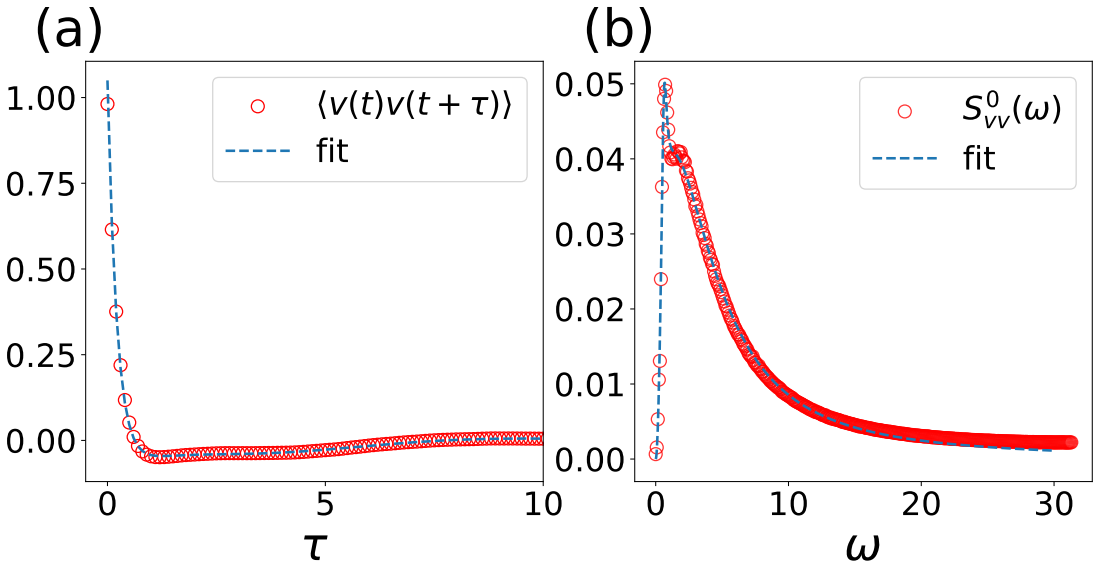

Figure 4.3: (a) The velocity auto-correlation function for $N = 40$ from simulation with 5×10^6 collisions (red open circle). Blue dashed line is the inverse Fourier transform of the fit in the momentum space, as shown in (b). (b) Velocity-velocity power spectrum (red open circle) and rational fit to the data (blue dashed line).

is straightforward to define the velocity distribution as

$$P_\alpha(v) = \sum_i \frac{t_{i+1} - t_i}{T} \delta(v_{\alpha,i} - v) \tag{4.75}$$

where $\alpha \in \{x, y, z\}$ labels the components of the velocity and $T = t_f - t_0$ is the total time. To get a smooth probability distribution, we broaden the δ functions by Lorentzians with width $\Gamma = 0.5$. The result for $N = 40$, number of collisions = 5×10^6 is shown in Fig. 4.2. As can be seen, the velocity distributions in the x, y and z directions match with each other, indicating that our simulation has reached statistical equilibrium. More importantly, the Gaussian nature of $P_\alpha(v)$ validates the application of linear response theorem on the shell coordinate $\vec{r}_i$. The red open circles in Fig. 4.3(a) show the average over the velocity auto-correlation functions of the shell along x, y, and z relative to the center of mass. By taking the Fourier transform, we

obtain the velocity-velocity power spectrum as shown in Fig. 4.3(b). As expected, there is only one broad peak which locates at around the collision frequency of a single ball with the shell. This suggests that the intra-cell motion is mostly incoherent. To get a functional form for the power spectrum, we perform a rational-function fit on the data in Fig. 4.3(b). The resulting fit and its inverse Fourier transform are plotted as blue dashed line in Fig. 4.3(b) and Fig. 4.3(a), respectively.

As shown in Fig. 4.2, the velocity distribution of the shell is Gaussian. Therefore, we expect the response of the shell coordinate $\vec{r}$ to external forces to be linear, consistent with Eq. 4.62. Using fluctuation-dissipation theorem on $S^0_{xx}(\omega) = S^0_{vv}(\omega)/\omega^2$ and the Kramer-Kronig relation, we can obtain the imaginary and real parts of the response function $\chi_r(\omega)$ of the relative coordinate $\vec{r}_{shell} - \vec{r}_{com}$,

$$\begin{aligned} \text{Im}\left[\chi_r(\omega)\right] &= \frac{\omega}{2k_BT} S^0_{xx}(\omega) \\ \text{Re}\left[\chi_r(\omega)\right] &= \frac{1}{\pi}\int_{-\infty}^{\infty} d\omega' \frac{\omega' \text{Im}\left[\chi_r(\omega)\right]}{\omega'^2 - \omega^2}. \end{aligned} \tag{4.76}$$

Taking the center of mass motion into account, the response function of the shell coordinate to external force is given by

$$\chi(\omega) = -\frac{1}{(N+1)\omega^2} + \frac{N}{N+1}\chi_r(\omega). \tag{4.77}$$

The real and imaginary parts for χ with $N = 40$ balls are shown in Fig. 4.4 where the divergence at $\omega \to 0$ comes from the contribution of the center of mass motion.

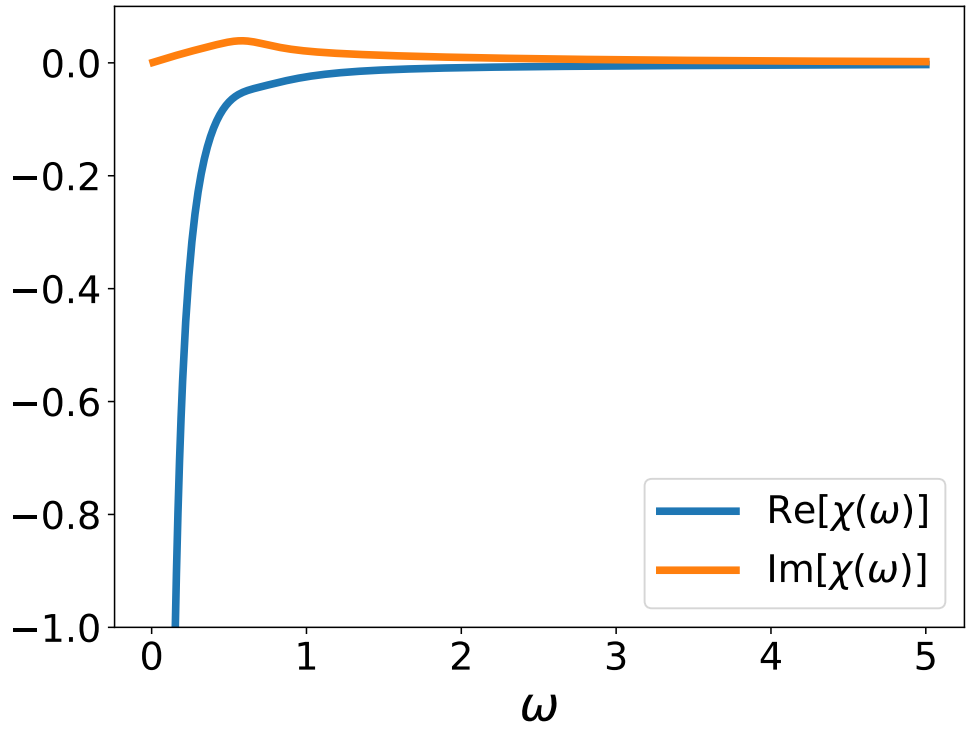

Figure 4.4: Real and imaginary parts of the response function $\chi(\omega)$ of the shell coordinate to an external force for $N = 40$ balls.

4.4.3 Acoustic Phonons in the Shell-ball Model

In the limit of the highly overdamped complex shell-ball model discussed in Sec. 4.4.2, the heat transport turns out to be dominated by acoustic phonons. From the Boltzmann transport equation Eq. 4.56, the transport properties of the acoustic phonons are determined by their dispersion $\omega(\vec{q})$ and damping rate $\tau^{-1}(\vec{q})$. In the limit of weak damping, the acoustic mode is described by a phonon dispersion relation

$$\omega(\vec{q}) = \sqrt{\frac{4k\sum_u \sin^2 q_u/2}{N+1}} \tag{4.78}$$

with a broadening or inverse lifetime

$$\tau^{-1}(\vec{q}) = \frac{2\lambda \sum_u \sin^2 q_u/2}{N+1}. \tag{4.79}$$

Note that the damping is quadratic in the long-wavelength limit, which is consistent with the Akhiezer's damping [167]. However, microscopically, we considered the acoustic phonon to be underdamped, or $\omega\tau > 1$. This contrasts the regime for Akhiezer's mechanism ($\omega\tau << 1$), which is needed for the viewpoint of static lattice distortion at the timescale of relaxation. The choice of k and λ is restricted by the assumptions of our framework. That is, the acoustic phonon cannot be overdamped by λ, or $\tau^{-1}(\vec{q}) < \omega(\vec{q})$, and the acoustic phonon frequency cannot exceed $k_B T = 1$. By substituting Eqs. 4.78 and 4.79 to the constraints above, we get the following conditions for the spring constant k and damping constant λ:

$$\frac{6\lambda}{N+1} < \sqrt{\frac{12k}{N+1}} < 1, \tag{4.80}$$

where the extreme case of $\vec{q} = (\pi, \pi, \pi)$ is taken.

For our numerical computation, we choose a set of parameters consistent with the constraint i.e. $k = 2$ and $\lambda = 2$ for $N = 40$ balls used in the calculation of chi in Fig. 4.4. In Fig. 4.5(a), we plot the imaginary part of the phonon Green's function $D(\vec{q}, \omega)$ along $\vec{q} \parallel (1, 1, 1)$ in frequency-momentum space. As can be observed in bright color, the phonon Green's function exhibits a single coherent mode, while all the other degrees of freedom are incoherent. A vertical cut along $q = 0.8$, as indicated by the red dashed line, is shown in 4.5(b). Besides the coherent Lorentzian peak, we can observe a broad background contributed by the incoherent

modes around frequencies close to the peak in Fig. 4.3(b). Next, the real and imaginary part of the corresponding poles, denoted by ω_s, is shown in 4.5(c) and 4.5(d). First, we confirm that the frequency and lifetime is in the desired regime by satisfying $|\text{Im}[\omega_s]| < \text{Re}[\omega_s] < 1$. Next, they fit to the analytic form in Eqs. 4.78 and 4.79 (orange dashed line) at long wavelength, where the motion is mostly in-phase. This further confirms that this mode possesses the properties of the sound mode. In fact, the coherence of sound mode at long wavelength is expected due to the translational symmetry in our system.

4.4.4 Effective Damping from Cubic Anharmonicity

To work in the regime where the internal force described by χ is linear, we consider the spring force from thermal fluctuation to be weaker than the force ϕ from intra-cell dynamics, that is, $k \cdot k_B T < \langle \phi^2 \rangle$. In the harmonic limit ($A \to 0$), the response function in momentum space defined by is given by

$$D_0(\vec{q}, \omega) = \frac{1}{\chi^{-1}(\omega) + k\,(\vec{q})}, \tag{4.81}$$

where $\chi(\omega)$ is the Fourier transform of $\chi(t)$, $k(\vec{q}) = 4k \sum_{u \in \{x,y,z\}} \sin^2 q_u/2$ is the spring force in momentum space. Since the center of mass coordinate of each unit cell is free from the intra-cell force, there will be well-defined acoustic phonon peaks in D_0 at long wavelength.

From a perturbative picture, the appearance of anharmonicity gives rise to broadening in these coherent peaks through an effective damping force, $-\lambda \sum_{\alpha \in \{x,y,z\}} (2\dot{\vec{r}}_i - \dot{\vec{r}}_{i+\alpha} - \dot{\vec{r}}_{i-\alpha})$ on $\vec{r}_i$. At finite temperature, the anharmonic force can be thought of as a driving force on the harmonic oscillator. At a timescale larger than the correlation time of the anharmonic force $\vec{f}^A(i, \alpha)$, one

can approximate the anharmonic force by a stochastic random force $\vec{\eta}(t)$ with correlation function given by

$$\langle \eta_u(t)\eta_v(t')\rangle = g\delta_{u,v}\delta(t-t') \tag{4.82}$$

where g is the fluctuation strength that is given by the correlation function of $\vec{f}^A(i,\alpha)$,

$$g = \int_{-\infty}^{\infty} d\tau \left\langle f_u^A(i,\alpha,t+\tau) f_u^A(i,\alpha,t)\right\rangle_0 - \left\langle f_u^A(i,\alpha,t)\right\rangle_0^2. \tag{4.83}$$

where $\langle\cdot\rangle_0$ denotes expectation values taken in the harmonic limit. Due to the isotropy, u can be taken as either the x, y, or z component of the non-linear force in Eq. 4.61. By applying Wick's theorem, g can be written in terms of the power spectrum in the following integral form.

$$\begin{aligned} g &= 32A^2 \int \frac{d\omega}{2\pi} \mathcal{I}(\omega)\mathcal{I}(-\omega), \\ \mathcal{I}(\omega) &= \int \frac{d^3q}{(2\pi)^3} \left(\sum_{u\in\{x,y,z\}} \sin^2 \frac{q_u}{2} \right) S_{0,xx}(\vec{q},\omega). \end{aligned} \tag{4.84}$$

The effective damping λ is then given by the following form according to fluctuation-dissipation theorem [159]:

$$\lambda = \frac{g}{2k_BT} \tag{4.85}$$

Note that since g is quartic in displacements (Eq. 4.83), according to the Wick's theorem and the equipartition principle, we expect g to scale as T^2. Together with Eq. 4.85, the scaling of damping is $\lambda \sim T$. In the linear response regime, including the effect of λ into the $D_0(\vec{q},\omega)$

gives the full response function,

$$D(\vec{q},\omega) = \frac{1}{D_0^{-1}(\vec{q},\omega) - 4i\omega\lambda\sum_u \sin^2 q_u/2} = \frac{1}{\chi^{-1}(\omega) + 4(k - i\omega\lambda)\sum_u \sin^2 q_u/2} \tag{4.86}$$

where u sums over x, y, z.

4.4.5 Sub-Planckian Thermal Diffusivity

We are now ready to compute the thermal diffusivity of the shell-ball model. By plugging in the position-position power spectrum $S_{xx}(\vec{q},\omega) = (2k_BT/\omega)\text{Im}[D(\vec{q},\omega)]$ into Eqs. 4.63 and 4.64, we can obtain the thermal conductivity κ. Next, according to equipartition principle, the specific heat per unit cell is $3Nk_B/2$. This gives the thermal diffusivity of our system $D_{th} = 2\kappa/3Nk_B$. On the other hand, since a coherent sound mode exists, the Planckian thermal diffusivity $D_P \equiv v_s^2\tau_P$ is well-defined.

$$D_P = \frac{k}{N+1}. \tag{4.87}$$

For the parameter set considered here ($N = 40$, $k = \lambda = 2$), the resulting $D_{th} \approx 8.13 \times 10^{-3}$, which is below the Planckian bound $D_P \approx 4.88 \times 10^{-2}$. As a result, we have demonstrated a system with sub-Planckian thermal diffusion.

The mechanism for breaking the Planckian bound here is quite simple. Thermal diffusivity is defined as $D_{th} = \kappa/c_v$. For an N-degree-of-freedom unit cell, the specific heat per unit volume scales with N. However, since the phonon Green's function shows only one coherent peak (See

Fig. 4.5(b)) corresponding to the acoustic mode, the optical phonons are incoherent. This is a direct consequence of the highly non-linear intracell dynamics. Due to the small relaxation time, these optical modes does not contribute significantly to the thermal conductivity and we expect the majority of the heat current to be carried by acoustic phonons. In this case, the thermal conductivity κ is only related to N implicitly through the sound velocity $\kappa \sim v_s(N)^2$. As a result, the scaling of thermal diffusivity with N is roughly $D_{th} \sim v_s(N)^2/N$. Therefore, we expect such scenario could attain D_{th}/D_P that scales with inverse the number of balls and sub-Planckian thermal diffusion will appear in the large-N regime.

4.5 Discussion and Conclusions

The shell-ball model discussed here may be instructive for understanding the experimental results on Planckian thermal diffusion in materials with complex unit cells with a large number of atoms. In Ref. [19], it has been pointed out that the insulators which presents thermal diffusivity close to D_P, such as the perovskites, usually exhibit complex unit cells. On the other hand, the insulators with simple unit cell usually have much larger value for D_{th}/D_P. This observation is consistent with our model, where the heat diffusivity is suppressed by the large c_v from the large degrees of freedom N within each unit cell, while the heat conductivity κ does not scale linearly with N. Our model, unlike most holographic models, presents a low energy spectrum described by the coherent acoustic phonons. At low temperature, the thermal energy is carried by these excitations, leading to efficient heat diffusivity well above the Planckian bound. However, as we show, higher temperatures spread out the energy to higher frequency incoherent modes that are not efficiently transmitted, which results in suppressed heat diffusion below the Planckian bound.

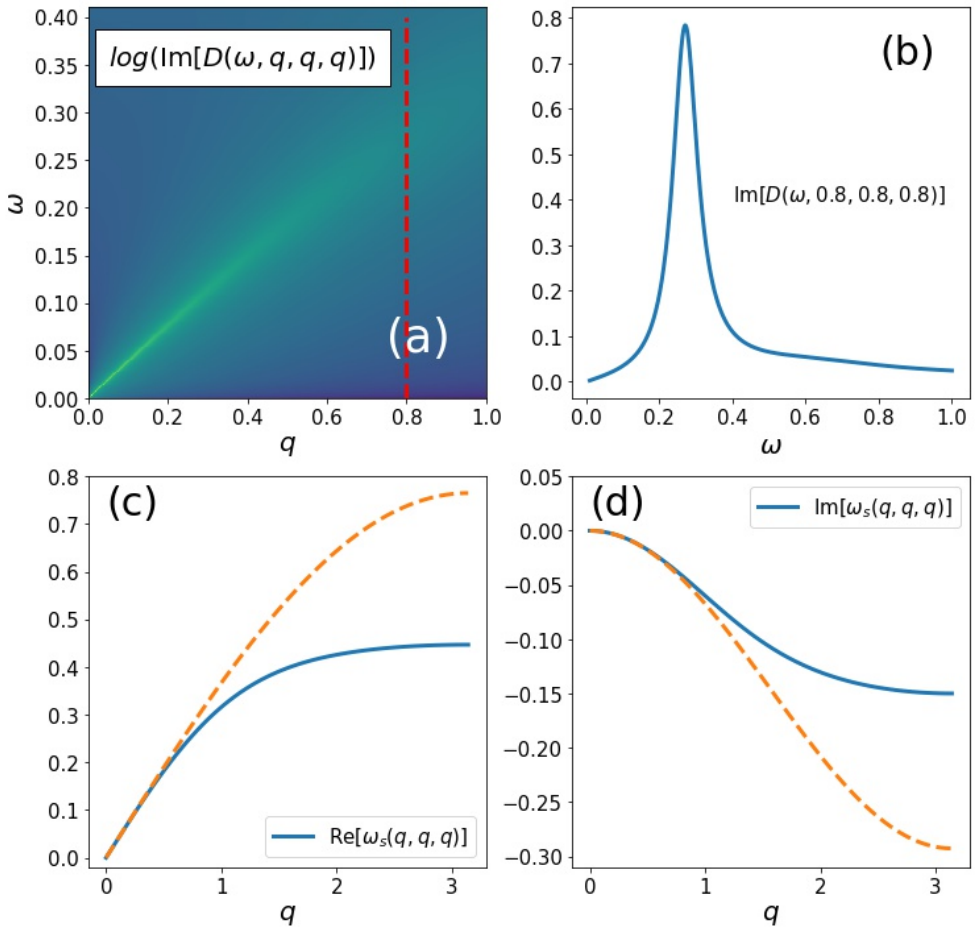

Figure 4.5: (a) Logarithm of the imaginary part (color) of the phonon Green's function in the frequency-momentum space for $\vec{q} \parallel (1,1,1)$, where a coherent mode is visible. (b) The vertical cut of (a) along $q = 0.8$. (c) and (d) Blue solid lines: Real and imaginary part of the poles $\omega_s(q,q,q)$ along $q \parallel (1,1,1)$ that corresponds to the peaks in (a). Orange dashed lines: The corresponding analytic form from Eqs. 4.78 and 4.79.

At intermediate temperature where some of the optical phonons are not thermally activated, we expect quantum behaviors to appear. Similar mechanism has been suggested in Ref. [19] to account for the appearance of $\hbar$ in the thermal diffusivity above Debye temperature. In addition, the intra-cell dynamics in our model is chaotic by nature due to strong non-linearity. This can also be connected to the proposal raised in Ref. [19] that the optical phonons in the Planckian materials likely exhibit chaotic dynamics. Finally, the scenario presented above suggests a smaller bound for thermal diffusivity that is roughly D_P/N. This behavior is consistent with the suppression of the viscosity bound in multi-component fluids [139]. Given the degrees of freedom in the unit cell of the Planckian materials, this is only within one order of magnitude to the measured D_{th}. Therefore, we expect our discussion in Sec. 4.3 to be a useful aspect to explain the Planckian diffusion in experiments.

Recently, Ref. [152] has suggested a diffusion bound based on the melting temperature. Specifically, the melting temperature T_M would give rise to a velocity upper bound v_M which then forces a lower bound to the phonon lifetime by using l/v_M, where l is the phonon mean free path. If we introduce a melting temperature T_M to our shell-ball lattice, a bound on the characteristic frequency $\omega_0 = \sqrt{k/N+1} < T_M$ will appear so that the energy scale from quantum fluctuation on the springs does not cause the lattice to melt. The appearance of this bound can affect the Planckian diffusion bound (Eq. 4.1) in two possible ways. First, there will be a bound on the sound velocity which is given by $a\omega_0$. However, considering the ratio D_{th}/D_P, since the sound velocity affects both D_{th} and D_P in the same way, it does not influence the breaking of Planckian diffusivity. Secondly, the bound on ω_0 will also set an upper bound for the phonon frequency $\omega(\vec{q})$. To stay in the regime where the acoustic phonons are well-defined, the momentum-dependent relaxation time $\tau(\vec{q})$ will be bounded from below. Nevertheless, since

the melting temperature should be a property of the intercell bond, such bound on lifetime should not depend on the internal property of the unit cell. As a result, the thermal diffusivity should still scale as $1/N$ as the number of intra-cell degrees of freedom increases.

The mechanism for sub-Planckian heat diffusivity here constitutes of large number of uncorrelated phonons that contributes to entropy but not heat transport. It is interesting to note that these ingredients can also show up in amorphous solids or glasses. Nevertheless, the disorder in these systems does not guarantee fast thermalization. Specifically, one can imagine the appearance of many harmonic modes in a disorder system that does not relax energy. In contrast, due to the strong nonlinearity of our system, the energy in a phonon excitation would relax rapidly to equilibrium. In the regime above the Ioffe-Regel limit, we believe the breaking of Planckian bound to be also possible in amorphous solids or glasses following the mechanism presented in our system. In fact, the possibility of reaching the Planckian bound has been discussed in Ref. [15]. However, thermal conductivity simulations of such systems require sophisticated method [168]. The model we present here utilizes the timescale separation between intercell and intracell motion, enabling the perturbative approach. Therefore, it can be simulated in a straightforward way.

Even though the mechanism for sub-Planckian heat diffusivity here is rather simple in the sense that it arises from an extra contribution to heat capacity from optical phonons, this mechanism involves transport of heat without the presence of well-defined waves. The anharmonic nature of interactions of the balls in the shell can be viewed as a strongly interacting (although classical) phonon system which is very inefficient in carrying the stored entropy. Understanding the temperature dependence of our results would require us to go to lower temperatures where some of the higher frequency dynamics would ”freeze” out as the Bose-Einstein distribution

replaces the equipartition theorem. However, this regime is beyond the validity of our formalism and provides an opportunity for studying quantum chaotic dynamics. In this case, it becomes a difficult quantum many-body problem where the present approach is invalid.

Chapter 5: Conclusion

Transport properties of a condensed matter system is one of the most important experimental probes for its microscopic physics. While the BTE accurately describes conventional transports, it falls short in modern condensed matter physics, particularly in topological phases, extreme parameter regimes, and lower dimensions. In this thesis, we discussed three systems showing responses beyond the Boltzmann framework.

In chapter 2, we introduce a new family of systems that hosts Majorana zero mode without the need of an external magnetic field or topological insulator [169]. Interestingly, when the wave functions of the two Fermi surfaces are localized to the opposite ends in the z direction, as is the case with HgTe, the 2DEG on one side of the Josephson junction can become a class DIII topological superconductor when ϕ_1 or ϕ_2 becomes π. In this case, helical Majorana edge states can carry ballistic heat flow with central charge $1/2$ around its edge, which is a direct result of quantum coherence of Majorana modes.

In chapter 3, we provide a theoretical description of the coherent phase mode of a Josephson junction chain that is in the insulating side of the SIT [170]. Through focusing on the exactly solvable point at Luttinger parameter $K = 1$, we show that the soliton-antisoliton pair in the sine-Gordon model presents a series of peaks in the polarizability that has a natural broadening due to the finite soliton mass arising from quantum phase slip. The soliton-antisoliton peaks exhibit

asymmetric shapes that is distinct from that of normal photonic excitations. Upon including disorder to the system, the low-frequency soliton and antisoliton becomes Anderson-localized, which manifest themselves as random peaks in the polarizability, while the high frequency responses remain coherent. At low temperature, the transport in this system is dominated by localized states, which is often described by the variable range hopping models. On the other hand, at high temperature, the contribution from the coherent modes dominates and the transport property becomes Boltzmann-like again.

In chapter 4, we introduce a purely classical system with a mechanism to break the Planckian thermal diffusion bound [171]. The Planckian diffusion is characterized by the Planckian relaxation time $\tau_P = \hbar/k_B T$. Pairing with the requirement for classical phonon, $\omega < k_B T$, it is clear that phonon in these systems are overdamped, thereby invalidating the Boltzmann transport theory. We studied a lattice system made up of unit cells consist of a shell containing N balls. The unit cells are are then connected by weakly anharmonic springs into a three dimensional lattice. The mechanism for breaking the Planckian diffusion is based on the highly incoherent intracell dynamics while the sound mode remains coherent. In this case, the thermal energy that scales with N within a unit cell has only a single channel to transport heat. This idea is conceptually similar to the suppression of the viscosity bound in multi-component fluids by Kovtun, Son, and Starinets [139]. At large N, our proposal reduces the diffusivity bound to D_P/N, where D_P is the Planckian diffusivity.

Bibliography

[1] Roman Kuzmin, Raymond Mencia, Nicholas Grabon, Nitish Mehta, Y-H Lin, and Vladimir E Manucharyan. Quantum electrodynamics of a superconductor–insulator phase transition. Nature Physics, 15(9):930–934, 2019.

[2] Ludwig Boltzmann. Weitere studien über das wärmegleichgewicht unter gasmolekülen. Kinetische Theorie II, pages 115–225, 1970.

[3] John M Ziman. Electrons and phonons: the theory of transport phenomena in solids. Oxford university press, 2001.

[4] N.W. Ashcroft and N.D. Mermin. Solid State Physics. Saunders College, Philadelphia, 1976.

[5] BJ Van Wees, H Van Houten, CWJ Beenakker, J Gr Williamson, LP Kouwenhoven, D Van der Marel, and CT Foxon. Quantized conductance of point contacts in a two-dimensional electron gas. Physical Review Letters, 60(9):848, 1988.

[6] Charles Kittel. Introduction to solid state physics. John Wiley & sons, inc, 2005.

[7] Chandra M Varma. Colloquium: Linear in temperature resistivity and associated mysteries including high temperature superconductivity. Reviews of Modern Physics, 92(3):031001, 2020.

[8] Nicholas Read and Dmitry Green. Paired states of fermions in two dimensions with breaking of parity and time-reversal symmetries and the fractional quantum hall effect. Physical Review B, 61(15):10267, 2000.

[9] Alexander Altland and Martin R Zirnbauer. Nonstandard symmetry classes in mesoscopic normal-superconducting hybrid structures. Physical Review B, 55(2):1142, 1997.

[10] Alexander Altland and Ben D Simons. Condensed matter field theory. Cambridge university press, 2010.

[11] Philip W Anderson. Absence of diffusion in certain random lattices. Physical review, 109(5):1492, 1958.

[12] Elihu Abrahams, PW Anderson, DC Licciardello, and TV Ramakrishnan. Scaling theory of localization: Absence of quantum diffusion in two dimensions. Physical Review Letters, 42(10):673, 1979.

[13] Nevill Francis Mott. Conduction in non-crystalline materials: Iii. localized states in a pseudogap and near extremities of conduction and valence bands. Philosophical Magazine, 19(160):835–852, 1969.

[14] JAN Bruin, H Sakai, RS Perry, and AP Mackenzie. Similarity of scattering rates in metals showing t-linear resistivity. Science, 339(6121):804–807, 2013.

[15] Kamran Behnia and Aharon Kapitulnik. A lower bound to the thermal diffusivity of insulators. Journal of Physics: Condensed Matter, 31(40):405702, 2019.

[16] Sean A Hartnoll and Andrew P Mackenzie. Colloquium: Planckian dissipation in metals. Reviews of Modern Physics, 94(4):041002, 2022.

[17] Sean A Hartnoll. Theory of universal incoherent metallic transport. Nature Physics, 11(1):54–61, 2015.

[18] Valentina Martelli, Julio Larrea Jiménez, Mucio Continentino, Elisa Baggio-Saitovitch, and Kamran Behnia. Thermal transport and phonon hydrodynamics in strontium titanate. Physical Review Letters, 120(12):125901, 2018.

[19] Jiecheng Zhang, Erik D Kountz, Kamran Behnia, and Aharon Kapitulnik. Thermalization and possible signatures of quantum chaos in complex crystalline materials. Proceedings of the National Academy of Sciences, 116(40):19869–19874, 2019.

[20] Rudolf Peierls. Zur kinetischen theorie der wärmeleitung in kristallen. Annalen der Physik, 395(8):1055–1101, 1929.

[21] Ettore Majorana. Teoria simmetrica dell'elettrone e del positrone. Il Nuovo Cimento (1924-1942), 14(4):171–184, 1937.

[22] Frank T Avignone III, Steven R Elliott, and Jonathan Engel. Double beta decay, majorana neutrinos, and neutrino mass. Reviews of Modern Physics, 80(2):481, 2008.

[23] Gianfranco Bertone, Dan Hooper, and Joseph Silk. Particle dark matter: Evidence, candidates and constraints. Physics reports, 405(5-6):279–390, 2005.

[24] A Yu Kitaev. Unpaired majorana fermions in quantum wires. Physics-uspekhi, 44(10S):131, 2001.

[25] Olexei Motrunich, Kedar Damle, and David A Huse. Griffiths effects and quantum critical points in dirty superconductors without spin-rotation invariance: One-dimensional examples. Physical Review B, 63(22):224204, 2001.

[26] K Sengupta, Igor Žutić, Hyok-Jon Kwon, Victor M Yakovenko, and S Das Sarma. Midgap edge states and pairing symmetry of quasi-one-dimensional organic superconductors. Physical Review B, 63(14):144531, 2001.

[27] Roman Jackiw and Cláudio Rebbi. Solitons with fermion number $1/2$. Physical Review D, 13(12):3398, 1976.

[28] Liang Fu and Charles L Kane. Superconducting proximity effect and majorana fermions at the surface of a topological insulator. Physical review letters, 100(9):096407, 2008.

[29] B Van Heck, S Mi, and AR Akhmerov. Single fermion manipulation via superconducting phase differences in multiterminal josephson junctions. Physical Review B, 90(15):155450, 2014.

[30] Mengmeng Bai, Fan Yang, Martina Luysberg, Junya Feng, Andrea Bliesener, Gertjan Lippertz, AA Taskin, Joachim Mayer, and Yoichi Ando. Novel self-epitaxy for inducing superconductivity in the topological insulator (bi 1- x sb x) 2 te 3. Physical Review Materials, 4(9):094801, 2020.

[31] Mengmeng Bai, Xian-Kui Wei, Junya Feng, Martina Luysberg, Andrea Bliesener, Gertjan Lippertz, Anjana Uday, Alexey A Taskin, Joachim Mayer, and Yoichi Ando. Proximity-induced superconductivity in (bi1- xsbx) 2te3 topological-insulator nanowires. Communications Materials, 3(1):1–7, 2022.

[32] Martin Endres, Artem Kononov, Michael Stiefel, Marcus Wyss, Hasitha Suriya Arachchige, Jiaqiang Yan, David Mandrus, Kenji Watanabe, Takashi Taniguchi, et al. Transparent josephson junctions in higher-order topological insulator wte2 via pd diffusion. arXiv preprint arXiv:2205.06542, 2022.

[33] A Yu Kitaev. Fault-tolerant quantum computation by anyons. Annals of Physics, 303(1):2–30, 2003.

[34] Michael Freedman, Alexei Kitaev, Michael Larsen, and Zhenghan Wang. Topological quantum computation. Bulletin of the American Mathematical Society, 40(1):31–38, 2003.

[35] Sankar Das Sarma, Michael Freedman, and Chetan Nayak. Topologically protected qubits from a possible non-abelian fractional quantum hall state. Physical review letters, 94(16):166802, 2005.

[36] Chetan Nayak, Steven H Simon, Ady Stern, Michael Freedman, and Sankar Das Sarma. Non-abelian anyons and topological quantum computation. Reviews of Modern Physics, 80(3):1083, 2008.

[37] Ville Lahtinen and Jiannis Pachos. A short introduction to topological quantum computation. SciPost Physics, 3(3):021, 2017.

[38] Xiao-Liang Qi and Shou-Cheng Zhang. Topological insulators and superconductors. Reviews of Modern Physics, 83(4):1057, 2011.

[39] Jay D Sau, Roman M Lutchyn, Sumanta Tewari, and S Das Sarma. Generic new platform for topological quantum computation using semiconductor heterostructures. Physical review letters, 104(4):040502, 2010.

[40] Jay D Sau, Sumanta Tewari, Roman M Lutchyn, Tudor D Stanescu, and S Das Sarma. Non-abelian quantum order in spin-orbit-coupled semiconductors: Search for topological majorana particles in solid-state systems. Physical Review B, 82(21):214509, 2010.

[41] Roman M Lutchyn, Jay D Sau, and S Das Sarma. Majorana fermions and a topological phase transition in semiconductor-superconductor heterostructures. Physical review letters, 105(7):077001, 2010.

[42] Yuval Oreg, Gil Refael, and Felix Von Oppen. Helical liquids and majorana bound states in quantum wires. Physical review letters, 105(17):177002, 2010.

[43] Jason Alicea. New directions in the pursuit of majorana fermions in solid state systems. Reports on progress in physics, 75(7):076501, 2012.

[44] Martin Leijnse and Karsten Flensberg. Introduction to topological superconductivity and majorana fermions. Semiconductor Science and Technology, 27(12):124003, 2012.

[45] B Andrei Bernevig. Topological insulators and topological superconductors. In Topological Insulators and Topological Superconductors. Princeton university press, 2013.

[46] CWJ Beenakker. Search for majorana fermions in superconductors. Annu. Rev. Condens. Matter Phys., 4(1):113–136, 2013.

[47] Liang Fu and Charles L Kane. Josephson current and noise at a superconductor/quantum-spin-hall-insulator/superconductor junction. Physical Review B, 79(16):161408, 2009.

[48] Liangzhi Kou, Yandong Ma, Ziqi Sun, Thomas Heine, and Changfeng Chen. Two-dimensional topological insulators: Progress and prospects. The journal of physical chemistry letters, 8(8):1905–1919, 2017.

[49] Roman M Lutchyn, Erik PAM Bakkers, Leo P Kouwenhoven, Peter Krogstrup, Charles M Marcus, and Yuval Oreg. Majorana zero modes in superconductor–semiconductor heterostructures. Nature Reviews Materials, 3(5):52–68, 2018.

[50] Michael Tinkham. Introduction to superconductivity. Courier Corporation, 2004.

[51] So Takei, Benjamin M Fregoso, Hoi-Yin Hui, Alejandro M Lobos, and S Das Sarma. Soft superconducting gap in semiconductor majorana nanowires. Physical review letters, 110(18):186803, 2013.

[52] Omri Lesser and Yuval Oreg. Majorana zero modes induced by superconducting phase bias. Journal of Physics D: Applied Physics, 55(16):164001, 2022.

[53] Alessandro Romito, Jason Alicea, Gil Refael, and Felix Von Oppen. Manipulating majorana fermions using supercurrents. Physical Review B, 85(2):020502, 2012.

[54] S Vaitiekėnas, GW Winkler, B van Heck, T Karzig, M-T Deng, K Flensberg, LI Glazman, C Nayak, P Krogstrup, RM Lutchyn, et al. Flux-induced topological superconductivity in full-shell nanowires. Science, 367(6485):eaav3392, 2020.

[55] Fernando de Juan, Jens H Bardarson, and Roni Ilan. Conditions for fully gapped topological superconductivity in topological insulator nanowires. SciPost Physics, 6(5):060, 2019.

[56] Falko Pientka, Anna Keselman, Erez Berg, Amir Yacoby, Ady Stern, and Bertrand I Halperin. Topological superconductivity in a planar josephson junction. Physical Review X, 7(2):021032, 2017.

[57] Michael Hell, Martin Leijnse, and Karsten Flensberg. Two-dimensional platform for networks of majorana bound states. Physical review letters, 118(10):107701, 2017.

[58] Antonio Fornieri, Alexander M Whiticar, F Setiawan, Elías Portolés, Asbjørn CC Drachmann, Anna Keselman, Sergei Gronin, Candice Thomas, Tian Wang, Ray Kallaher, et al. Evidence of topological superconductivity in planar josephson junctions. Nature, 569(7754):89–92, 2019.

[59] Hechen Ren, Falko Pientka, Sean Hart, Andrew T Pierce, Michael Kosowsky, Lukas Lunczer, Raimund Schlereth, Benedikt Scharf, Ewelina M Hankiewicz, Laurens W Molenkamp, et al. Topological superconductivity in a phase-controlled josephson junction. Nature, 569(7754):93–98, 2019.

[60] A Banerjee, O Lesser, MA Rahman, H-R Wang, M-R Li, A Kringhøj, AM Whiticar, ACC Drachmann, C Thomas, T Wang, et al. Signatures of a topological phase transition in a planar josephson junction. arXiv preprint arXiv:2201.03453, 2022.

[61] A Banerjee, O Lesser, MA Rahman, C Thomas, T Wang, MJ Manfra, E Berg, Y Oreg, Ady Stern, and CM Marcus. Local and nonlocal transport spectroscopy in planar josephson junctions. arXiv preprint arXiv:2205.09419, 2022.

[62] André Melo, Sebastian Rubbert, and Anton Akhmerov. Supercurrent-induced majorana bound states in a planar geometry. SciPost Physics, 7(3):039, 2019.

[63] O Lesser, Y Oreg, and A Stern. One-dimensional topological superconductivity based entirely on phase control. arXiv preprint arXiv:2205.13537, 2022.

[64] Fan Zhang, CL Kane, and EJ Mele. Time-reversal-invariant topological superconductivity and majorana kramers pairs. Physical review letters, 111(5):056402, 2013.

[65] Andreas P Schnyder, Shinsei Ryu, Akira Furusaki, and Andreas WW Ludwig. Classification of topological insulators and superconductors in three spatial dimensions. Physical Review B, 78(19):195125, 2008.

[66] Alexei Kitaev. Periodic table for topological insulators and superconductors. In AIP conference proceedings, volume 1134, pages 22–30. American Institute of Physics, 2009.

[67] Xiao-Liang Qi, Taylor L Hughes, and Shou-Cheng Zhang. Topological invariants for the fermi surface of a time-reversal-invariant superconductor. Physical Review B, 81(13):134508, 2010.

[68] Jeffrey CY Teo and Charles L Kane. Topological defects and gapless modes in insulators and superconductors. Physical Review B, 82(11):115120, 2010.

[69] Anna Keselman, Liang Fu, Ady Stern, and Erez Berg. Inducing time-reversal-invariant topological superconductivity and fermion parity pumping in quantum wires. Physical review letters, 111(11):116402, 2013.

[70] AF Andreev. Electron spectrum of the intermediate state of superconductors. Sov. Phys. JETP, 22(455):18–23, 1966.

[71] JA Sauls. Andreev bound states and their signatures. Philosophical Transactions of the Royal Society A: Mathematical, Physical and Engineering Sciences, 376(2125):20180140, 2018.

[72] CWJ Beenakker. Universal limit of critical-current fluctuations in mesoscopic josephson junctions. Physical review letters, 67(27):3836, 1991.

[73] M Titov and Carlo WJ Beenakker. Josephson effect in ballistic graphene. Physical Review B, 74(4):041401, 2006.

[74] Tudor D Stanescu, Jay D Sau, Roman M Lutchyn, and S Das Sarma. Proximity effect at the superconductor–topological insulator interface. Physical Review B, 81(24):241310, 2010.

[75] C Julian Chen. Theory of scanning tunneling spectroscopy. Journal of Vacuum Science & Technology A: Vacuum, Surfaces, and Films, 6(2):319–322, 1988.

[76] EG Novik, A Pfeuffer-Jeschke, T Jungwirth, V Latussek, CR Becker, G Landwehr, H Buhmann, and LW Molenkamp. Band structure of semimagnetic hg 1- y mn y te quantum wells. Physical Review B, 72(3):035321, 2005.

[77] Rahul Nandkishore and David A. Huse. Many-body localization and thermalization in quantum statistical mechanics. Annual Review of Condensed Matter Physics, 6(1):15–38, 2015.

[78] Subir Sachdev. What can gauge-gravity duality teach us about condensed matter physics? Annu. Rev. Condens. Matter Phys., 3(1):9–33, 2012.

[79] Subir Sachdev. Quantum phase transitions. Cambridge university press, 2011.

[80] Matthew P. A. Fisher. Quantum phase transitions in disordered two-dimensional superconductors. Phys. Rev. Lett., 65:923–926, Aug 1990.

[81] N Marković, C Christiansen, and A. M. Goldman. Thickness–magnetic field phase diagram at the superconductor-insulator transition in 2d. Phys. Rev. Lett., 81(23):5217, 1998.

[82] Nadya Mason and Aharon Kapitulnik. Superconductor-insulator transition in a capacitively coupled dissipative environment. Phys. Rev. B, 65(22):220505(R), 2002.

[83] A. F. Hebard and M. A. Paalanen. Magnetic-field-tuned superconductor-insulator transition in two-dimensional films. Phys. Rev. Lett., 65(7):927, 1990.

[84] Mintu Mondal, Anand Kamlapure, Somesh Chandra Ganguli, John Jesudasan, Vivas Bagwe, Lara Benfatto, and Pratap Raychaudhuri. Enhancement of the finite-frequency superfluid response in the pseudogap regime of strongly disordered superconducting films. Scientific reports, 3:1357, 2013.

[85] Markus Greiner, Olaf Mandel, Tilman Esslinger, Theodor W Hänsch, and Immanuel Bloch. Quantum phase transition from a superfluid to a mott insulator in a gas of ultracold atoms. nature, 415(6867):39, 2002.

[86] Daniel Podolsky and Subir Sachdev. Spectral functions of the higgs mode near two-dimensional quantum critical points. Phys. Rev. B, 86(5):054508, 2012.

[87] Manuel Endres, Takeshi Fukuhara, David Pekker, Marc Cheneau, Peter Schauβ, Christian Gross, Eugene Demler, Stefan Kuhr, and Immanuel Bloch. The 'higgs' amplitude mode at the two-dimensional superfluid/mott insulator transition. Nature, 487(7408):454, 2012.

[88] R. M. Bradley and S Doniach. Quantum fluctuations in chains of josephson junctions. Phys. Rev. B, 30(3):1138, 1984.

[89] Thierry Giamarchi. Quantum physics in one dimension, volume 121. Oxford university press, 2004.

[90] M Bard, I. V. Protopopov, I. V. Gornyi, A Shnirman, and A. D. Mirlin. Superconductor-insulator transition in disordered josephson-junction chains. Phys. Rev. B, 96(6):064514, 2017.

[91] K. A. Matveev, A. I. Larkin, and L. I. Glazman. Persistent current in superconducting nanorings. Phys. Rev. Lett., 89(9):096802, 2002.

[92] Gianluca Rastelli, Ioan M Pop, and Frank W. J. Hekking. Quantum phase slips in josephson junction rings. Phys. Rev. B, 87(17):174513, 2013.

[93] Edmond Chow, Per Delsing, and David B Haviland. Length-scale dependence of the superconductor-to-insulator quantum phase transition in one dimension. Phys. Rev. Lett., 81(1):204, 1998.

[94] Karin Cedergren, Roger Ackroyd, Sergey Kafanov, Nicolas Vogt, Alexander Shnirman, and Timothy Duty. Insulating josephson junction chains as pinned luttinger liquids. Phys. Rev. Lett., 119(16):167701, 2017.

[95] A. Luther and V. J. Emery. Backward scattering in the one-dimensional electron gas. Phys. Rev. Lett., 33:589–592, Sep 1974.

[96] Edmond Chow, Per Delsing, and David B Haviland. Length-scale dependence of the superconductor-to-insulator quantum phase transition in one dimension. Physical review letters, 81(1):204, 1998.

[97] David B Haviland, Karin Andersson, and Peter Ågren. Superconducting and insulating behavior in one-dimensional josephson junction arrays. Journal of Low Temperature Physics, 118(5-6):733–749, 2000.

[98] Watson Kuo and CD Chen. Scaling analysis of magnetic-field-tuned phase transitions in one-dimensional josephson junction arrays. Phys. Rev. Lett., 87(18):186804, 2001.

[99] Hisao Miyazaki, Yamaguchi Takahide, Akinobu Kanda, and Youiti Ootuka. Quantum phase transition in one-dimensional arrays of resistively shunted small josephson junctions. Phys. Rev. Lett., 89(19):197001, 2002.

[100] Yamaguchi Takahide, Hisao Miyazaki, and Youiti Ootuka. Superconductor-insulator crossover in josephson junction arrays due to reduction from two to one dimension. Phys. Rev. B, 73(22):224503, 2006.

[101] John Michael Kosterlitz and David James Thouless. Ordering, metastability and phase transitions in two-dimensional systems. In Basic Notions Of Condensed Matter Physics, pages 493–515. CRC Press, 2018.

[102] N David Mermin and Herbert Wagner. Absence of ferromagnetism or antiferromagnetism in one-or two-dimensional isotropic heisenberg models. Physical Review Letters, 17(22):1133, 1966.

[103] VL Berezinskii. Destruction of long-range order in one-dimensional and two-dimensional systems possessing a continuous symmetry group. ii. quantum systems. Sov. Phys. JETP, 34(3):610–616, 1972.

[104] KB Efetov. Phase transitions in granulated superconductors. Zhurnal Eksperimental'noi i Teoreticheskoi Fiziki, 78:2017–2032, 1980.

[105] Anatoly I Larkin. Effect of inhomogeneties on the structure of the mixed state of superconductors. Soviet Journal of Experimental and Theoretical Physics, 31:784, 1970.

[106] Hidetoshi Fukuyama and Patrick A Lee. Dynamics of the charge-density wave. i. impurity pinning in a single chain. Physical Review B, 17(2):535, 1978.

[107] Th Giamarchi and H. J. Schulz. Anderson localization and interactions in one-dimensional metals. Phys. Rev. B, 37(1):325, 1988.

[108] Manuel Houzet and Leonid I Glazman. Microwave spectroscopy of a weakly-pinned charge density wave in a superinductor. arXiv preprint arXiv:1901.01515, 2019.

[109] V Gurarie and AM Tsvelik. A superconductor-insulator transition in a one-dimensional array of josephson junctions. Journal of low temperature physics, 135:245–255, 2004.

[110] Al B Zamolodchikov. Mass scale in the sine–gordon model and its reductions. International Journal of Modern Physics A, 10(08):1125–1150, 1995.

[111] Sidney Coleman. Quantum sine-gordon equation as the massive thirring model. Phys. Rev. D, 11:2088–2097, Apr 1975.

[112] Rudolf Baier and E Pilon. On the axial anomaly at finite temperature in the schwinger model. Zeitschrift für Physik C Particles and Fields, 52(2):339–342, 1991.

[113] S. Mandelstam. Soliton operators for the quantized sine-gordon equation. Phys. Rev. D, 11:3026–3030, May 1975.

[114] H Babujian, A Fring, M Karowski, and A Zapletal. Exact form factors in integrable quantum field theories: The sine-gordon model. Nuclear Physics B, 538(3):535–586, 1999.

[115] M-S Choi, J Yi, M. Y. Choi, J Choi, and S-I Lee. Quantum phase transitions in josephson-junction chains. Phys. Rev. B, 57(2):R716, 1998.

[116] H. P. Büchler, G Blatter, and W Zwerger. Commensurate-incommensurate transition of cold atoms in an optical lattice. Phys. Rev. Lett., 90(13):130401, 2003.

[117] M Bard, I. V. Protopopov, and A. D. Mirlin. Decay of plasmonic waves in josephson junction chains. Phys. Rev. B, 98(22):224513, 2018.

[118] Lev Davidovich Landau and Evgenii Mikhailovich Lifshitz. Course of theoretical physics. Elsevier, 2013.

[119] Jan Zaanen. Why the temperature is high. Nature, 430(6999):512–513, 2004.

[120] John A Hertz. Quantum critical phenomena. Physical Review B, 14(3):1165, 1976.

[121] GR Stewart. Non-fermi-liquid behavior in d-and f-electron metals. Reviews of modern Physics, 73(4):797, 2001.

[122] Hilbert v Löhneysen, Achim Rosch, Matthias Vojta, and Peter Wölfle. Fermi-liquid instabilities at magnetic quantum phase transitions. Reviews of Modern Physics, 79(3):1015, 2007.

[123] Sung-Sik Lee. Recent developments in non-fermi liquid theory. Annual Review of Condensed Matter Physics, 9:227–244, 2018.

[124] Aharon Kapitulnik, Steven A Kivelson, and Boris Spivak. Colloquium: anomalous metals: failed superconductors. Reviews of Modern Physics, 91(1):011002, 2019.

[125] H Takagi, B Batlogg, HL Kao, J Kwo, Robert Joseph Cava, JJ Krajewski, and WF Peck Jr. Systematic evolution of temperature-dependent resistivity in la 2- x sr x cuo 4. Physical review letters, 69(20):2975, 1992.

[126] Nigel E Hussey, K Nozawa, H Takagi, S Adachi, and K Tanabe. Anisotropic resistivity of yba 2 cu 4 o 8: Incoherent-to-metallic crossover in the out-of-plane transport. Physical Review B, 56(18):R11423, 1997.

[127] Yoichi Ando, Kouji Segawa, Seiki Komiya, and AN Lavrov. Electrical resistivity anisotropy from self-organized one dimensionality in high-temperature superconductors. Physical review letters, 88(13):137005, 2002.

[128] K Takenaka, J Nohara, R Shiozaki, and S Sugai. Incoherent charge dynamics of la 2- x sr x cuo 4: Dynamical localization and resistivity saturation. Physical Review B, 68(13):134501, 2003.

[129] PL Bach, SR Saha, K Kirshenbaum, J Paglione, and RL Greene. High-temperature resistivity in the iron pnictides and the electron-doped cuprates. Physical Review B, 83(21):212506, 2011.

[130] 11 VJ Emery and SA Kivelson. Superconductivity in bad metals. Physical Review Letters, 74(16):3253, 1995.

[131] Charles Kittel, Paul McEuen, and Paul McEuen. Introduction to solid state physics, volume 8. Wiley New York, 1996.

[132] CC Homes, SV Dordevic, M Strongin, DA Bonn, Ruixing Liang, WN Hardy, Seiki Komiya, Yoichi Ando, G Yu, N Kaneko, et al. A universal scaling relation in high-temperature superconductors. Nature, 430(6999):539–541, 2004.

[133] A Legros, S Benhabib, W Tabis, F Laliberté, M Dion, M Lizaire, B Vignolle, D Vignolles, H Raffy, ZZ Li, et al. Universal t-linear resistivity and planckian dissipation in overdoped cuprates. Nature Physics, 15(2):142–147, 2019.

[134] Yasuyuki Nakajima, Tristin Metz, Christopher Eckberg, Kevin Kirshenbaum, Alex Hughes, Renxiong Wang, Limin Wang, Shanta R Saha, I-Lin Liu, Nicholas P Butch, et al. Quantum-critical scale invariance in a transition metal alloy. Communications Physics, 3(1):1–8, 2020.

[135] VR Shaginyan, KG Popov, and VA Khodel. Quasiclassical physics and t-linear resistivity in both strongly correlated and ordinary metals. Physical Review B, 88(11):115103, 2013.

[136] Vasily Robertovich Shaginyan, M Ya Amusia, AZ Msezane, VA Stephanovich, GS Japaridze, and SA Artamonov. Fermion condensation, t-linear resistivity, and planckian limit. JETP Letters, 110(4):290–295, 2019.

[137] Aavishkar A Patel and Subir Sachdev. Theory of a planckian metal. Physical review letters, 123(6):066601, 2019.

[138] Grigorii Efimovich Volovik. Flat band and planckian metal. JETP Letters, 110(5):352–353, 2019.

[139] Pavel K Kovtun, Dan T Son, and Andrei O Starinets. Viscosity in strongly interacting quantum field theories from black hole physics. Physical review letters, 94(11):111601, 2005.

[140] K Trachenko and VV Brazhkin. Minimal quantum viscosity from fundamental physical constants. Science Advances, 6(17):eaba3747, 2020.

[141] Matteo Baggioli, Vadim Brazhkin, and Kostya Trachenko. Similarity between the kinematic viscosity of quark-gluon plasma and liquids at the viscosity minimum. arXiv preprint arXiv:2003.13506, 2020.

[142] K Trachenko, M Baggioli, K Behnia, and VV Brazhkin. Universal lower bounds on energy and momentum diffusion in liquids. Physical Review B, 103(1):014311, 2021.

[143] Mike Blake. Universal charge diffusion and the butterfly effect in holographic theories. Physical review letters, 117(9):091601, 2016.

[144] Mike Blake, Richard A Davison, and Subir Sachdev. Thermal diffusivity and chaos in metals without quasiparticles. Physical Review D, 96(10):106008, 2017.

[145] Yingfei Gu, Xiao-Liang Qi, and Douglas Stanford. Local criticality, diffusion and chaos in generalized sachdev-ye-kitaev models. Journal of High Energy Physics, 2017(5):125, 2017.

[146] Richard A Davison, Wenbo Fu, Antoine Georges, Yingfei Gu, Kristan Jensen, and Subir Sachdev. Thermoelectric transport in disordered metals without quasiparticles: The sachdev-ye-kitaev models and holography. Physical Review B, 95(15):155131, 2017.

[147] Aavishkar A Patel and Subir Sachdev. Quantum chaos on a critical fermi surface. Proceedings of the National Academy of Sciences, 114(8):1844–1849, 2017.

[148] Mike Blake and Aristomenis Donos. Diffusion and chaos from near ads 2 horizons. Journal of High Energy Physics, 2017(2):13, 2017.

[149] Juan Maldacena, Stephen H Shenker, and Douglas Stanford. A bound on chaos. Journal of High Energy Physics, 2016(8):106, 2016.

[150] Jiecheng Zhang, Eli M Levenson-Falk, BJ Ramshaw, DA Bonn, Ruixing Liang, WN Hardy, Sean A Hartnoll, and Aharon Kapitulnik. Anomalous thermal diffusivity in underdoped yba2cu3o6+ x. Proceedings of the National Academy of Sciences, 114(21):5378–5383, 2017.

[151] Jiecheng Zhang, Erik D Kountz, Eli M Levenson-Falk, Dongjoon Song, Richard L Greene, and Aharon Kapitulnik. Thermal diffusivity above the mott-ioffe-regel limit. Physical Review B, 100(24):241114, 2019.

[152] Connie H Mousatov and Sean A Hartnoll. On the planckian bound for heat diffusion in insulators. Nature Physics, 16(5):579–584, 2020.

[153] A Einstein. Elementary observations on thermal molecular motion in solids. Annalen der Physik, 35:679–694, 1911.

[154] Paul Langevin. Sur la théorie du mouvement brownien. Compt. Rendus, 146:530–533, 1908.

[155] Don S Lemons and Anthony Gythiel. Paul langevin's 1908 paper "on the theory of brownian motion"["sur la théorie du mouvement brownien," cr acad. sci.(paris) 146, 530–533 (1908)]. American Journal of Physics, 65(11):1079–1081, 1997.

[156] Hazime Mori. Transport, collective motion, and brownian motion. Progress of theoretical physics, 33(3):423–455, 1965.

[157] Robert Zwanzig. Memory effects in irreversible thermodynamics. Physical Review, 124(4):983, 1961.

[158] John G Kirkwood. The statistical mechanical theory of transport processes i. general theory. The Journal of Chemical Physics, 14(3):180–201, 1946.

[159] Rep Kubo. The fluctuation-dissipation theorem. Reports on progress in physics, 29(1):255, 1966.

[160] Raj Kumar Pathria. Statistical mechanics. Elsevier, 2016.

[161] Ryogo Kubo. Statistical-mechanical theory of irreversible processes. i. general theory and simple applications to magnetic and conduction problems. Journal of the physical society of Japan, 12(6):570–586, 1957.

[162] R de L Kronig. On the theory of dispersion of x-rays. Josa, 12(6):547–557, 1926.

[163] Hendrik Anthony Kramers. La diffusion de la lumiere par les atomes. In Atti Cong. Intern. Fisica (Transactions of Volta Centenary Congress) Como, volume 2, pages 545–557, 1927.

[164] Robert Zwanzig. Time-correlation functions and transport coefficients in statistical mechanics. Annual Review of Physical Chemistry, 16(1):67–102, 1965.

[165] Anthony JC Ladd, Bill Moran, and William G Hoover. Lattice thermal conductivity: A comparison of molecular dynamics and anharmonic lattice dynamics. Physical Review B, 34(8):5058, 1986.

[166] William Graham Hoover. Computational statistical mechanics. Elsevier, 2012.

[167] A Akhieser. On the absorption of sound in solids. J. Phys.(Ussr), 1:277, 1939.

[168] Ping Sheng and Minyao Zhou. Heat conductivity of amorphous solids: Simulation results on model structures. Science, 253(5019):539–542, 1991.

[169] Huan-Kuang Wu and Jay Sau. Proposal for majorana modes without a magnetic field in a semiconductor-superconductor sandwich structures. arXiv preprint arXiv:2401.02408, 2024.

[170] Huan-Kuang Wu and Jay D Sau. Theory of coherent phase modes in insulating josephson junction chains. Physical Review B, 99(21):214509, 2019.

[171] Huan-Kuang Wu and Jay D Sau. Classical model for sub-planckian thermal diffusivity in complex crystals. Physical Review B, 103(18):184305, 2021.